Addressing Diameter Non-uniformity in the Melt Spinning of Asphaltenes-Derived Carbon Fibres

by

Calvin Phan

A thesis submitted in partial fulfillment of the requirements for the degree of

Master of Science

in
Materials Engineering

Department of Chemical and Materials Engineering
University of Alberta

ABSTRACT

Asphaltenes offer a cheap alternative to the predominant precursor currently used in the manufacture of carbon fibres. Melt spinning is typically employed for transforming asphaltenes into a fibrous form but faces two challenges: inconsistent or poor spinnability and a large diameter variation in the product. This work investigates the diameter variation by separating the variation into a time-dependent component, “relative thinning rate,” and a time-independent component, “fluctuation.” The effects of heat treatment of the asphaltenes precursor prior to spinning near the spinning temperature and delaying the beginning of spinning were explored. Neither methods could completely mitigate thinning but both methods were successful in reducing diameter fluctuation, although delaying the beginning of spinning proved to be more effective. It is suggested that cross-linking and a small amount of cracking could explain results from thermogravimetry and nuclear magnetic resonance. No conclusive trends about the composition, density, and rheology changes with spinning time were observed. The effect of diameter variation on tensile properties was tested but remain inconclusive due to insufficient sample size. Low tensile strengths may also be associated with unoptimized oxidation and carbonization conditions as well as particulate matter that either passed filtration or formed before solidification of the thread line during melt spinning.

PREFACE

Producing carbon fibres from asphaltenes, while significantly cheaper than conventional precursors, should also exhibit competitive mechanical performance when incorporated into composite materials. In the couple of years that I have spent on carbon fibres, many of these ideas were explored, but it was eventually realized that these improvements could not be optimized if fibre diameter is not uniform. To the research group's experience (University of Alberta Carbon Fiber Group, led by Dr. Weixing Chen), asphaltenes-derived carbon fibres tended to have large variations in diameter, so then it was settled that I would investigate the mechanism behind this variance. At this time, I had also observed that many asphaltenes precursors our group worked with were not consistently spinnable and wondered if it may be related to the observed diameter variance.

In order to fulfil the experiments required for the project in a reasonable amount of time with sufficient data quality, I made a few modifications to existing data collection and analysis processes in the group. The semi-automatic diameter measurement, DiameterJ, described in Section 3.4 was modified by me from the source code to tailor to the needs of the data analysis. The laser diffractometer used to measure single fibre diameters prior to tensile testing, better described in Section 3.12, was built by me. The tensile specimen papers were designed by me. I also developed a user interface to assist with analysis of stress-strain data and wrote Python code for log-likelihood Weibull parameter estimation used to characterize the tensile data and conduct statistical analysis. All the experimental work outlined in Section 3 were conducted by me, except for:

- Preparation of the base asphaltene precursor, which was provided by CNOOC Ltd.
- Treatment of asphaltenes in tetrahydrofuran, as well as thermogravimetry and calorimetry, which were carried out by Desirée Leistenschneider in the labs of Dr. Arno de Klerk's group at University of Alberta.
- CHNS(O) elemental analysis, which was carried out by Desirée Leistenschneider in the IOSI labs at University of Alberta.
- Nuclear magnetic resonance spectroscopy and determination of aliphatic and aromatic content, which was conducted by the University of Alberta NMR Lab.
- Rheometry data, which were collected by Thread Innovations.

Some experiments were performed by me at facilities other than the labs of the Carbon Fiber Group at University of Alberta. These are listed as follows:

- Helium pycnometry in the Lipids Lab at the University of Alberta.
- Scanning electron microscopy, which was done in the Earth and Atmospheric Sciences Scanning Electron Microscopy lab.
- Single-fibre specimen preparation, laser diameter measurement, and tensile testing, which were done at the lab of Thread Innovations.

Interpretation of analyzed data to arrive at conclusions, as well as the literature review presented in this thesis was done by me, under the assistance of Dr. Weixing Chen and Desirée Leistenschneider. Dr. Arno de Klerk also gave important pointers in literature review, especially pertaining to content outlined in Section 2.6. I must also thank my old friend and economist, LJ Valencia, for the conversations that helped shape the statistical discussion in Section 4.11.

This thesis is the original work of Calvin Phan. No part of this thesis has been previously published.

CONTENTS

LIST OF FIGURES

LIST OF TABLES

1 INTRODUCTION

1.1 An Economic Precursor for Carbon Fibre Production

There are numerous applications of carbon fibres in industries ranging from aerospace to civil engineering due to its high strength-to-weight ratio, chemical resistance, high temperature tolerance, and low thermal expansion [1, 2]. However, carbon fibres are limited to high end components due to its cost, a large part of which is due to the cost of precursors used to fabricate the carbon fibres, accounting for half of the production costs [3]. Currently, the most popular precursor is polyacrylonitrile (PAN) due to the high quality of fibres obtained [3]. Another common precursor is pitch, which is isotropic by nature but could be made anisotropic by heat treatment, also known as mesophase pitch [4]. Pitch is inexpensive compared to PAN, but the carbon fibres produced have a lower tensile strength and require extensive chemical modifications, thereby inflating processing costs [4].

Meanwhile, a class of components known as “asphaltenes” is associated with problems in bitumen production and transportation as well as environmentally detrimental effects. Asphaltenes are therefore typically regarded as waste products. The low cost of asphaltenes justifies it as a promising alternative to the carbon fibre precursors commonly used currently. A lower precursor cost could mean the expansion of applications for carbon fibres, making it more viable to incorporate into moderate or low-end products.

1.2 Tensile Behaviour and Statistics of Carbon Fibres

Carbon fibres are categorized as a brittle material. Materials of this type are distinguished by negligible plastic deformation upon failure, for example, by tension. As a result, the entire fibre fails catastrophically above a critical stress with no crack growth. The weakest defect where a crack can initiate determines the stress at which the entire fibre fails. This is what’s often referred to as the “weakest link theory” in brittle materials. A common measure of performance for carbon fibres is its tensile strength. The nature of brittle materials leads to tensile strengths that are dependent on the volume of the specimen tested. Carbon fibres with larger diameters would have lower average tensile strengths due to an increased chance for a critical defect to exist within the fibre.

When discussing the strength of carbon fibres, it becomes important to distinguish its volume dependence from its material dependence. It is necessary to fit tensile data to the modified Weibull distribution, which is the direct mathematical consequence of the weakest link theory. The simplest formulation is given by the cumulative distribution function P in the Equation 2.12, which also represents the probability that a sample volume V fails at or below a given tensile stress, σ_f. Given a reference volume V_0, the formulation is characterized by two parameters: the scaling parameter σ_0 which corresponds to the reference failure stress and the shape parameter β, also known as the Weibull modulus [5].

Equation 1.1

$$P = 1 - \exp\left(-\frac{V}{V_0}\left(\frac{\sigma_f}{\sigma_0}\right)^{\beta}\right)$$

Here, β is a measure of the volume dependence of the tensile strength of a group of fibres. A higher β represents a lower volume dependence and a higher defect size homogeneity. Meanwhile, σ_0 of two groups of carbon fibres could be directly compared so long as V_0 is meaningfully chosen. That is, V_0 should represent a volume within the range of the tested fibres to avoid statements based on excessive data extrapolation.

1.3 Carbon-Fibre Precursors and Process Overview [6]

There are three categories of precursors that are or have been commercially viable:

- Cellulosic precursors: these are the oldest precursors used to produce carbon fibres, but only have a 25-30% yield of produced carbon fibres. They have been mostly superseded by more modern precursors.
- Acrylic precursors: these refer to solutions of acrylonitrile and comonomers. The precursor polymerizes into polyacrylonitrile (PAN) in the spinning process, PAN is the most popular precursor fibre used today, and its carbon fibres have a yield of 40-50%.
- Pitch-based precursors: carbon fibres produced from pitch can have a higher modulus than acrylic precursors since the precursor is closer to a graphitic structure. The yield is also higher at >85%.

Regardless of the precursor used, they are formed into fibres, known as “green fibres.” Then, they are stabilized at intermediate temperatures in an oxidizing environment to prevent

remelting in subsequent steps. While the mechanism of stabilization differs depending on the precursor used, typical chemical processes include cyclization, double bond formation, and cross-linking. In any case, the fibres become non-melting even at higher temperatures.

Next, carbonization of oxidized fibres removes volatile heteroatom content (e.g. nitrogen, oxygen, and sulphur) leaving behind a hexagonal carbon structure known as “turbostratic carbon,” which exhibit a short-range order. This step is done at higher temperatures (>1000 °C) in an inert environment. Depending on the type of carbon fibre desired, the peak heat treatment temperature varies. These types are:

- High-strength carbon fibres: the peak temperature is about 1500-1600 °C. Temperatures higher than this lead to a lower tensile strength. This process is also known as “carbonization” and the molecular structure, referred to as “turbostratic carbon” exhibits short-range order.
- High-modulus carbon fibres: the peak temperature is above 1600 °C and up to 3000 °C. The elastic modulus is increased at the expense of tensile strength. Above 2000 °C, an argon environment must be used as nitrogen is no longer inert with carbon. This process is known as “graphitization” as the molecular structure approaches a layered graphitic structure with long-range order.
- Isotropic carbon fibres: for applications where low cost is important, a peak temperature lower than 1000 °C yields fibres that have little ordering in the molecular structure. Both the tensile strength and modulus are low compared to the other types.

A summary of the main carbon fibre production steps from green fibres is illustrated in Figure 1.1. Although the general process is the same independent of the precursor, the specifics (e.g. temperature and time) should be optimized for the precursor in question.

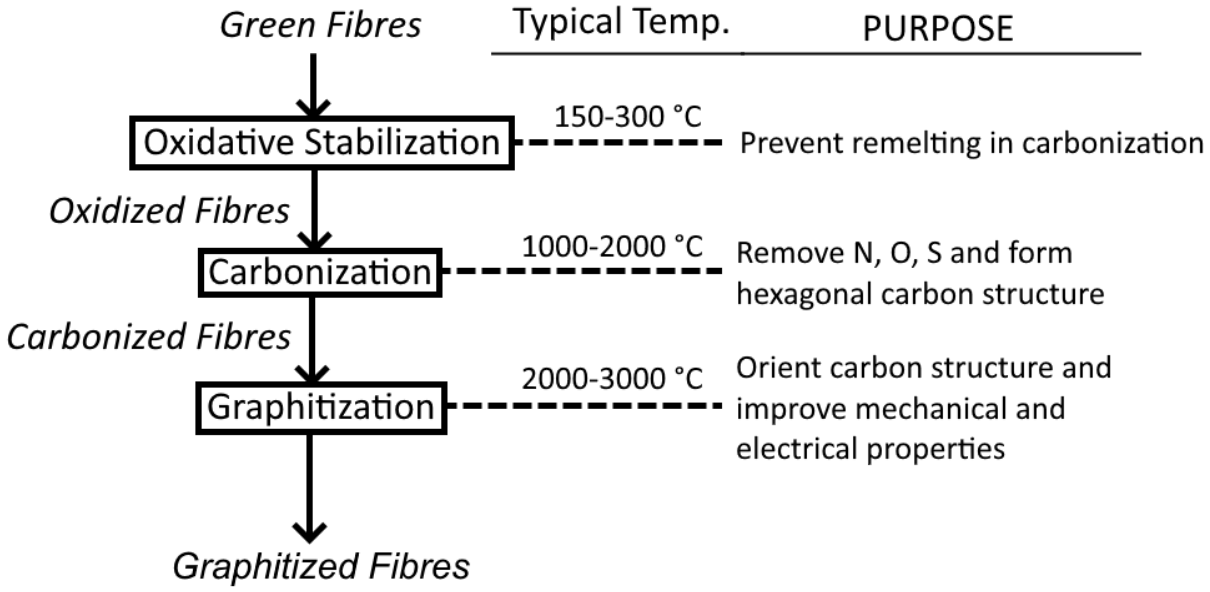

Figure 1.1: Main process steps of carbon fibre production

In an industrial setting, carbonized or graphitized fibres are surface treated to enhance adhesion to a matrix (e.g. epoxy/resin) depending on the application to which the fibres are marketed. The carbon fibres are also subjected to a sizing treatment, which is a coating of a lubricant, typically epoxy, that prevents fibres from adhering to each other during handling and transportation.

1.4 Possible Effect of Diameter Variation on Tensile Properties

The typical measure of the mechanical performance of a strand of carbon fibre is its tensile strength. Green fibres do not have any appreciable strength. The strength of carbon fibres can be attributed to the stabilization, carbonization, and graphitization processes, Carbonization and graphitization strengthen the chemical bonds in the molecular structure of the carbon fibre, but their efficacy is optimized when stabilization is also optimized. To demonstrate the role of diameter on the final tensile strength of a carbon fibre, consider the carbonization step, which aims to remove volatile heteroatoms like nitrogen, oxygen, and sulphur. In the ideal scenario, the escape of the volatiles is accompanied with a decrease in the bulk volume of the fibre. However, should the volatiles be removed and leave behind defects (e.g., pores) in the carbon structure, a lesser extent of shrinking would be observed. These defects effectively decrease the tensile strength of the fibre. Since a higher volatile content can influence the effectiveness of

carbonization in producing a strong fibre, the previous step, stabilization, must be optimized. If the fibres are not sufficiently oxidized, they would remelt during carbonization; if the fibres are over-oxidized, there would be a high volatile content contributing to more defects in the fibre after carbonization. In extreme cases, carbonization of an over-oxidized fibre could result in partial or complete disintegration of the fibre. Since the kinetics of oxidation of green fibres is diffusion-controlled, it is postulated that the carbon fibres processed from green fibres with a higher diameter variance would have a lower reference stress σ_0. Indeed, Zuo et al.'s work show that it is not surprising to observe standard deviations of 4 microns in a 17-micron average diameter batch of green fibres [7]. Mitigating diameter variance could be a significant vector for improving the tensile properties of asphaltenes-derived carbon fibres, should it be shown that the hypothesis is true.

1.5 Observations of Lack of Spinnability

It has been observed that some asphaltenes feedstocks can be melt spun at higher speeds than others. In extreme cases, some asphaltenes cannot be melt-spun at all, with the thread breaking solely under its own weight. Sometimes, there is no flow out of the spinneret, although this is often dismissed as improper setup of the equipment. It is plausible that the mechanism responsible for diameter variation can also influence the spinnability of an asphaltenes feedstock.

1.6 Scope of Work

The objective of this study is to:

1. Confirm the existence and probe the mechanism of large diameter variance of green fibres melt-spun from untreated asphaltenes
2. Determine whether diameter variation plays an effective role in influencing carbon fibre tensile strength

2 LITERATURE REVIEW

2.1 Producing PAN-Based Carbon Fibres [8]

About 90% of carbon fibres are produced from PAN. Since PAN decomposes before melting [9], solution spinning must be employed. A PAN solution is filtered to remove solid inhomogeneities and then spun with one of the two main types:

- Dry spinning: a hot PAN solution is pumped through a spinneret into flowing hot gas, which is above the boiling temperature of the solvent. Evaporation of the solvent leaves behind solid fibres.
- Wet spinning: PAN solution is pumped through a spinneret into a coagulation bath. The polymer precipitates out of the coagulation bath as fibres.

During stabilization, the linear chain PAN is transformed into a ladder structure. Stretching in the stabilization stage is necessary to straighten polymer chains of random conformation and in doing so, the partial charges on the nitrogen and carbon of the nitrile groups of neighbouring monomer units attract and align. Conversion of the nitrogen triple bond to a double bond (cyclization) and oxidation of the carbons in the main chain completes the stabilization process of PAN [10]. This process is illustrated in Figure 2.1.

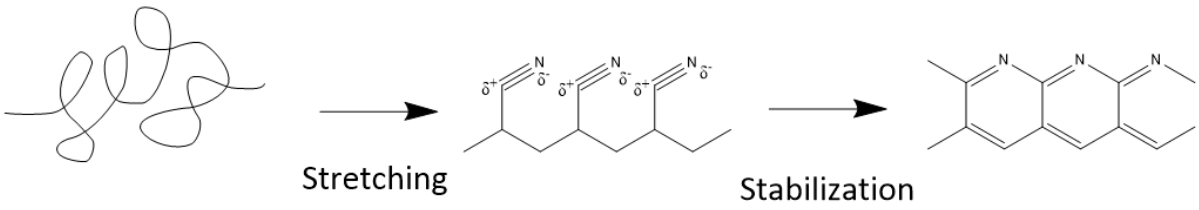

Figure 2.1: Stabilization of PAN-Based Fibres

Because of the presence of solvent in PAN-based green fibres, it must be removed during stabilization. Care must be taken to control variables (e.g. time and temperature) of the process steps so that the removal of solvent does not leave behind pores, and if they do, that the pores are collapsed. This is also achieved by stretching during stabilization. Washing, drying, and additional heat treatments may be added to the stabilization process to close pores that would detriment the tensile strengths of the final carbon fibre product. Time and temperature must also be optimized for stabilization to minimize pore volume, which can be generated with the escape of volatiles.

In carbonization, elimination of hydrogen and nitrogen through various reactions assembles the ladder structures into sheets. Note that while the ideal PAN macromolecule discussed in Figure 2.1 is oxygen-free, in practice comonomers are included in the PAN precursor which may contain some oxygen. The oxygen is also removed during carbonization. The reactions responsible for carbonization are various and are not discussed here. However, the kinetics of different reactions have a different temperature dependence, and so depending on the temperature of carbonization, some reactions could be favoured over others [11, 12]. Also, the carbonization should be slow enough to allow for produced gases to escape without leaving pores behind. Therefore, time and temperature must also be well-controlled for carbonization.

2.2 Producing Carbon Fibre from Pitch

The next most popular precursor from which to derive carbon fibres is pitch. While the definition of pitch is broad, it typically refers to a black viscoelastic substance left behind after distillation of petroleum, coal tar, or other organic matter. Pitches are characterized by a high aromatic content and high melting point compared to the distillates of the source material. While there is no defined set of molecules that define pitch, they are typically polyaromatic or heterocyclic compounds substituted with short-chain alkyl side groups. Some example molecules [13] are given in Figure 2.2.

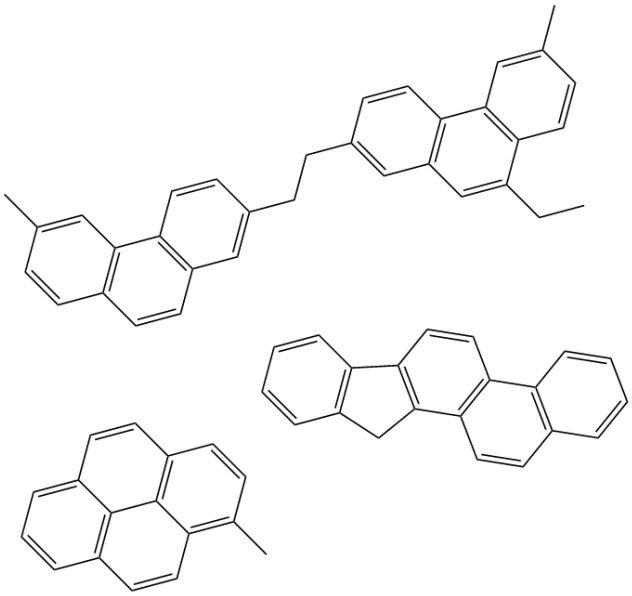

Figure 2.2: Examples of molecules in petroleum pitch

Both coal tar and petroleum pitches are used as precursors for carbon fibres. Naturally occurring pitches are optically isotropic but can be made anisotropic by heat treatment, which cross-links some of the aromatic molecules into longer chains. The layering of the aromatic planes of these molecules lead to disc-like structures with orientational order but not positional order. The anisotropic domains are referred to as "mesophase" signifying a phase in between that of a liquid and crystalline solid. By extension, a pitch that has anisotropic content is referred to as "mesophase pitch." Typically, heat treatment alone leads to only a limited fraction of mesophase. Figure 2.3 summarizes some methods to prepare mesophase pitch as a carbon fibre precursor. Further cross-linking of mesophase transforms it into coke, which is a non-melting solid.

Obtani	tributyl phosphate poly vinyl chloride pitch	→	heat treatment		
UCC	pitch	→	heat treatment under vigorous nitrogen flow		
Diefendorf	pitch	→	heat treatment	→	solvent extraction
Strehlow Tonen	pitch	→	heat treatment	→	high temperature centrifugation
Mochida	pitch	→	hydrogenation with catalyst	→	heat treatment
Yamada	pitch	→	hydrogenation by THQ	→	heat treatment
Park	pitch	→	heat treatment under pressure	→	heat treatment under vacuum
Mochida	pitch naphthalene	→	condensation with $AlCl_3$	→	heat treatment
Mochida	naphthalene methylnaphthalene ethylene tar	→	condensation with HF/BF_3		

Figure 2.3: Some methods of producing mesophase pitch as a carbon fibre precursor. Adapted from [14].

One major advantage of using pitch as opposed to PAN is that melt spinning can be employed instead of solution spinning. The elimination of solvents from the spinning process reduces the number of variables that must be tuned (e.g. polymer concentration, copolymer concentration, etc.) and simplifies the stabilization step. Unfortunately, despite the lower precursor cost and simpler process, carbon fibres derived from isotropic pitch tend to be weaker than PAN-based fibres [15, 16]. The applications of carbon fibres made from isotropic pitch are limited to those where cost is more important than performance.

Meanwhile carbon fibres derived from mesophase pitch tend to have slightly lower tensile strength but have exceptional moduli compared to PAN. Mesophase pitch is also advantageous as tension during the spinning process is not needed. However, it turns out that mesophase pitch carbon fibres are more expensive than PAN-based fibres [16, 17]. Due to the high moduli, they are restricted for high performance applications. The high cost of mesophase pitch is attributed to its difficulties with spinnability compared to PAN or isotropic pitch feedstocks. The reasons have been attributed to [17, 10]:

- the mesophase pitch precursor needs to be tuned (e.g. mesophase content) so that its viscosity is within a spinnable range,
- the viscosity of mesophase pitch has a high temperature dependence and therefore requires melt spinning equipment with precise temperature control,
- continuous transition of mesophase into coke,
- evolution of gases during spinning,
- heterogeneity due to isotropic and anisotropic regions

2.3 Producing Carbon Fibre from Asphaltenes

Oilsands bitumen and crude oil are too viscous for effective flow, and must either be diluted with solvent (i.e. cutter stock) or undergo a mild cracking process (i.e. visbreaking) to allow for transportation in pipelines. The high viscosity is attributed to the oil's heaviest fraction, asphaltenes, which can become a problem if they precipitate out of the fluid during transportation. If that happens, asphaltene deposition can coat surfaces and plug components of processing equipment [18].

Asphaltenes can be removed from bitumen by dissolving the bitumen in a light alkane such as pentane or heptane and filtering out the precipitates. Therefore, its definition is based on solubility class rather than a defined molecular structure: insoluble in light alkanes but soluble in toluene. It is a brittle black solid at room temperature but melts into a viscous liquid above its softening point. Asphaltenes are the heaviest component of bitumen with typical densities ranging from 1.1 to 1.6 g/cm^3 at room temperature [19]. Molecules of asphaltenes have higher aromatic and heteroatom (e.g. nitrogen, oxygen, and sulphur) contents than the bitumen that they are derived from.

Over the course of asphaltenes research, there has been a long debate about the molecular structure of asphaltenes. It is worth noting that because asphaltenes are derived based on solubility class, any discussion about its molecular structure refers to a representative or "average" structure. Any given asphaltenes sample will consist of an ensemble of molecules of various size. To complicate matters more, it is well-known that asphaltenes form aggregates which, for a time, led to rigorous debate over the structure of asphaltenes. For example, initial measurements with vapour pressure osmometry yielded molecular weights on the order of 1000-10,000 g/mol. Various techniques have since disproved this in favour of a molecular weight ~750 g/mol [20]. The initial inflated values of molecular weight were due to asphaltenes' tendency to aggregate. In fact, this behaviour is described in the Yen-Mullins model. This model describes asphaltenes as monomers with a central fused ring structure with aliphatic chains attached to its perimeter (Figure 2.4). These molecules form nanoaggregates consisting of several molecules even at low concentrations (~150 mg/L in n-heptane) and at higher concentrations (~2 g/L in n-heptane) several nanoaggregates can form clusters about 5 nanometres in size [21].

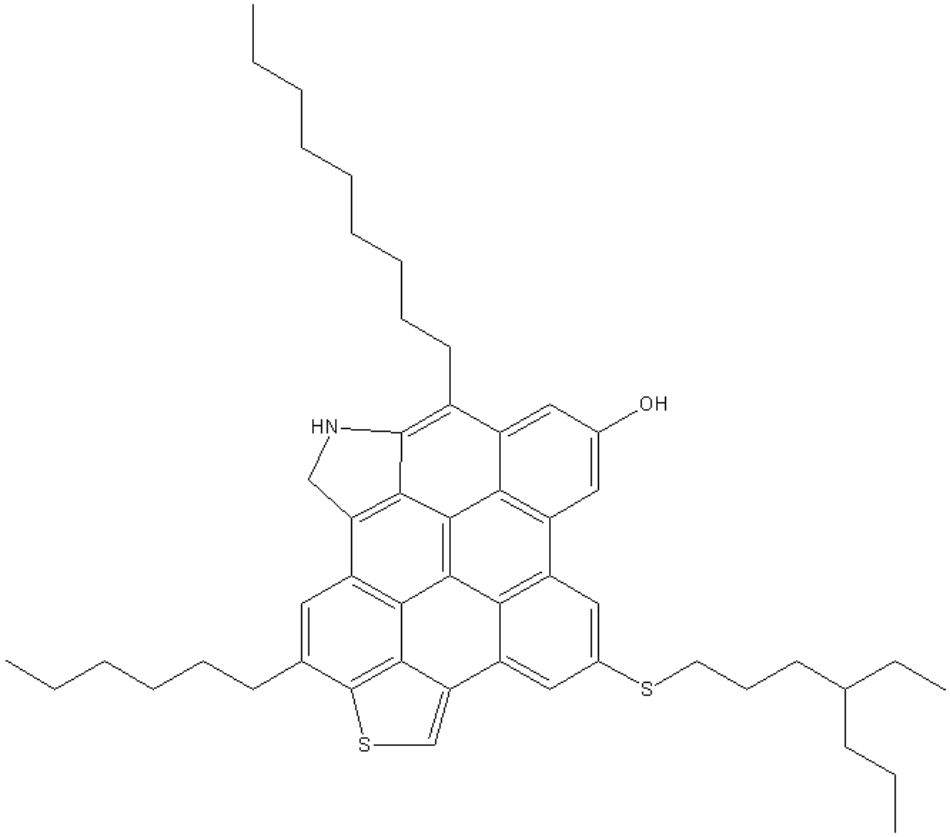

Figure 2.4: Example of an asphaltenes molecule

The carbon fibre production process from asphaltenes is similar to pitch. In the melt spinning of asphaltenes, the feedstock is heated up to a liquid state and then pushed through a spinneret, a metal plate with one or more orifices, forming the extrudate which is then wound around and pulled by a rotating drum. To prevent large particles such as residual coke or ash, a filter is typically placed before the asphaltenes melt encounter the spinneret. In this work, a batch melt spinner is used where the pressure to force the melt through the spinneret is supplied via pressurized gas. This gas must be inert to mitigate oxidation of the feedstock, which can occur much lower than typical spinning temperatures. In a mass production setting, the pressure is typically supplied by one or two rotating screws which allow the feedstock to be continuously supplied at one end and heated on the other.

Another difference between asphaltenes and other precursors in the carbon fibre production process is stabilization. The typical single-step air oxidation is ineffective at stabilizing the fibres prior to carbonization [22]. Two methods of stabilizing asphaltenes green fibres are presented in literature:

- Step-wise air oxidation [22]: Saad et al. successfully stabilized green fibres by employing a two-step oxidation process at 260 and 350 °C. The total time of the process was 10 hours discounting cooling at the end.
- Acid-assisted oxidation [23]: Leistenschneider et al. successfully stabilized green fibres by submersing them in nitric acid, followed by oxidation in flowing air at 260 °C without prior drying. The total time of the process was 9 hours. Later optimization reduced the oxidation time to 5 hours at the same temperature [24].

Carbonization and graphitization processes of asphaltenes-derived carbon fibres are similar to those produced from PAN or pitch, although the exact temperature and times of the heat treatment could be tuned specific to the precursor. However, little work has been done to differentiate these treatments between asphaltenes and conventional precursors.

2.4 Effect of Fluid Properties on Melt Spinning

To understand the effect of fluid properties, such as viscosity and surface tension, on the diameter of the melt-spun fibre, physical models associated with the melt spinning process are described. The melt spinning process can be separated into two parts: extrusion and drawing. Extrusion refers to the pressing of feedstock through the spinneret to form threads with a geometry defined by the orifices of the spinneret. Drawing refers to the pulling of the extruded thread to form fibres that are significantly thinner than the orifice diameter. Drawing is a combined effect of both the weight of the thread and the pulling force from the rotating drum. Discussion on extrusion and drawing can further be separated into cases for continuous and discontinuous flow.

2.4.1 CONTINUOUS FLOW IN EXTRUSION

In steady-state, continuous flow, predicting the flow rate of the extrusion process is a matter of determining the pressure drops across all the components. A sensible approximation is to assume

the spinneret is responsible for most of the pressure drop, and that the pressure drops of the other components are negligible. In that case, flow through the spinneret produces pressure drops from both simple shear and extensional flow. Entrance loss due to flow from a reservoir into the orifice is not accounted for, since there are other components in the vicinity of the spinneret that may influence that pressure drop. Geometry of a coni-cylindrical orifice is illustrated in Figure 2.5.

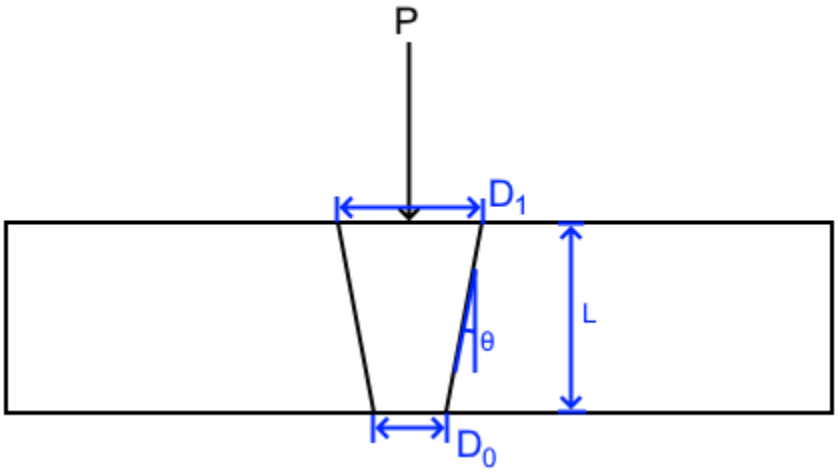

Figure 2.5: Schematic of coni-cylindrical orifice

Consider a power law fluid where the shear viscosity μ obeys $\mu = C\dot{\gamma}^{n-1}$, where $\dot{\gamma}$ is the apparent shear rate at the wall. The pressure loss due to shear in a coni-cylindrical orifice is given by Equation 2.1 [25].

Equation 2.1

$$P_s = \frac{2\mu\dot{\gamma}_0}{3n\tan\theta}\left(1-\left(\frac{D_0}{D_1}\right)^{3n}\right), \dot{\gamma}_0 = \frac{8v_0}{D_0}$$

The pressure loss in a coni-cylindrical orifice due to extensional flow is given by Equation 2.2, where μ_E is the extensional viscosity [25].

Equation 2.2

$$P_E = \frac{\mu_E \tan\theta\,\dot{\gamma}_0}{3}\left(1-\left(\frac{D_0}{D_1}\right)^{3}\right)$$

For a Newtonian fluid in laminar flow, the combination of these pressure losses P can be simplified to Equation 2.3, where $d = \frac{D_0}{D_1}$ and f_D is the Darcy-Weisbach friction factor for cylindrical pipes, equivalent to $\frac{64}{Re_0}$. This form is convenient to use since at $\theta = 0$ the equation reduces to the Darcy-Weisbach equation without a mathematical discontinuity. Note that α is strictly dependent on the geometry of the orifice.

Equation 2.3

$$P = \alpha f_D \frac{\rho v_0^2}{2}\left(\frac{L}{D_0}\right), \alpha = \left(\frac{d + d^2 + d^3}{3}\right)\left(1 + \frac{3}{8}\left(\frac{D_0}{L}\right)^2 \left(\frac{1-d}{d}\right)^2\right)$$

An important observation is that under laminar flow, the pressure loss is directly proportional to the exit velocity v_0 and v_0 is inversely proportional to the shear viscosity μ, since the above equation reduces to Equation 2.4. This relation holds true even for non-Newtonian fluids. In that case, α is not only dependent on orifice geometry but also the material parameter n. Given that the same material is melt-spun, α remains constant.

Equation 2.4

$$P = \frac{32\alpha\mu v_0 L}{D_0^2}$$

2.4.2 DISCONTINUOUS FLOW IN EXTRUSION

In the beginning of an extrusion process, or whenever continuous flow has suddenly ceased, continuous flow cannot start or resume until the pressing pressure overcomes the surface tension sustaining the meniscus inside the orifice (Figure 2.6). This capillary negative pressure P_{cap} is given by Equation 2.5, where ξ is the surface tension.

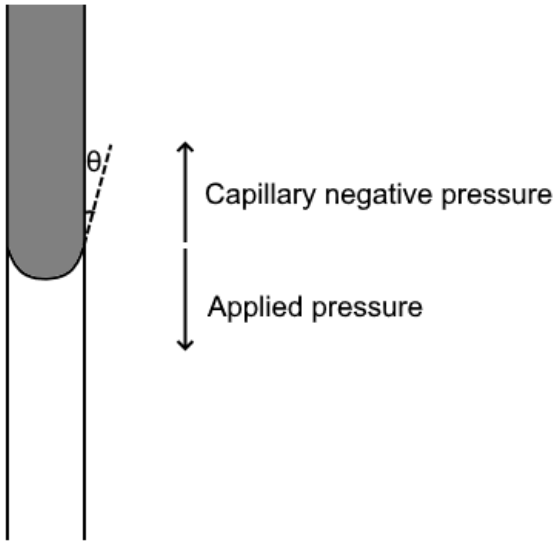

Figure 2.6: Capillary negative pressure caused by surface tension

Equation 2.5

$$P_{cap} = \frac{\xi \cos\theta}{D_0}$$

This equation demonstrates the importance of surface tension in an extrusion process, even if it doesn't play a role during continuous flow. It is possible to have a scenario where the pressing pressure is sufficient to sustain continuous flow but cannot overcome the surface tension required in discontinuous flow. In that case, extrusion is not possible.

2.4.3 CONTINUOUS FLOW IN DRAWING

Given that the melt can be continuously extruded, the continuity equation is conveniently expressed as Equation 2.6 if the assumption of incompressibility along the thread is entertained. The variables v_0, D_0, v_f, and D_f are the orifice velocity, orifice diameter, velocity at the uptake drum (uptake velocity), and uptake diameter (the diameter of the produced green fibre) respectively. This relation holds regardless of the thread profile between the orifice and uptake.

Equation 2.6

$$v_0 D_0 = v_f D_f$$

The above equation allows for the determination of v_0 indirectly without knowing the frictional losses h_L in Equation 2.7 since D_0 and v_f are known and D_f can be measured by microscopy. However, if D_f were to be predicted, the following system of equations must be solved [26].

Equation 2.7

$$\frac{\partial \sigma}{\partial z} = \rho\left(\frac{v\sigma}{\mu_E} - g\right) + \frac{4\tau_f}{D} + (2\xi + \sigma D)\left(\frac{\sigma}{v\mu_E}\right)$$

$$\frac{\partial T}{\partial z} = -\frac{4h}{\rho c_p v D}(T - T_\infty)$$

$$\frac{\partial v}{\partial z} = \frac{\sigma}{\mu_E}$$

$$\frac{\partial D}{\partial z} = -\frac{\sigma}{\mu_E}\left(\frac{D}{2v}\right)$$

The variables are defined as follows:

- z: distance along the thread from the orifice,
- σ: stress (in the direction of z),
- ρ: density of the thread,
- v: local velocity of the thread,
- μ_E: extensional viscosity, which is 3μ for a Newtonian fluid,
- g: gravitational acceleration constant,
- τ_f: skin friction due to air resistance,
- D: local diameter of the thread,
- ξ: surface tension,
- T: local temperature of the thread,
- T_∞: ambient temperature,
- h: convection coefficient,
- c_p: specific heat capacity of the thread.

The following boundary conditions are also imposed, where Z refers to the distance between the orifice and the uptake drum and T_{sp} is the spinning temperature.

Equation 2.8

$$D(0) = D_0, v(0) = v_0, v(Z) = v_f, T(0) = T_{sp}$$

Arguably, the strongest limitation of these differential equations is that the material parameters μ_E and ξ are not applicable once the thread has solidified. After solidification, the diameter, velocity, and stress of the thread remain approximately constant. Determining these material parameters over the entire range of temperatures and strain rates present throughout the thread line is also not a trivial task. The purpose of these equations in this work, however, is not to solve these differential equations, but to show the influence of fluid flow properties (density, viscosity, and surface tension) on the thread's stress, temperature, velocity, and diameter profile. A feedstock with a high surface tension would hasten the development of stress with z, and given the same z where solidification ends, would result in a higher peak stress in the thread. An increased viscosity would display a somewhat opposite trend. A thread with a higher peak stress may be more prone to breaking, and therefore fluid flow properties like surface tension and viscosity may carry serious implications on whether a continuous extrusion can be drawn into a thread continuously.

2.4.4 DISCONTINUOUS FLOW IN DRAWING

One of the phenomena in which a continuously drawn thread can break is fluid thread instability. This occurs when small perturbations in diameter along the thread grow, eventually leading to sections of the thread that break due to excessive extensional stress. Surface tension controls the driving force for surface area reduction which ultimately breaks up a thread into droplets. Consider a long cylindrical fluid thread with a radius r_0 held stationary at both ends. A small perturbation Δr is introduced so that the local radius r is described by Equation 2.9, where z is the distance along the thread. The growth rate ω of these perturbations for a viscous fluid in an inviscid environment like air can be described by Equation 2.10, where k is the wavenumber of the perturbation, r_0 is the initial radius of the thread, ξ is the surface tension of the fluid, μ is the shear viscosity of the fluid, and I is the modified Bessel function of the first kind [27].

Equation 2.9

$$r = r_0 + \Delta r \exp(\omega t + ikz)$$

Equation 2.10

$$\omega = \frac{\xi}{2r_0\mu}\frac{1 - k^2r_0^2}{k^2r_0^2 + 1 - k^2r_0^2I_0^2(kr_0)/I_1^2(kr_0)}$$

The most unstable perturbations correspond to when the magnitude of ω is largest, which occurs at the longest wavelengths. The most unstable perturbation when $k = 0$ is given by Equation 2.11.

Equation 2.11

$$\max(\omega) = \frac{\xi}{6r_0\mu}$$

Evidently, the surface-tension-to-viscosity ratio ξ/μ is an important parameter in the discussion of fluid thread instability. Yet, when applied to melt spinning, the application of a force to the end of a thread, extensional behaviour of the fluid (i.e. draw resonance), as well as the exchange of heat with the environment and diameter reduction along the thread renders this discussion of fluid thread instability rudimentary at best. Although more advanced models exist, the conclusion remains the same: surface tension is an important parameter in predicting discontinuous flow behaviour in melt spinning.

A continuously extruded green fibre can also break if it exceeds the breaking stress in the elastic or viscoelastic region of the thread. The way the fibre breaks in these regions can be further classified as brittle or ductile depending on whether necking occurs. Since the most unstable perturbations occur at long wavelengths leading to a reduction in diameter at distant intervals, ductile failure due to is difficult to distinguish from fluid thread instability. Figure 2.7 shows a typical stress profile throughout the thread. The stress gradient is ρg after solidification if air resistance is neglected [28].

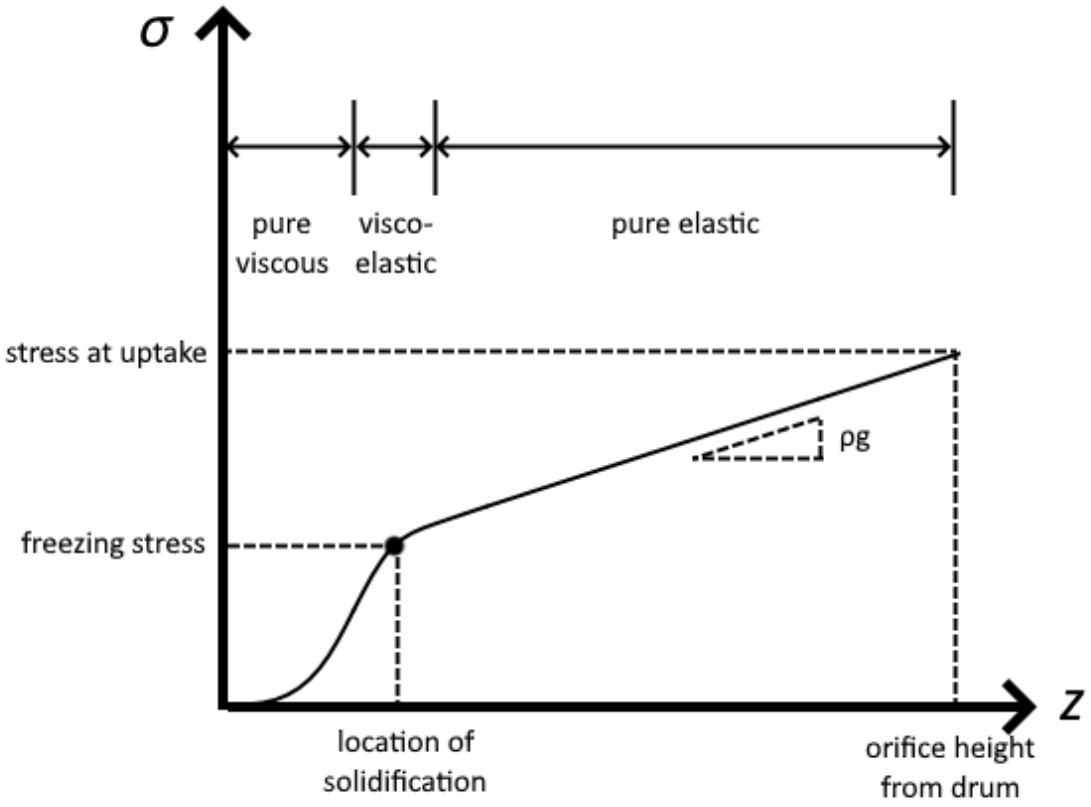

Figure 2.7: Typical stress profile along the thread

2.5 Definition of Spinnability

The same properties that affect the diameter of the produced green fibre can also affect whether the flow of material is continuous or discontinuous. Therefore, discussion of diameter variation cannot be separated from the subject of spinnability.

There is no consensus on the definition of spinnability. Many authors regard the draw ratio, the ratio between the final fibre diameter and the maximum diameter along the thread line [29]. The maximum diameter may be somewhat larger than the orifice diameter under the presence of die swell, which is the widening of the thread immediately after exiting the orifice due to restoration of elastic energy. Like the draw ratio, the ratio between extensional and shear viscosities, also known as Trouton's ratio, could be used as it is related to the draw ratio. However, the role of surface tension is not factored into these quantities, so it does not give the full picture on spinnability. Indeed, other definitions of spinnability are more verbose, citing additional criteria

such as a diameter tolerance or production requirements [30]. In this work, however, spinnability is specified at a set of operating parameters: ~260 °C spinning temperature, ~400 kPa pressing pressure, and 6.28 m/s uptake speed. Optimizing these parameters for spinnability is outside the scope of this work. The remaining descriptor for spinnability is a classification of whether the fibre can be collected by the uptake drum without supervision, with supervision (the user occasionally must pull the thread and wrap it around the drum), or not at all.

2.6 Reactions of Asphaltenes in Melt Spinning

Only a small extent of oxidation is required to drastically change the fluid properties (e.g., viscosity) of asphaltenes. Previous studies found that the spinning temperature increased within 24 hours of oxidation in air at 190 °C (autoxidation). Meanwhile, the viscosity of bitumen increases by two orders of magnitude even at low extents of oxidation [31]. Asphaltenes, the most polar component of bitumen, would be expected to oxidize the easiest, and therefore its viscosity would be even more sensitive to oxidation than bitumen is. To mitigate oxidation, a batch melt spinner must use an inert gas to supply the pressure, such as nitrogen or argon.

Asphaltenes can undergo reactions even under an inert environment. Asphaltenes are reported to have a persistent free radical content which, at spinning temperatures, can participate in various free radical reactions including combination, addition, hydrogen disproportionation, hydrogen transfer, and cracking [32, 33]. Cracking is typically accompanied by the generation of volatile compounds, although it is not expected to be kinetically significant at spinning temperatures (<300 °C) [32, 34]. These reactions are better summarized in Figure 2.8. The existence of reactions can lead to fluid properties that change with time, influencing the diameter of the produced green fibre.

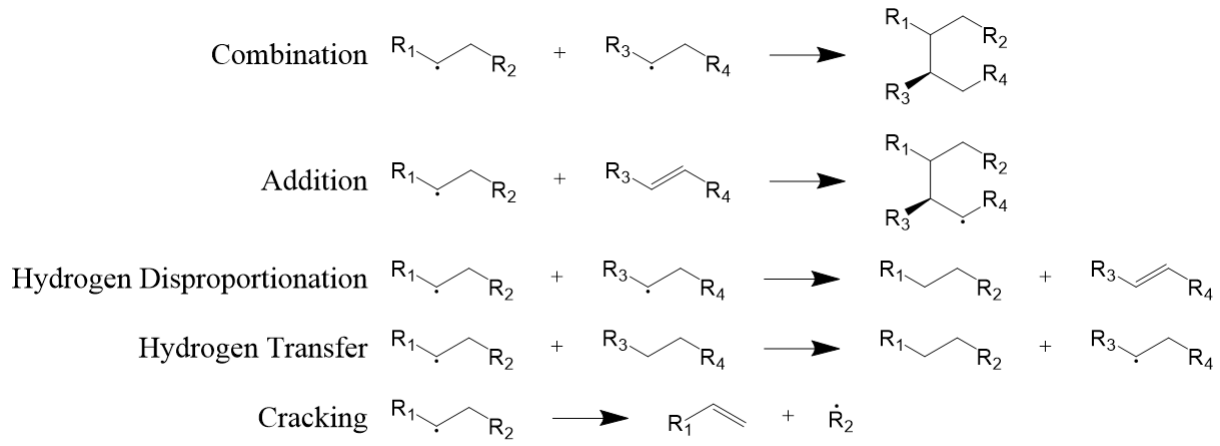

Figure 2.8: Examples of free radical reactions. Adapted from [32][1].

2.7 Weibull Statistics in Brittle Materials

The tensile strengths of brittle materials such as carbon fibres typically exhibit scatter that follow a modified Weibull distribution, which is justified by "weakest link theory," in which the weakest defect in a sample volume is responsible for the failure of the entire sample. The simplest formulation is given by P, the cumulative distribution function (Equation 2.12), i.e., the probability that failure of a sample volume V occurs at or below the failure stress σ_f. V_0 is the reference volume, σ_0 is the reference failure stress, and β is the Weibull modulus [5].

Equation 2.12

$$P = 1 - \exp\left(-\frac{V}{V_0}\left(\frac{\sigma_f}{\sigma_0}\right)^{\beta}\right)$$

Since the average tensile stress is not constant with sample volume, fibre strengths must be compared at a reference volume, chosen to correspond to a 5-mm length of 20-micron diameter fibre (0.00157 mm^3). The comparison of fibre strength reduces to estimating the parameters σ_0 and β. The Weibull modulus β is a measure of scatter in the data: the higher the β, the less scatter in σ_f and the less dependence of average tensile stress on sample volume. The standard

[1] This is an unofficial adaptation of an article that appeared in an ACS publication. ACS has not endorsed the content of this adaptation or the context of its use

method of estimating these parameters is by maximizing the log-likelihood function (a.k.a. maximum likelihood estimation or MLE), which is given by Equation 2.13.

Equation 2.13

$$\log L = \sum_i \left(\log \frac{\beta}{\sigma_0} \frac{V_i}{V_0} + (\beta - 1) \log \frac{\sigma_{fi}}{\sigma_0} - \frac{V_i}{V_0} \left(\frac{\sigma_{fi}}{\sigma_0} \right)^{\beta} \right)$$

A common way of visualizing the tensile data considers an alternate but equivalent linearized form of Equation 2.12, presented in Equation 2.14. Plotting the left-hand side as a function of $\ln \sigma_f$ is referred to "Weibull plots."

Equation 2.14

$$\ln(-ln(1-P)) - \ln \frac{V}{V_0} = \beta \ln \sigma_f - \beta \ln \sigma_0$$

Note that the precision of the Weibull parameters should not be interpreted from these Weibull plots, since those estimated parameters were used to produce the plot itself. Instead, contours representing a confidence level (e.g. 95%) better illustrate the precision of the estimated parameters. Confidence contours can be constructed by calculating numerous (β, σ_0) pairs where the likelihood ratio (i.e. log-likelihood difference) is

$$\Delta \log L = \log L(\beta^*, \sigma_0^*) - \log L(\beta, \sigma_0) = \frac{1}{2} \chi_\alpha^2(2),$$

where * denotes the optimal value when likelihood is maximized and $\chi_\alpha^2(2)$ is the chi-squared distribution with two degrees of freedom corresponding to the two Weibull parameters with a confidence level of $1 - \alpha$.

3 EXPERIMENTAL METHOD

3.1 Description of Batch Melt Spinner

A schematic of the batch melt spinner is shown in Figure 3.1. Details of the box, spinneret, and components are illustrated in Figure 3.2.

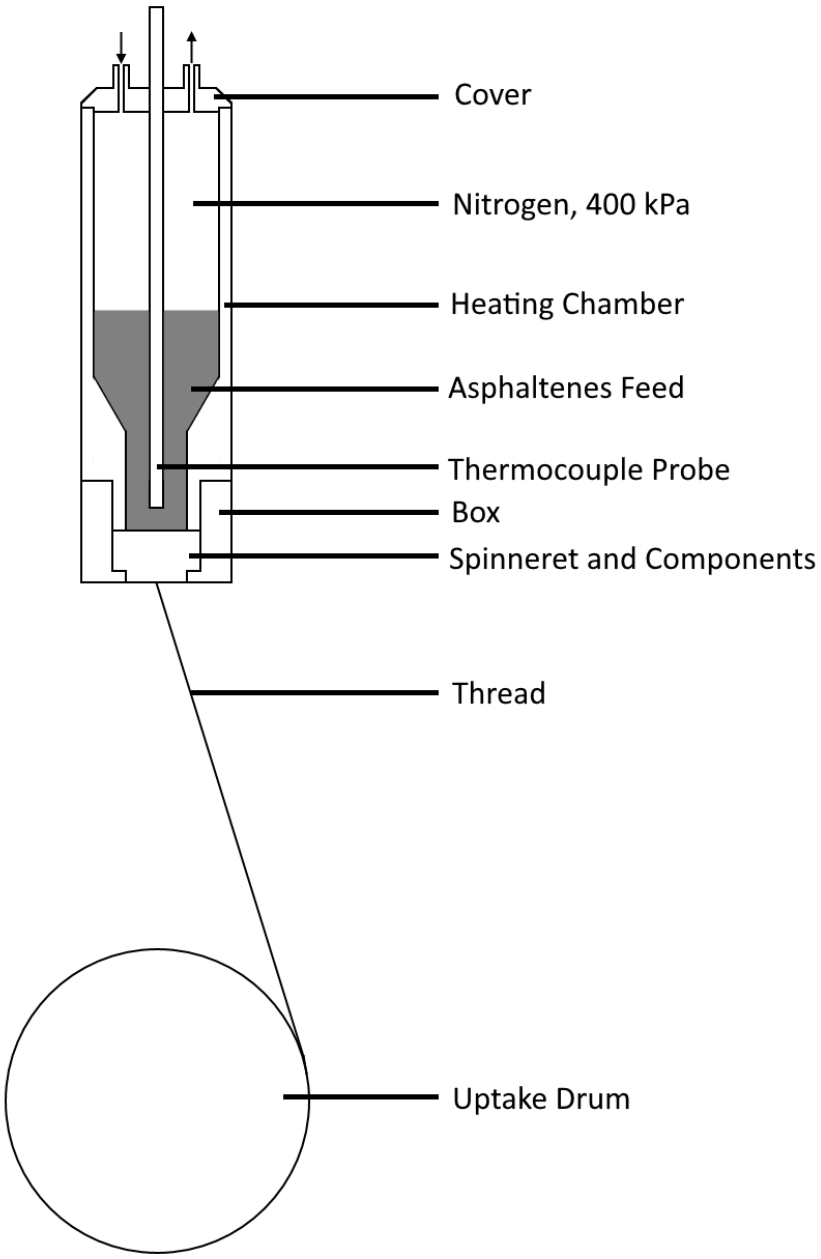

Figure 3.1: Schematic of batch melt spinner (not to scale)

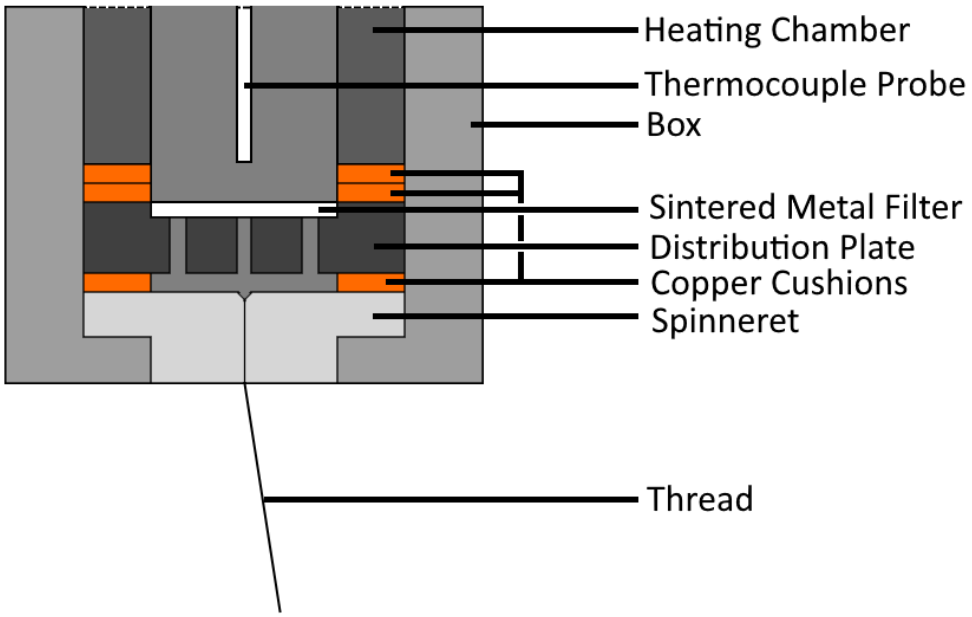

Figure 3.2: Details of box, spinneret, and components (not to scale)

3.2 Default Procedure for Melt Spinning Fractions of Green Fibres

14.5 grams of an asphaltenes feed, ground in a mortar and pestle, was loaded into the melt spinner (Anytester AT2225). The feed was softened at a probe temperature of 258 °C inside the heating chamber by setting the temperature of the heating coils to 250 °C. The discrepancy between the set and probe temperatures is due to both instrument error as well as the exothermicity of present asphaltenes reactions, and the set temperature can vary by a few degrees depending on the feed used. Once the probe temperature reaches the spinning temperature, the drum speed was set to 600 RPM (6.28 m/s thread uptake speed) and the feed is pressed through a spinneret with 0.3 mm orifice diameter with nitrogen at 400-420 kPa gauge pressure. At 5-minute intervals, the thread is manually broken, and the drum is stopped to collect fractions of green fibres that corresponded to different elapsed times since the increase of pressure.

3.3 Materials and Nomenclature

Solvent de-asphalted asphaltenes (SDA) with a C5-insoluble:solubles ratio of 40:1 was supplied by China National Offshore Oil Corporation Limited. From a single industrial batch. Various treatments and spinning variations are carried out on these untreated asphaltenes:

- SDA-x: SDA was heat-treated in a tube furnace at a hold temperature of x °C for 2 hours after a ramp-up of 1.5 °C/min. x is either 240, 260, or 280 °C.
- SDA-x-24: like SDA-x, but with a holding time of 24 hours.
- SDA-del$y$: Untreated asphaltenes were heated in the melt spinner to the spinning temperature and then held for y minutes before increasing the pressing pressure to begin spinning. y is either 10 or 20 minutes.
- SDA-THF: Untreated asphaltenes were dissolved in tetrahydrofuran (THF) and boiled at 75 °C for 12 hours in an oil bath. The product was then dried by rotary evaporation and vacuum-heated at 50 mbar and 60 °C until brittle solid remained.
- SDA-THF-260: SDA-THF was heat treated at 260 °C, in the same manner as SDA-260.

3.4 Semi-Automatic Measurement of Diameters with DiameterJ

Scanning electron microscopy (SEM) images of the fibres were taken with a Zeiss Sigma 300 VP-FESEM. The diameters of these fibres were determined semi-automatically with DiameterJ, modified to better suit the needs of this work, to produce diameter distributions for each fraction. The change of the diameter distributions over the fractions is referred to as “diameter distribution evolution” (DDE).

The workflow of semi-automatic diameter measurement in SEM images consists of three steps: image filtering, segmentation, and then the DiameterJ algorithm [35]. The goal of image filtering is to remove noise in the images that would interfere with the segmentation algorithms. Non-local means denoising using the Python OpenCV library (fastNLMeansDenoising) was used on each image to produce a filtered image with little noise but preserved fibre edges [36]. The parameters for fastNLMeansDenoising (h=10, searchWindowSize=21) were chosen by trial and error. The grayscale of the filtered image was then pre-segmented to a black and white mask (white representing the fibres and black representing the background) using DiameterJ’s built-in statistical region merging and mixed algorithms. For each image, a suitable pre-segmented image

was manually chosen and edited to remove irregularities such as contaminants, mis-segmented fibres, and low-angle intersections that could lead to significant errors in the diameter distribution. Some images were poorly pre-segmented, so the filtered images were manually segmented using GIMP's foreground select tool. Then, the modified DiameterJ algorithm is run to get a distribution of fibre radii for a series of images corresponding to each fraction. An example of this workflow is illustrated in Figure 3.3.

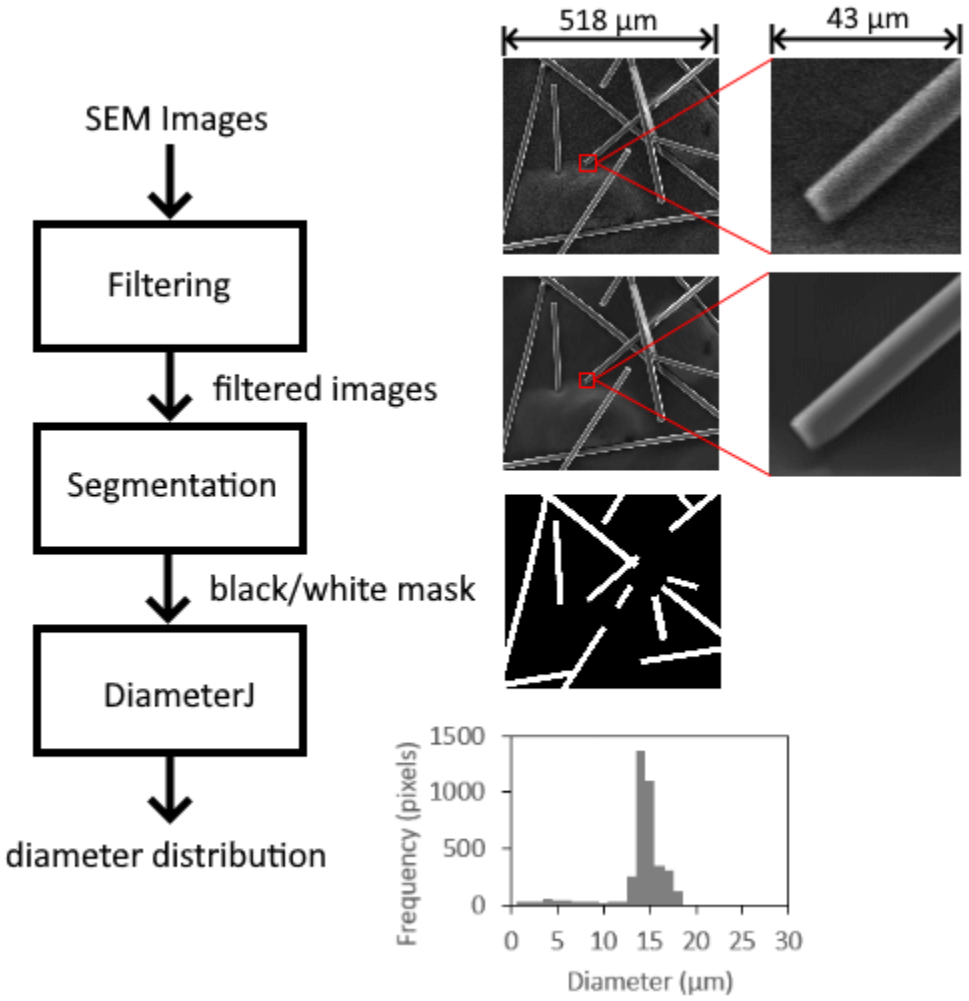

Figure 3.3: DiameterJ workflow

This method of determining the diameter distribution, although much faster than measuring the diameters manually, is prone to a systematic "false" peak in the lower end of the diameter distribution. The part of the distribution associated with the false peak should be discounted in the analysis of summary statistics.

3.5 Thermogravimetry

Understanding the weight loss and heat of a reaction gives us valuable clues about the nature of the reaction. Thermogravimetric analysis was conducted with a Mettler Toledo TGA/DSC1 equipped with a LF1100 furnace and MX5 microbalance having a measuring range of 5 g and 1 µg readability. Flowing argon was supplied to the instrument at 40 mL/min for both the sample and the reference. The samples were heated to 260 °C at 20 °C/min and then held at that temperature for five hours.

3.6 Nuclear Magnetic Resonance Spectroscopy

^{1}H and ^{13}C nuclear magnetic resonance spectroscopy (NMR) were conducted with a 400 MHz Varian Unity Inova spectrometer by the Analytical Services of the Chemistry Department at University of Alberta. For ^{13}C NMR, the measurements were conducted without nuclear Overhauser enhancement by using chromium (III) acetylacetonate as a relaxation agent and setting up decoupling on during spectra acquisition. NMR spectra was used to quantify aliphatic and aromatic content in the asphaltenes. More details can be found in Appendix C.

3.7 Capillary Rheometry

To assess the evolution of viscosity with time, rheometry was carried out with the Rosand RH2000 from Netsch by Thread Innovations Ltd. The feed is heated to either 255, 260, or 265 °C and held at that temperature for one hour while a piston gradually pushes the feed out the die (1 mm diameter, 32 mm length, 180° entry angle) at a constant speed corresponding to a 0.5 s^{-1} shear rate. A transducer measures the piston pressure which is analogous to viscosity. Determining viscosity accurately from pressure requires Bagley corrections by extrapolating measurements obtained at varying die lengths. These additional experiments are not conducted as part of this study.

3.8 CHNS-O Analysis

CHNS-O Flash 2000 from Thermo Fisher Scientific with a 2,2-(2,5-Thienediyl)bis[5-(2-methyl-2-propanyl)-1,3-benzoxazole (BBOT) standard was used to characterize the carbon, hydrogen, sulphur, and oxygen content of green fibre fractions. Analysis includes the run of two tin capsule

blanks, 3-point calibration measurements and an unknown run using BBOT to validate the calibration of the chromatograph.

3.9 Pycnometry

The simplest method of measuring densities is using a liquid pycnometer. This method relies on Archimedes' principle. Four masses must be determined:

1) empty pycnometer
2) pycnometer filled with a liquid
3) pycnometer with solid sample
4) pycnometer with solid sample and then filled with the liquid in (2)

The accuracy of this type of pycnometry is contingent on the liquid having no interaction with the bulk of the fibre, yet completely wets the fibre. Any gas bubbles trapped will also have a significant influence on the calculated density. Alcohols can wet the green fibres completely, but the rapid evaporation of ethanol leads to large errors in the measured mass. Propylene glycol and glycerin are more suitable candidates for liquid pycnometry, but the high viscosity of glycerin causes trapped bubbles to become difficult to remove. Therefore, propylene glycol was selected as the liquid to carry out liquid pycnometry of green fibre fractions. There is no guarantee that propylene glycol does not cause swelling or shrinking of the green fibres, so it is only regarded as an estimate of the bulk density of the samples. Using the four mass measurements listed above, the working equation of liquid pycnometry is:

Equation 3.1

$$\frac{\rho_s}{\rho_l} = \frac{m_{p+s} - m_p}{\left(m_{p+l} - m_p\right) - \left(m_{p+s+l} - m_{p+s}\right)}$$

where ρ and m is density and mass respectively, and the subscripts s, l, and p correspond to sample, liquid, and pycnometer. The form shown below, derived from differentiation of Equation 3.1, is useful for combining mass measurement uncertainties Δm for error analysis.

Equation 3.2

$$\frac{\Delta\rho_s}{\rho_s} = \left(\frac{1}{m_{p+s+l} - m_{p+s}} - \frac{1}{(m_{p+l} - m_p) - (m_{p+s+l} - m_{p+s})}\right)(\Delta m_{p+s} + \Delta m_p) + \frac{\Delta m_{p+l} + \Delta m_{p+s+l}}{(m_{p+l} - m_p) - (m_{p+s+l} - m_{p+s})}$$

Liquid pycnometry is advantageous since relatively little sample volume is required. In these experiments, the pycnometer size was 2 mL and at least 10 mg of fibre is tested for each fraction. Each mass is measured 5 times and the representative value is taken as the average except for measurements with propylene glycol. Even though propylene glycol evaporates slowly, over the course of 5 measurements the masses with liquid typically decreased by 1 mg. Correcting for evaporation is necessary since a low sample volume is used and is conducted by linear regression between the sample number and the measurement and taking the estimated mass of the first sample as the representative value.

Meanwhile, the true density of the material is typically determined by "helium pycnometry." Helium, unlike propylene glycol, can penetrate open pores. A gas pycnometer measures the volume of gas displaced by the sample, which the density is determined from given a known mass. This method is also non-destructive, and the fibres could be reused for subsequent experiments. Helium pycnometry was conducted using the AccuPyc II 1340 Pycnometer from Micromeritics. The volume of displaced gas was measured at an equilibrium rate of 17 Pa/min. At least five measurements are made for each fraction.

3.10 Infrared Spectroscopy

Fourier-Transform infrared spectroscopy (FTIR) was taken with the Nicolet is50 and Nicolet Summit models from Thermo-Fischer Scientific in the attenuated total reflectance (ATR) mode on a diamond crystal. All spectra were an accumulation of at least 32 scans at 4 cm^{-1} resolution.

3.11 Oxidation and Carbonization of SDA Green Fibres

To gauge the influence of diameter non-uniformity on the final mechanical properties of a carbon fibre, oxidative stabilization and carbonization were carried out on green fibres of untreated

asphaltenes. The carbonized fibres were not subsequently graphitized, and the tensile strength of carbonized fibres was taken as a measure of the mechanical performance.

To stabilize green fibres, a 100-mg bundle is submersed in at least 100 mL of 1:1 ratio of 15 %v/v nitric acid to ethanol for 10 minutes, followed by heating without prior drying at 1.5 °C/min to 300 °C in a tube furnace and holding for 2 hours in an air flow of 0.4 L/min (0.1 m/s). The fibres were furnace-cooled to room temperature.

Carbonization of the oxidized fibres was carried out in a nitrogen environment, heated at 1.5 °C/min from ambient temperature to 60 °C to give sufficient time to purge any oxygen in the tube, followed by a ramp up of 3 °C/min to 1500 °C and then holding for 2 hours. The fibres were allowed to furnace-cool to room temperature.

Although the procedure above has not undergone rigorous optimization, A difference in mechanical performance in different fractions would extend the same conclusion to a process that is optimized. Optimizing the oxidation and carbonization processes is not within the scope of this work.

3.12 Tensile Testing of Carbonized Fibres

The preparation of single fibre tensile specimens was achieved by isolating and adhering a single strand of carbonized fibre onto custom-cut cardstock using UV resin. A schematic of the specimen paper and preparation is shown in Figure 3.4. Laser diffraction was used to determine the diameter of the single fibres. Diameters determined this way were calibrated by correlation with diameters measured via scanning electron microscopy. Tensile tests were then carried out with the Newton from TestResources[2] at a strain rate of 0.05 min^{-1}. More details about tensile specimen preparation and testing are provided in Appendix 3.

[2] Actuator: DG1000 lbf; force transducer: SMT1-2.2-294

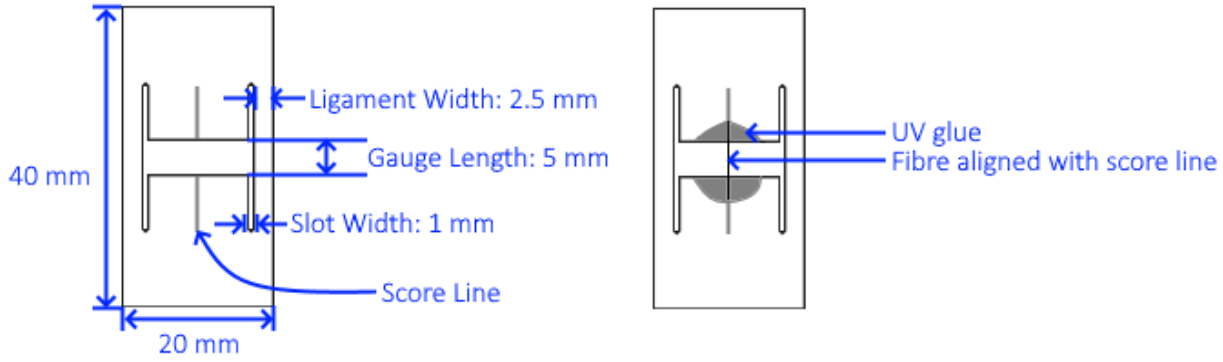

Figure 3.4: Single fibre tensile specimen geometry and preparation

4 RESULTS AND DISCUSSION

4.1 Diameter Distribution Evolution (DDE) of Green Fibre Fractions of Untreated Asphaltenes

As-received solvent de-asphalting asphaltenes were melt spun by heating the asphaltenes to ~260 °C and pressing it through a spinneret with nitrogen (~400 kPa pressing pressure)[3]. Details on the melt spinning process are better described in Section 3.2. The spinning was paused in set intervals (~5 min) to collect fractions of green fibres. The diameter distributions of the collected green fibre fractions are obtained by semi-automatically analyzing SEM images via the DiameterJ algorithm, as described in Section 3.4. A ridge plot showing the green fibre diameter distributions of the fractions is shown in Figure 4.1. The timeframe of each fraction is labeled on the baseline of each distribution, and the position of the baseline corresponds to the midpoint of the timeframe.

[3] The exact spinning temperature fluctuated between 255 and 260 °C and the pressing pressure was kept between 400 and 420 kPa.

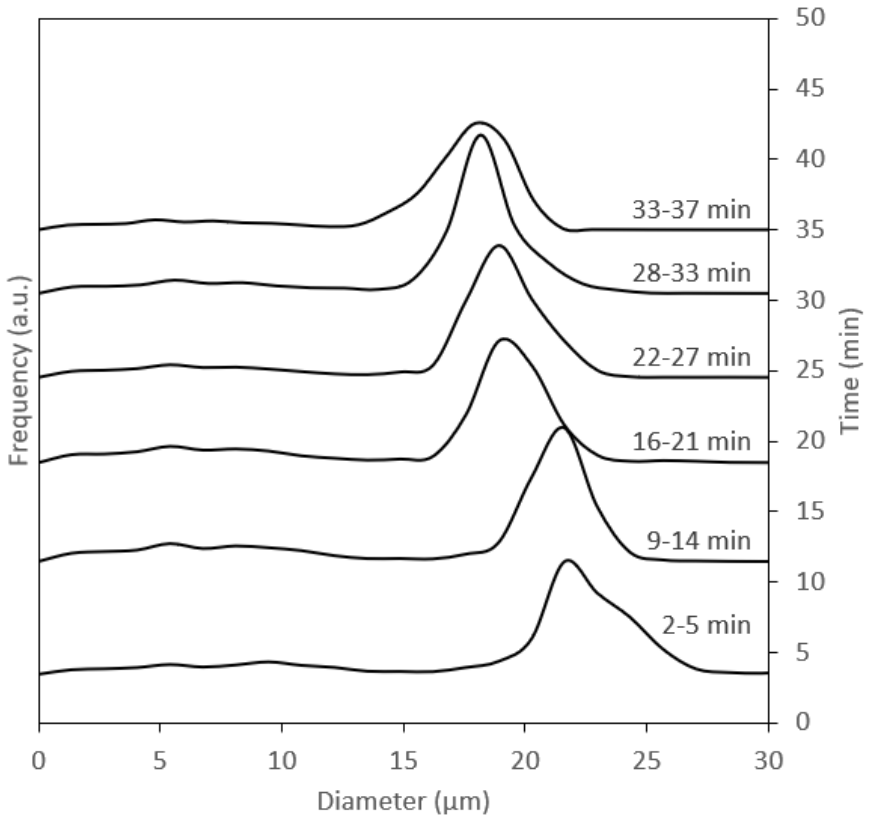

Figure 4.1: Ridge plot of green fibre fraction diameters spun from untreated asphaltenes

A decrease in peak diameter from 22 to 18 microns (17% decrease) is observed throughout the spinning. This extent of thinning is, in theory, detrimental to the consistency of processes occurring after melt spinning. For example, oxidative stabilization is a diffusion-limited process. The distance which a diffusive particle traverses (oxygen in this case), as described by random walk theory in three dimensions, can be related to kinetics by Equation 4.1, where $\langle x^2 \rangle$ is the mean square distance traversed by the diffusive particle, D is diffusivity, and t is time.

Equation 4.1

$$\langle x^2 \rangle = 6Dt$$

The major limitation of random walk theory is that it does not consider particle collisions. Nonetheless, it illustrates the dependency of diffusion-controlled processes with distance. At a

given temperature, the expected distance which a particle traverses scales with the root of time. Applied to green fibres, the oxygen must be given enough time to reach from the surface to the core of the fibre and react with the asphaltenes. However, since under-oxidation and over-oxidation of the green fibres should be avoided, as it is associated with brittleness [24], a uniform green fibre diameter is an important prerequisite for consistency in oxidative stabilization. A failure to achieve this consistency in stabilization ultimately is reflected in poor mechanical properties of the final carbon fibre or an excessive loss of yield during carbonization [24].

It is interpreted that the evolution of diameter with time is due to changes in the feedstock's material properties, since environmental and operating conditions are controlled. As the changes in diameter occur gradually over the course of spinning, reactions are likely responsible for these changes. The reactions could be physical and/or chemical. Physical reactions include phase separation between lighter and heavier components, and the boiling of volatile compounds. The main chemical reactions in the asphaltenes feedstock are free radical reactions described in Section 2.6, since an inert gas is supplied to the heating chamber. These free radical reactions can lead to the formation of carbon-carbon double bonds from single bonds, production of volatiles due to cracking, and cross-linking which increases the molecular weight of asphaltenes.

Another observation that could be made is that some green fibre fractions exhibit a broader diameter within the fraction itself. For example, the second fraction (9-14 min) has the highest interquartile range of the fractions, at 3.28 microns, while the fifth fraction (28-33 min) has an interquartile range of only 2.34 microns. The differences in diameter variation within each fraction could be due to one or more reasons, including:

- oscillating flowrates due to machine vibration,
- discontinuous phenomena such as fluid thread instability or thread breakage,
- variation in fluid properties due to material heterogeneity,
- differences in the rate of diameter decrease or fraction timeframe.

4.2 Characterizing Green Fibre DDE as a Method of Examining Fluid Properties

To assess how changes in the feedstock's material or fluid properties lead to the observed diameter evolution, the flowrates at the spinneret orifice and at the uptake are considered. The flowrate at the orifice is connected to the asphaltene's fluid properties, but the green fibre diameter is associated with the flowrate at the uptake. To connect the two, consider the conservation of mass at the orifice an uptake of a continuous thread in Equation 4.2, where $\dot{m}$ is mass flow rate, ρ is density, v is thread velocity, and D is diameter The subscripts 0 and f represent the orifice and uptake respectively.

Equation 4.2

$$\dot{m} = \rho_0 v_0 D_0^2 = \rho_f v_f D_f^2$$

This green fibre diameter is considered an approximation of D_f, and is valid if negligible elastic strain due to drawing is recovered. Since ρ_0, D_o, and v_f do not change throughout the spinning, and ρ_f is not expected to change significantly with diameter, the green fibre diameter is a representation of the orifice velocity v_0. It has been shown in Section 2.4.1 that given the same pressing pressure and D_0, v_0 is inversely proportional to the feedstock's viscosity.

Since a reduction of green fibre diameter is associated with increasing viscosity, the next question is whether this increase in viscosity with time is attributed to reversible or irreversible processes. In the ideal reversible process, a cooling step after heating would completely revert any physical or chemical changes that had occurred during the heating stage, given that cooling is carried out slowly. If the reactions occurring during melt spinning are irreversible, then heat treatment at around the spinning temperature would be effective at mitigating the observed diameter thinning, and therefore reduce the diameter variation of the batch overall. However, if the process is reversible, then heat treatment would be ineffective, and instead, delaying the beginning of spinning would be the more appropriate measure to reducing diameter thinning, since there would be no cooling step involved.

While it is apparent that there is a time dependence on the DDE of green fibres, changes in the peak diameter of green fibres can also be random. Meanwhile, the observed variation within

each fraction (intra-fraction variation) is also not independent of the observed diameter thinning. It is therefore necessary to separate the observed DDE into time-dependent (thinning) and time-independent (fluctuation) components to quantify the significance of each contribution. While thinning can be caused by changes in viscosity due to reversible or irreversible reactions, physical or chemical, fluctuation is either a sign of discontinuous effects such as fluid thread instability or inherent inhomogeneity in the feedstock's viscosity. This differentiation is also required to compare the effectiveness of heat treating and delayed spinning at reducing diameter thinning, which will be discussed later. The average median diameter is also included as it gives an idea of the average viscosity over the course of spinning.

To characterize the decreasing diameter with time, relative thinning rate is defined as

Equation 4.3

$$\text{Relative Thinning Rate} \equiv \frac{-dD_f/dt}{D_f} \approx -\frac{\text{slope of representative diameter}}{\text{intercept of representative diameter}}$$

The representative diameters chosen are the median diameters of the fractions. The median was chosen over the peak diameter or the average diameter since it is sensitive to the shape of the diameter distribution but insensitive to outliers. This quantification of thinning is directly tied to the physics of melt spinning. It follows from Equation 2.4 and Equation 2.6 that given the same pressing pressure, orifice diameter, and thread uptake speed,

Equation 4.4

$$2\frac{-dD_f}{D_f} = \frac{dv_0}{v_0} = \frac{d\mu}{\mu}$$

Therefore, relative thinning rate is also a measure of the relative increase in viscosity.

Apart from the steady diameter decrease with time, the first and last fractions seem to exhibit a broader distribution. These fractions were obtained from a single melt spinning with a thread, so a distribution is not relevant in a plot of instantaneous thread diameter as a function of time. The presence of variation within each of the fractions point to random fluctuations in diameter within the duration of a fraction. However, less diameter variation in a fraction does not necessarily

entail less fluctuation. It could be the case that these fluctuations occur over a longer time, leading to narrow diameter distributions within a fraction, but more fluctuation between fractions. The diameter variation of the fractions all combined can still be high. Using the sum of variances to account for both intra-fraction and inter-fraction variation, "fluctuation" is proposed as:

Equation 4.5

$$\text{Fluctuation} \equiv \frac{1}{E(\overline{D}_f)}\sqrt{Var(\overline{D}_f - \widehat{D}_f) + E\left(Var(D_f)\right) - \frac{1}{12}\left(E(\Delta t)\frac{dD_f}{dt}\right)^2}$$

where $\overline{D}_f$ is the observed representative diameter of a fraction, $\widehat{D}_f$ is the estimated diameter, t is time, and Δt is the duration of a fraction. The representative diameter chosen is the median diameter. The term $\text{Var}(\overline{D}_f - \widehat{D}_f)$ accounts for variance between fractions while $\text{E}(\text{Var}(D_f))$ accounts for variance within fractions. The third term discounts the contribution of a constant thinning (uniform distribution) to the variance within fractions.

In the melt spinning of untreated asphaltenes, the relative thinning rate and fluctuation of green fibres can be calculated from the data presented in Figure 4.1 (also tabulated in Appendix A.1). The values of relative thinning rate and fluctuation are 38% and 24.9% respectively. The average median diameter of the green fibre fractions was 18.8 microns. Both time-dependent and time-independent components of green fibre diameter variation are significant. Therefore, understanding the mechanism of both thinning and fluctuation is crucial to unlocking the solution to control diameter variation in melt-spun green fibres.

4.3 Effect of Prior Heat Treatment on DDE

A variety of reactions are kinetically significant around spinning temperatures. If these reactions are non-reversible, then it was thought that heat treatment would lead to a feedstock that was closer to its equilibrium state. This would mitigate thinning of the thread line with time. However, reactions that change the molecular weight of asphaltenes could lead to a broader molecular weight distribution, likely leading to a larger fluctuation in green fibre diameter and can even have a negative impact on spinnability.

Heat treatment was carried out by heating as-received SDA to 240, 260, or 280 °C at 1.5 °C/min and holding for 2 h before furnace-cooling to room temperature. The nomenclature for the resulting precursors is SDA-x, where x corresponds to the holding temperature. The heat-treated feedstocks were then melt-spun under the same conditions (pressing pressure, spinning temperature, and uptake velocity) prescribed for untreated SDA in Section 4.1. The spinning was intermittently paused to collect 5-minute fractions and their diameter distributions were similarly measured with DiameterJ from SEM images. The median diameter evolutions of treated and untreated feedstocks are compared in Figure 4.2. The diameter distribution evolutions are characterized and quantified in Table 4.1.

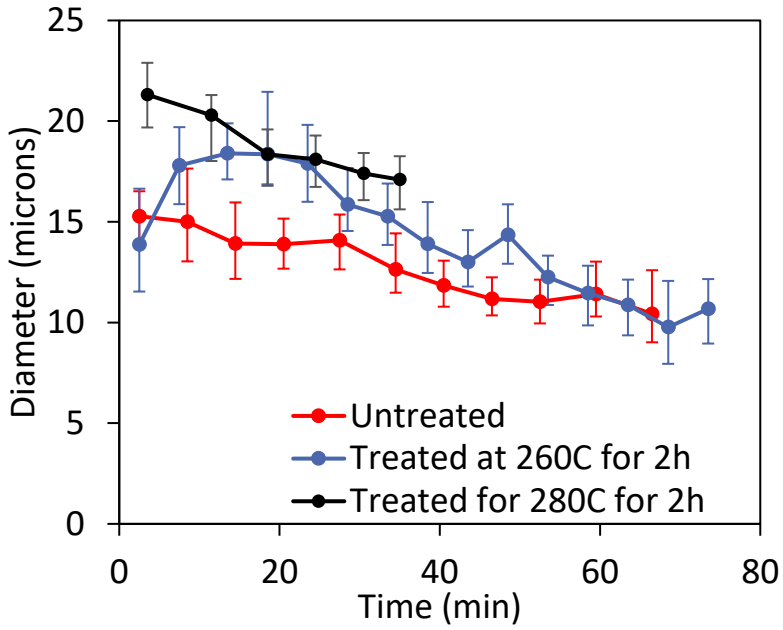

Figure 4.2: Median diameter evolution of heat-treated and untreated asphaltenes. All precursors were spun at 260 °C. The error bars denote quartiles.

Table 4.1: Diameter distribution evolution characterization of SDA and SDA-x fractions

Precursor	Pre-treatment Hold Temperature and Time*	Relative Thinning Rate	Average Median Diameter	Fluctuation
SDA	N/A	38%/h	18.8 µm	24.9%
SDA-260	260 ˚C, 2 h	42%/h**	14.3 µm	22.6%
SDA-280	280 ˚C, 2 h	30%/h	12.8 µm	24.1%

*All heat treatments were conducted with a ramp-up rate of 1.5 ˚C/min

** first point excluded from linear regression. The low diameter of the first point may be due to incomplete melting of the feedstock.

It is evident from these results that heat treatment decreases the average median diameter of the fibre fractions, which confirms the existence of irreversible reactions. This would likely correspond to the median diameter of the produced green fibre had it not been separated into fractions. It is interpreted that the average viscosity of the molten feedstock increases with time at a constant temperature, which could be attributed to cross-linking of the asphaltenes during heat treatment.

4.4 Physical and Chemical Changes During Heat Treatment and Melt Spinning

Another clue that points to irreversibility of asphaltenes reactions at spinning temperatures is evident when examining the weight losses of heat treatments, shown in Figure 4.3. All heat treatments were subject to a ramp-up rate of 1.5 °C/min from room temperature. While there was an insignificant mass loss associated with heat treatment of asphaltenes, a clear trend was still observed that the yield decreases with increasing holding temperature and time.

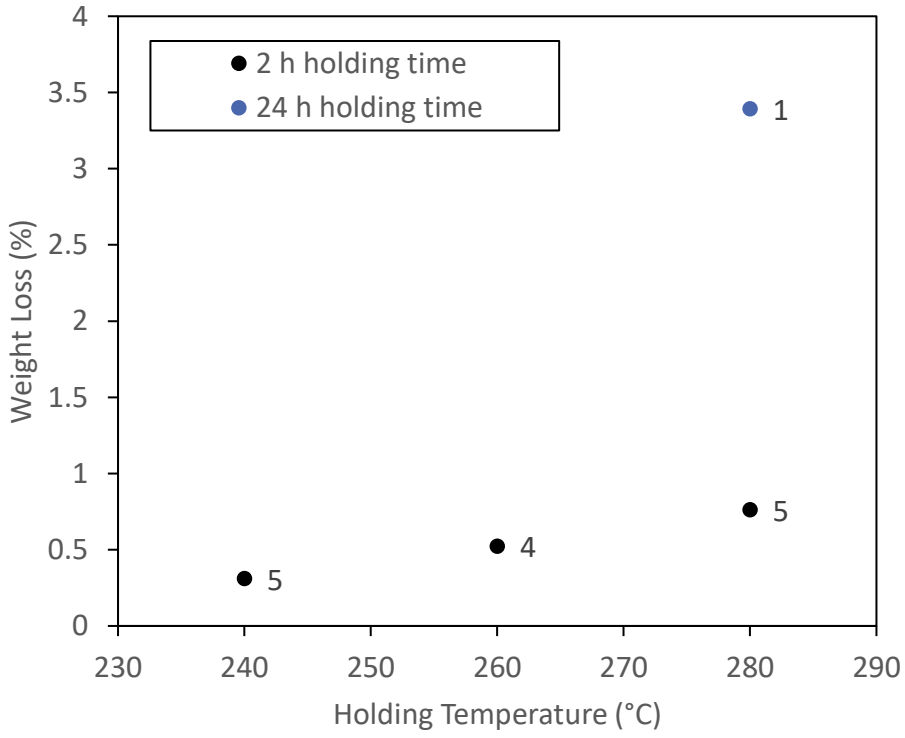

Figure 4.3: Average weight losses due to SDA heat treatments. The number beside each points denotes the number of samples from which an average is taken.

Since the heat treatments are conducted in an inert environment, the mass losses must be due to the escape of volatiles in the asphaltenes either through pre-existing volatile matter or generation of volatiles through, for example, cracking reactions. However, if only the former is true, it would be expected that the volatiles should be completely removed after the two hours of heat treatment. Pre-existing volatile matter likely cannot explain the increasing mass loss with holding temperature. Although only a small mass of volatiles escapes the samples, it translates to a significant volume amount. This is evident as bubbles or pockets appear on the surface of the asphaltenes samples during heat treatment and remain after solidification.

To quantify the evolution of volatiles during spinning, thermogravimetry was conducted. The experimental method also combines thermogravimetry with calorimetry to provide clues to the type of reaction that takes place. The apparatus consists of a sample and reference crucible. The reference crucible is heated up at set heating rate and the heat flow between the reference and sample, as well as the weight of the sample, are measured. Two variables are of interest: specific heat flow, which is the heat flow per unit mass of sample, and weight fraction with respect to the initial weight. Thermogravimetry isotherms refer to heat flows and weight fractions as a function of time under constant sample temperature and are presented in Figure 4.4. For each feedstock, the reference was heated at a rate of 20 °C/min to 260 °C and held for 5 hours. The specific heat flow (red) and weight fraction (black) is recorded and plotted with time. Each plot of specific heat flow started negative, denoting that energy must be supplied to heat the sample from room temperature to the hold temperature. As the temperature rose for the next 12 min., the specific heat flow increased, suggesting the onset of exothermic reactions. The specific heat flow appeared to reach an equilibrium quickly once the hold temperature was reached. Therefore, the first 15 minutes is regarded as a transient period that doesn't reflect the sample's isothermal behaviour. Meanwhile, the weight fraction increased slightly before decreasing again during the transient period, which could be due to oxidation due to residual oxygen around the sample. The weight fraction continued to decrease after the transient period and was not stabilized even at 5 hours.

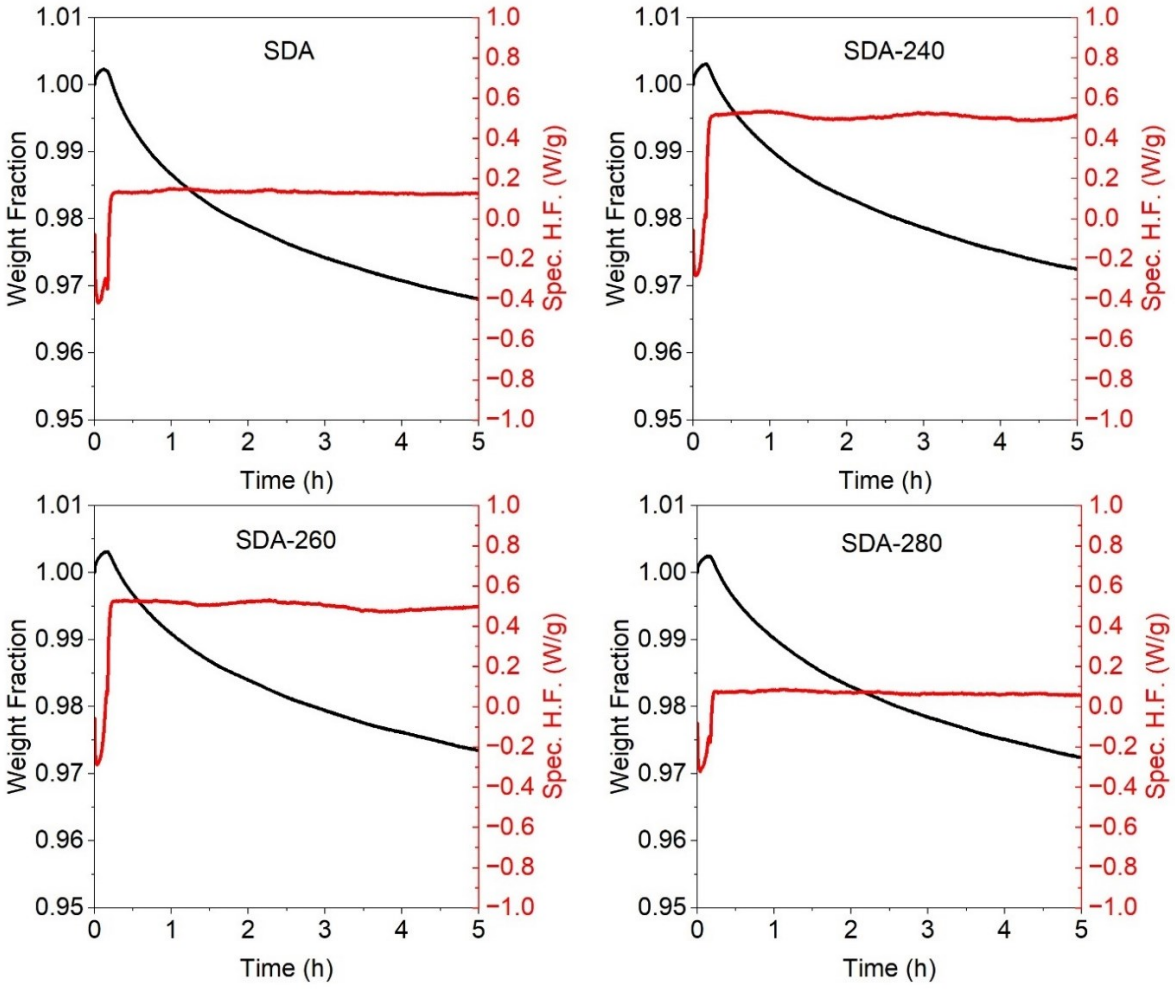

Figure 4.4: Isotherms of SDA and SDA-x at 260 °C

To better visualize comparisons of the isotherms among treated and untreated SDA, two quantifications are considered: the stable specific heat flow at 260 °C and the weight loss at 2 hours. Figure 4.5 and Figure 4.6 compare these quantifications as a function of holding temperature.

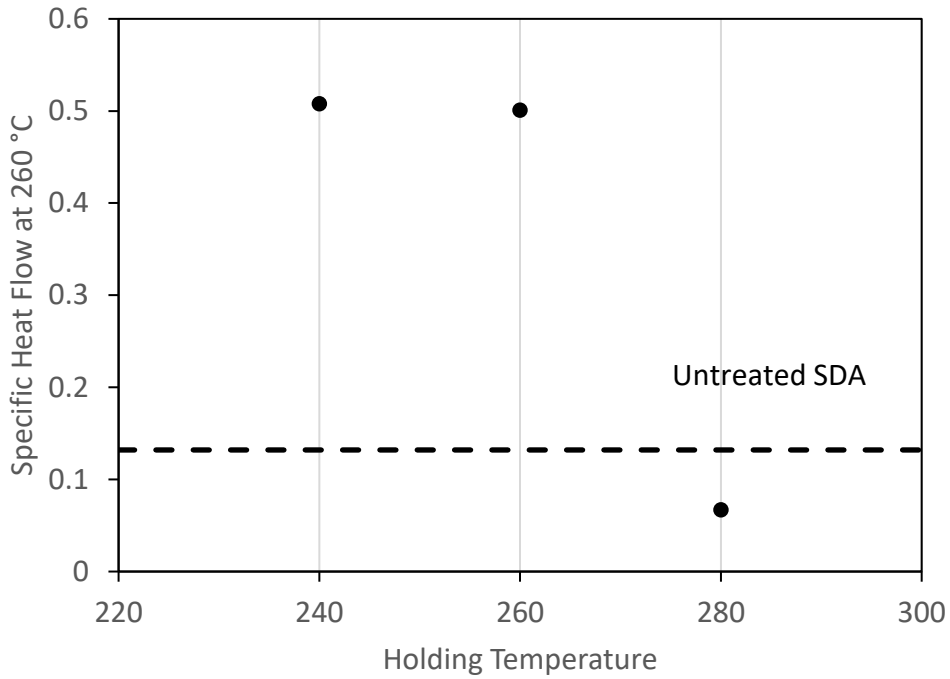

Figure 4.5: Specific heat flow at 260 °C as a function of holding temperature.

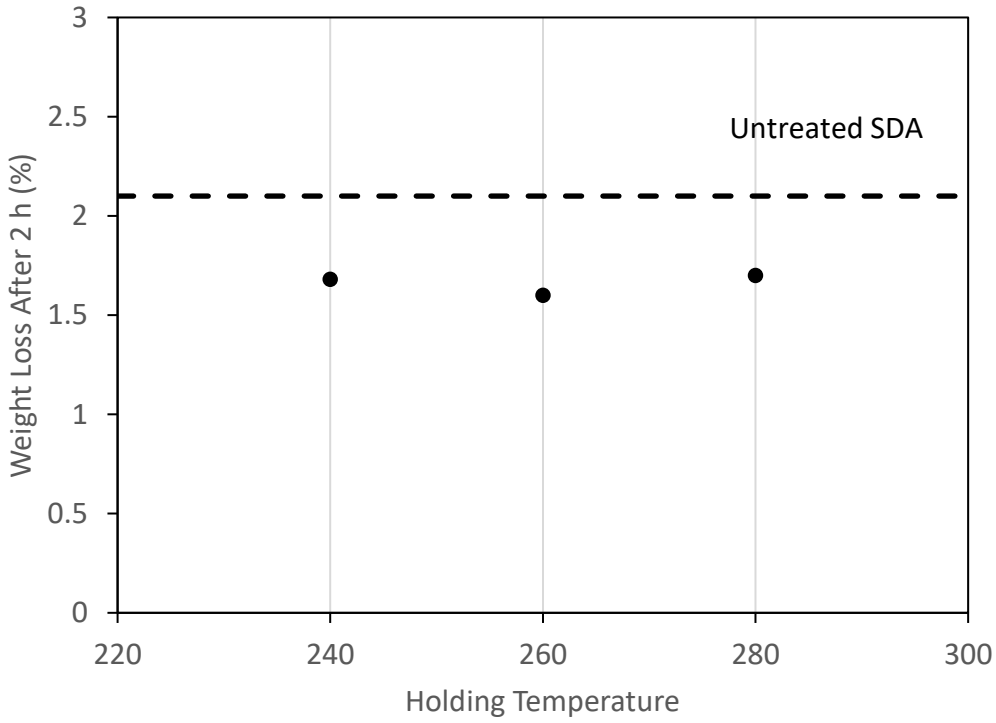

Figure 4.6: TGA weight loss after 2 h as a function of holding temperature

The first observation is that the weight loss of SDA after 2 hours as measured from TGA (~2%) is far more than that deduced from the yield for the heat treatment at 260 °C (~0.5%), even though during heat treatment there is a slow ramp-up period, and the entire treatment lasts for about 5 hours. This could be explained with the escape of volatiles, which would take longer to bubble out in a thicker sample like the crucible used in heat treatments. The positive heat flow in all the samples is evidence that exothermic reactions are occurring. Although this could be explained by physical ordering such as the formation of liquid mesophase, this is unlikely as it has been shown in similar asphaltenes to disappear at 97 °C [37]. Under an inert environment, a more sensible explanation is the presence of polymerization reactions or especially free radical termination reactions, since no bonds are required to break. Exothermicity decreases with increasing heat treatment temperature but SDA-240 and SDA-260 are more exothermic than SDA. This pattern could be due to two competing mechanisms:

1. a shift in the thermal equilibrium to favour more free radical generation reactions than termination reactions at higher temperatures, with excess generated free radicals not completely consumed upon cooling. A higher free radical concentration is therefore available for reaction at the spinning temperature and results in larger specific heat flows.
2. a decreased rate of volatiles generation (an endothermic process) at spinning temperatures after heat treatment. Higher treatment temperatures would be more efficient at removing volatile content and therefore result in lower specific heat flows at the spinning temperature.

Both explanations are supported by NMR. From NMR spectra, the aliphatic to aromatic ratio (Ali:Aro) for both protons and carbon can be quantified. Collection and analysis of ^{1}H and ^{13}C NMR spectra to obtain aromatic and aliphatic content was conducted by the NMR Lab at the University of Alberta. An example of how the analysis is conducted is demonstrated in Appendix C. The Ali:Aro ratios of treated to untreated asphaltenes are compared in Figure 4.7. All the treated asphaltenes were found to have a higher Ali:Aro in both ^{1}H and ^{13}C spectra. ^{13}C Ali:Aro decreased with treatment temperature while no correlation between ^{1}H Ali:Aro and treatment temperature could be established. The large variation between ^{1}H Ali:Aro with treatment temperature is not likely due to instrument error, as repeated measurement yielded similar

values. The increase in ^{1}H and ^{13}C Ali:Aro in the treated compared to the untreated asphaltenes is consistent with polymerization or cross-linking reactions, where substitution reactions would contribute to the increase of ^{1}H Ali:Aro while addition contributes to an increase in ^{13}C Ali:Aro. Meanwhile, the evolution of volatiles could explain the steady decrease of ^{13}C Ali:Aro with increasing treatment temperature, since these volatiles tend to be light hydrocarbons.

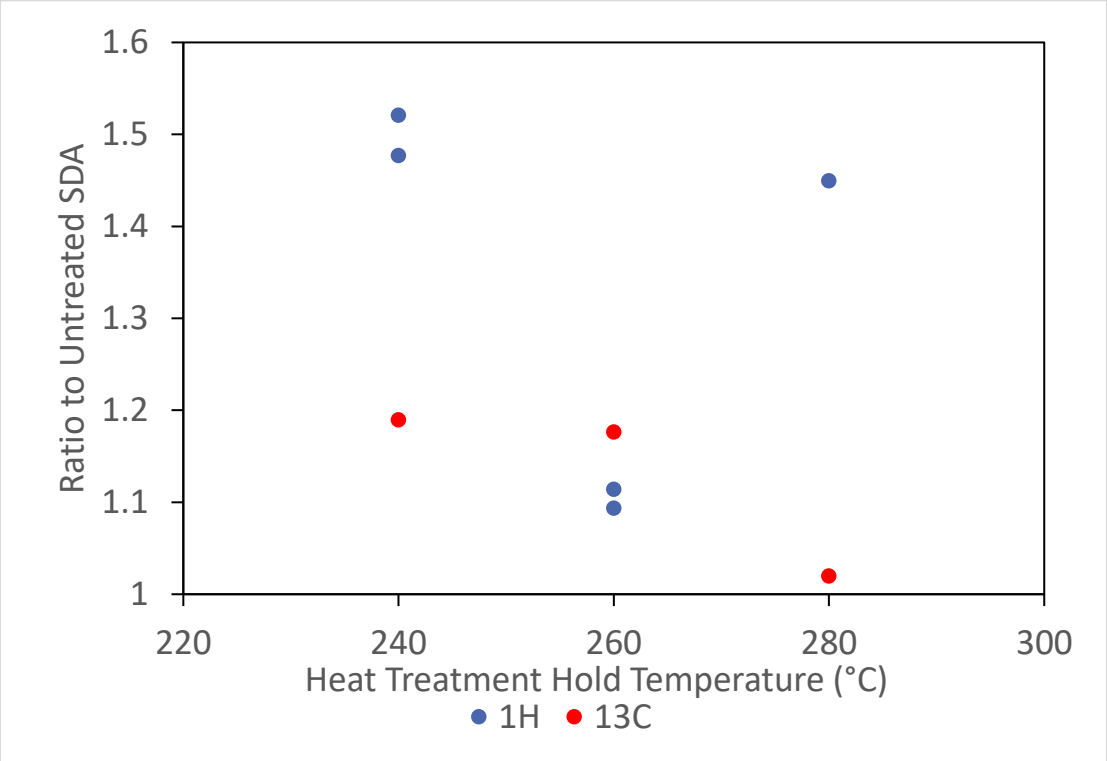

Figure 4.7: Ali:Aro ratios of SDA-x to SDA

Composition may also serve as a clue to the effect of heat treatment on asphaltenes structure and chemistry. Figure 4.8 shows the H/C, S/C, N/C, and O/C ratios of SDA-240 and SDA-280 with respect to that of untreated asphaltenes. The error bars denote the 95% confidence interval[4].

[4] determined by averaging measurements of green fibre fractions, which were found to have no significant dependence of CHNS with time

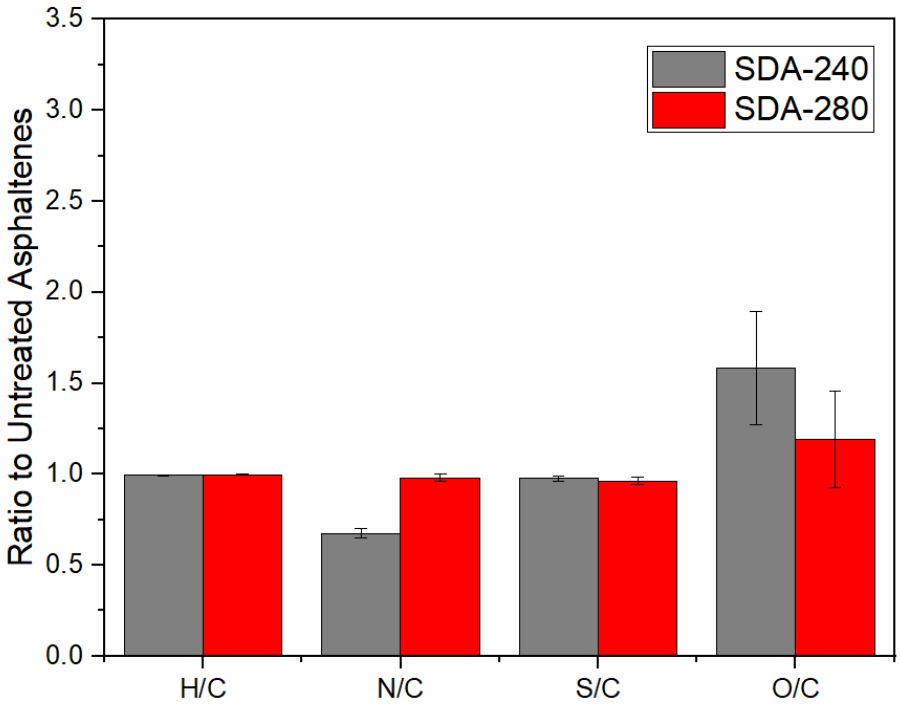

Figure 4.8: Ratios of H/C, N/C, S/C, and O/C of heat-treated SDA to untreated SDA

Even though the escape of light hydrocarbons would, in theory, lead to less hydrogens to carbons in the sample, the volatiles escaped during heat treatment amounts to a negligible mass fraction and so therefore the atomic composition remains virtually unaffected. However, both SDA-240 and SDA-280 had a lower N/C and a higher O/C. A sensible explanation is that even though the heat treatments were run under argon, there was likely residual oxygen in the furnace which reacted with sensitive nitrogen groups to form more volatile nitrogen compounds. An alternative explanation would be that the decrease of nitrogen and increase of oxygen content during heat treatment are independent events that happen to coincide. In that case, the asphaltenes reacted with residual oxygen in the furnace, but the volatilization of nitrogen compounds could have occurred even in the complete absence of oxygen.

4.5 Effect of Delayed spinning on Diameter Distribution Evolution

The relative change in weight w with time t, $\frac{1}{w}\frac{dw}{dt} = \frac{d\ln w}{dt}$, gives a sense of the "reaction rate" responsible for weight loss in the asphaltenes samples, which is shown as a function of time in Figure 4.9 from TGA data. The values of $\frac{d\ln w}{dt}$ are obtained by the Savitzy-Golay method [38] with a 2nd-order polynomial using 300 data points. The first 12 minutes corresponds to the ramp-up period and the peak $\frac{d\ln w}{dt}$ appears shortly after. The maximum $\frac{d\ln w}{dt}$ for the heat-treated samples are about 0.025 h^{-1}, which is the same rate is achieved 6 minutes later in SDA. Since heat treatment for two hours effectively only advances the reaction progress by 6 minutes upon reheating, then cooling must partially reset the volatility of asphaltenes. It is proposed that this phenomenon is due to the dissolution of gases at lower temperatures. It has been shown in literature that gases like CH_4, CO_2, and N_2 have a higher solubility in bitumen at lower temperatures [39] and it is expected that asphaltenes would behave similarly. While nitrogen is present during melt spinning, argon is used as the environment for heat treatments and the TGA/DSC experiments. Therefore, N_2 dissolution could not explain the resetting of volatility observed in the TGA experiments. The dissolution of gases could be better associated with volatile hydrocarbons such as methane and ethane which could be products of cracking, or carbon oxides due to autoxidation.

Therefore, the next idea was to in lieu of heat treatment, delay the beginning of melt spinning instead. The delay was defined beginning from when the probe temperature of the asphaltenes reached the spinning temperature (260 °C). The pressure was only increased to 400 kPa after a specified time has passed. The uptake velocity was set to 6.28 m/s (600 RPM), identical to that used for the melt spinning of SDA without delay and heat-treated feedstocks, and 5-minute green fibre fractions were collected. The median diameter evolutions of various delay times are shown in Figure 4.10. Summary statistics for delayed spinning batches are listed in Table 4.2.

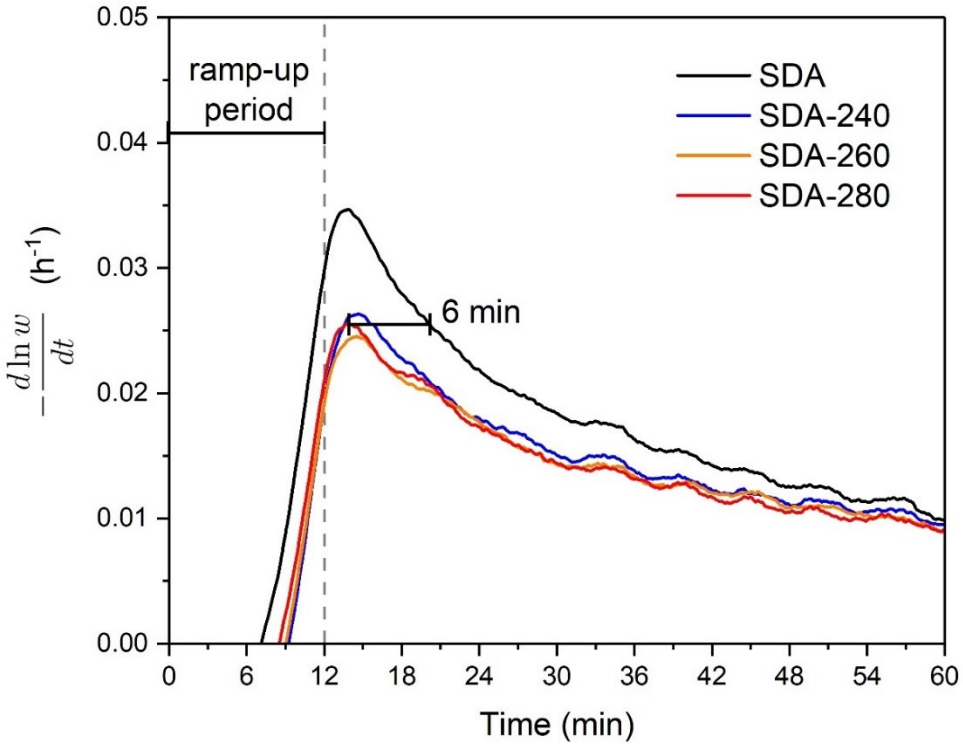

Figure 4.9: Plot of relative rate of weight change as a function of time from the first hour of TGA of treated and untreated SDA.

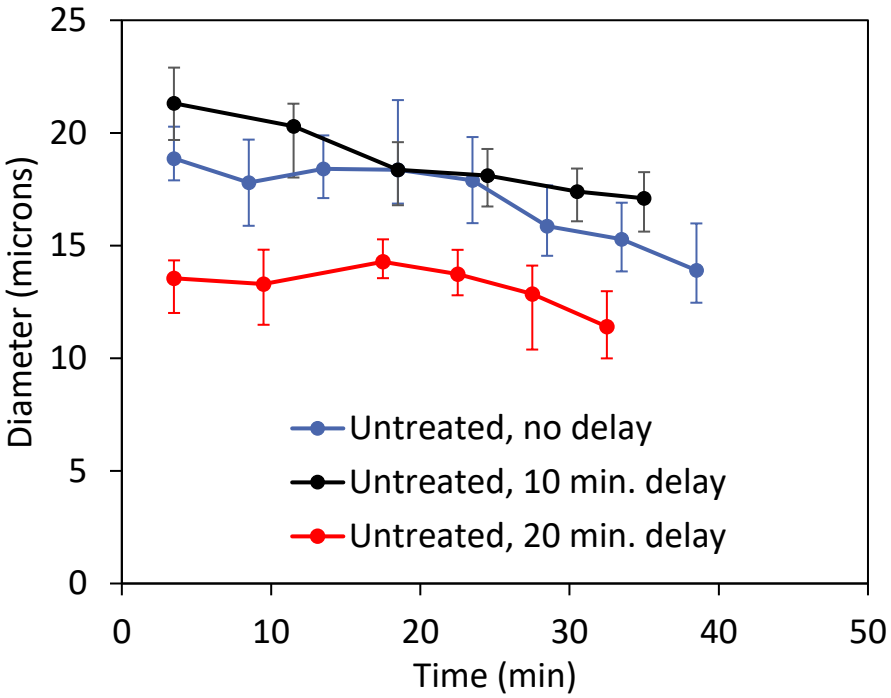

Figure 4.10: Median diameter evolution of delayed spinning fractions. Error bars denote quartiles.

Table 4.2: Median diameter evolution characteristics of delayed spinning fractions

Precursor, Delay	Relative Thinning Rate	Average Median Diameter	Fluctuation
SDA, 0 min	38%/h	18.8 µm	24.9%
SDA, 10 min	40%/h	17.0 µm	20.6%
SDA, 20 min	23%/h	13.2 µm	20.9%

Evidently, delaying the spinning by minutes was similarly effective to heat treating for hours in reducing the diameter of the fibre. This is evidence of reversibility of asphaltenes reactions during melt spinning. However, heat-treated feedstocks were able to spin for longer times with a similar fibre diameter. Yet, a longer spinning time does not necessarily entail better spinnability: the diameter fluctuation of green fibres spun with a delay was generally lower than those using a heat-treated feedstock. A lower fluctuation is explained by a lower perturbation growth rate ω. Plausible explanations for the longer spinning durations of heat-treated feedstocks compared to delayed spinning are:

1. discontinuous extrusion when spinning heat-treated feedstocks where the spinneret is partially or completely blocked.
2. heat-treated asphaltenes continue to be spinnable at a lower thread diameter. As the median diameter decreases with time, these asphaltenes can be spun for a longer duration.

These two interpretations lead to conflicting judgments about whether heat treatment is more effective at improving spinnability than delaying the beginning of spinning. The latter argument must be true since lower diameters are collectable toward the end of spinning. However, the former argument cannot be excluded. In a set of rheology experiments, it was shown that spinneret blockages are a significant phenomenon during melt spinning.

4.6 Capillary Rheometry of Heat-Treated and Untreated Asphaltenes

Differences in DDE have been observed between melt spinning of treated and untreated asphaltenes as well as with or without a delayed start. To understand these differences, capillary rheometry was carried out to examine changes in viscosity with time, since viscosity is regarded

as the fluid property that is associated with the diameter of the produced green fibre during continuous drawing and extrusion. In these capillary rheometry experiments, a piston pushes a sample through a die at a constant velocity according to a given strain rate. The rheometer measures the pressing pressure required to sustain the piston's displacement rate. The pressing pressure is recorded as a function of time. Shown in Figure 4.11, it was found that there was no consistent pattern in the evolution of viscosity. Note that pressure is analogous to viscosity. As shown in Section 2.4.1, in laminar flow the two are linearly dependent, however accurate conversion to viscosity requires Bagley corrections and additional experiments which are not included in this work.

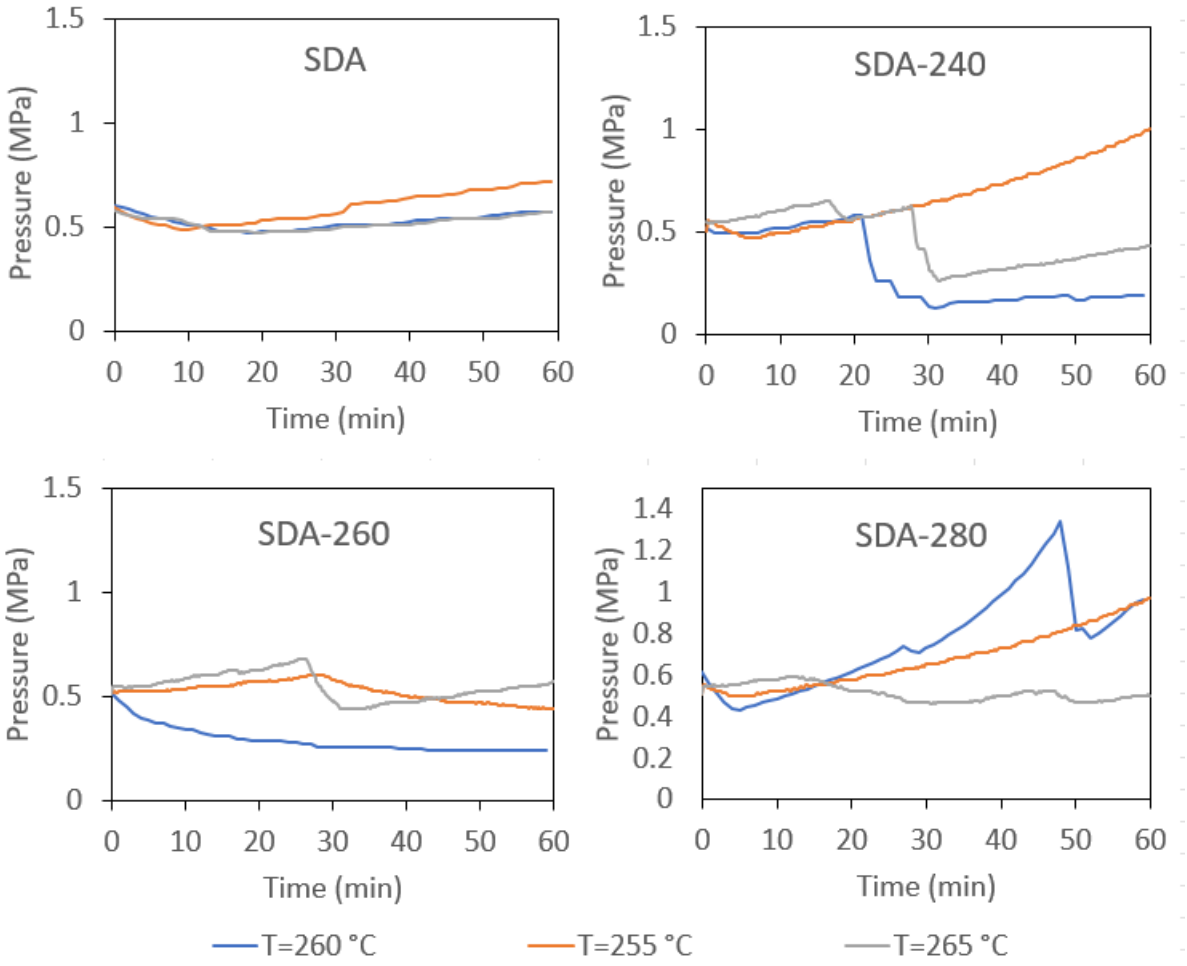

Figure 4.11: Evolution of pressing pressure in capillary rheometry for SDA and SDA-x

The evolution of pressure shown above can be separated into three phenomena, illustrated in Figure 4.12:

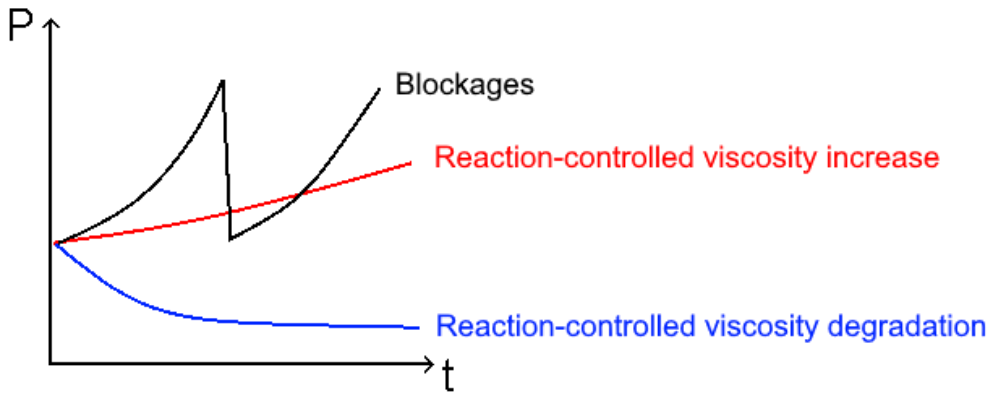

Figure 4.12: Typical pressing pressure evolution phenomena

The existence of gradual blockages also entails that the feed is compressible. The consequence of this would be a significant die swell due to decompression at the die exit. It was observed that the extrudate often preferred to form a glob rather than exit as a cylindrical thread. This would also contribute to a growing pressure as the glob solidifies either due to cooling or oxidation in open air. Upon removing the glob, a drop in pressure is often observed. Other times, there is no flow at all, and the pressure gradually rises. Poking the die with a needle sometimes caused a large amount of material to flow out thereby lowering the pressure, but this was not necessarily replicable. Additionally, flow can sometimes be restored without intervention. The presence of blockages reinforces that it is not meaningful to convert pressure measurements to viscosity, since in discontinuous extrusion the shear rate at the die exit may not correspond to the speed of the piston.

One of the unique runs is with SDA-260 at 260 °C. In this case, an inverse exponential trend is observed, which is consistent with degradation behaviour of other polymers. It could be argued that this trend is also observed in the beginning of other runs, such as those of SDA, but are later replaced by a more dominant increasing trend. The decreasing pressure, and therefore viscosity in continuous extrusion, is inconsistent with the decreasing median diameter of SDA-260 green fibre fractions. This is further confirmation that the physics of discontinuous extrusion

significantly contribute to the spinnability of asphaltenes and the diameter variation in the resulting green fibres.

There are also instances of fluctuating pressures. This is attributed to either melt fracture or wall slip-and-stick phenomena. Nonetheless, the presence of fluctuating pressure imply that the observed fluctuation of green fibre diameter can at least be partially attributed to the extrusion process, although this does not exclude the contribution of fluid thread instability in the drawing process.

Through rheometry, it was shown that the diameter variation of green fibres during melt spinning is significantly contributed by the extrusion process. A complete solution to mitigate diameter variation in melt-spun green fibres must address both the material properties of the feedstock as well as the design of the spinneret.

4.7 Pycnometry of Green Fibre Fractions

Besides viscosity, density can also influence the melt spinning behaviour, for example in discontinuous extrusion where the gravity term ρg assists in overcoming the surface tension of a droplet to form a thread, or in the shaping of the thread diameter profile $D(z)$. However, density is more importantly an indicator of molecular weight which would increase if cross-linking reactions were indeed occurring in the molten asphaltenes. There may also be a change in density throughout spinning if there was phase separation between lighter and heavier components of the feedstock.

Since it is not trivial to measure the density of an asphaltenes melt, the density of the green fibre is taken as an indicator of the density of the melt. Both propylene glycol (bulk) and helium (true) densities of SDA and SDA-280 fractions are measured. The true density reflects the actual density of the asphaltenes, while the bulk density also includes the effect of porosity. The two densities of SDA and SDA-280 are compared in Figure 4.13. The vertical error bars correspond to 95% confidence intervals while the horizontal error bars show the time since the beginning of spinning from which the fraction is taken. From these results, there is no significant trend in the true density with time, except for the beginning and end fractions where the true density tends to be higher for both the treated and untreated green fibres. Meanwhile, the bulk density seems to

increase and then decrease with time for SDA, but this trend was not seen in SDA-280. This could be due to the contribution of scatter which is higher in SDA-280. As shown by the 95% confidence intervals, the scatter cannot be fully explained by measurement error, and must also be due to the material itself. Therefore, heat treatment enhances inhomogeneity in the asphaltenes feedstock. Furthermore, this conclusion confirms that the variation in diameter of green fibres from heat-treated asphaltenes is not solely due to fluid thread instability.

It is also evident that the first and last fractions have a higher true density than the rest of the fractions. The first fraction could have a higher density due to heavier components sinking to the bottom while the precursor is heated. The denser last fraction suggests skin formation. The last fraction is also in constant contact with the nitrogen pressing gas. While the nitrogen is expected to be chemically inert, it is still possible for the nitrogen to dissolve into a skin layer of the asphaltenes melt. However, the dissolution of nitrogen at higher temperatures would be accompanied with the formation of bubbles as the melt cools and solidifies. The presence of bubbles would then be reflected in higher porosities, i.e. relative difference between true and bulk densities. Since there is no consistent evidence of higher porosity in the last fraction compared to the rest of the fractions, it cannot be concluded that nitrogen dissolves into the skin layer to any significant extent. Note that this conclusion does not disprove the possibility that nitrogen enhances skin formation or the density of the skin.

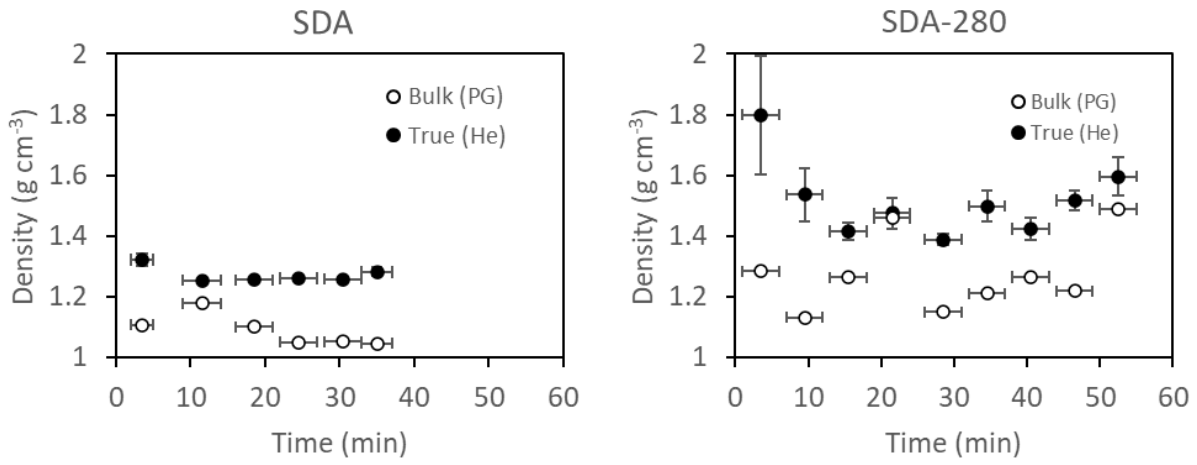

Figure 4.13: Pycnometry of SDA and SDA-280 fractions

When both bulk and true densities are available, porosity (open) can be calculated from their relative difference, shown in Equation 4.6. A higher porosity is an indicator that the precursor generates more volatile matter.

Equation 4.6

$$\text{Porosity} = 1 - \frac{\rho_{\text{bulk}}}{\rho_{\text{true}}}$$

Average true densities and porosities of green fibre fractions are shown in Table 4.3. Due to the large scatter of porosities throughout the fractions, the difference in porosities of SDA and SDA-280 could not be meaningfully differentiated. However, the average true density of SDA-280 is noticeably higher than SDA, while the true density of SDA-260 is lower than SDA. Delaying the spinning of SDA by 20 minutes leads to an intermediate density between SDA with no delay and SDA-260.

Table 4.3: Average densities and porosities of green fibre fractions

Feedstock	Treatment Conditions*	Delay	Average True Density	Average Bulk Density	Average Porosity
SDA	N/A	None	1.27 g/cm^3	1.09 g/cm^3	14.4%
SDA-260	260 ˚C for 2 h	None	1.05 g/cm^3	No data	No data
SDA-280	280 °C for 2 h	None	1.52 g/cm^3	1.27 g/cm^3	15.6%
SDA	N/A	20 min	1.13 g/cm^3	No data	No data

*After 1.5 ˚C/min ramp-up from room temperature.

Note that true density here corresponds to that measured by helium pycnometry, so the assumption that there is negligible closed porosity must be entertained. The true density corresponds to the density if the material had no porosity at all and serves as a clue to the chemistry and microstructure of the material. In the case of green fibres, a higher density is attributed to a higher aromatic to aliphatic content or increased cross-linking, corroborating with previous TGA/DSC and NMR results.

4.8 CHNS-O Analysis of Green Fibre Fractions

To narrow down the nature of inhomogeneity in heat-treated fractions, carbon, hydrogen, nitrogen, sulphur, and oxygen compositions were determined. Figure 4.14 shows the evolution

of H/C, N/C, S/C, and O/C ratios (HNSO/C) for SDA, SDA-240, SDA-280, and SDA-del20 (20 min delayed spinning of untreated SDA). Some fractions were measured twice to demonstrate data reproducibility.

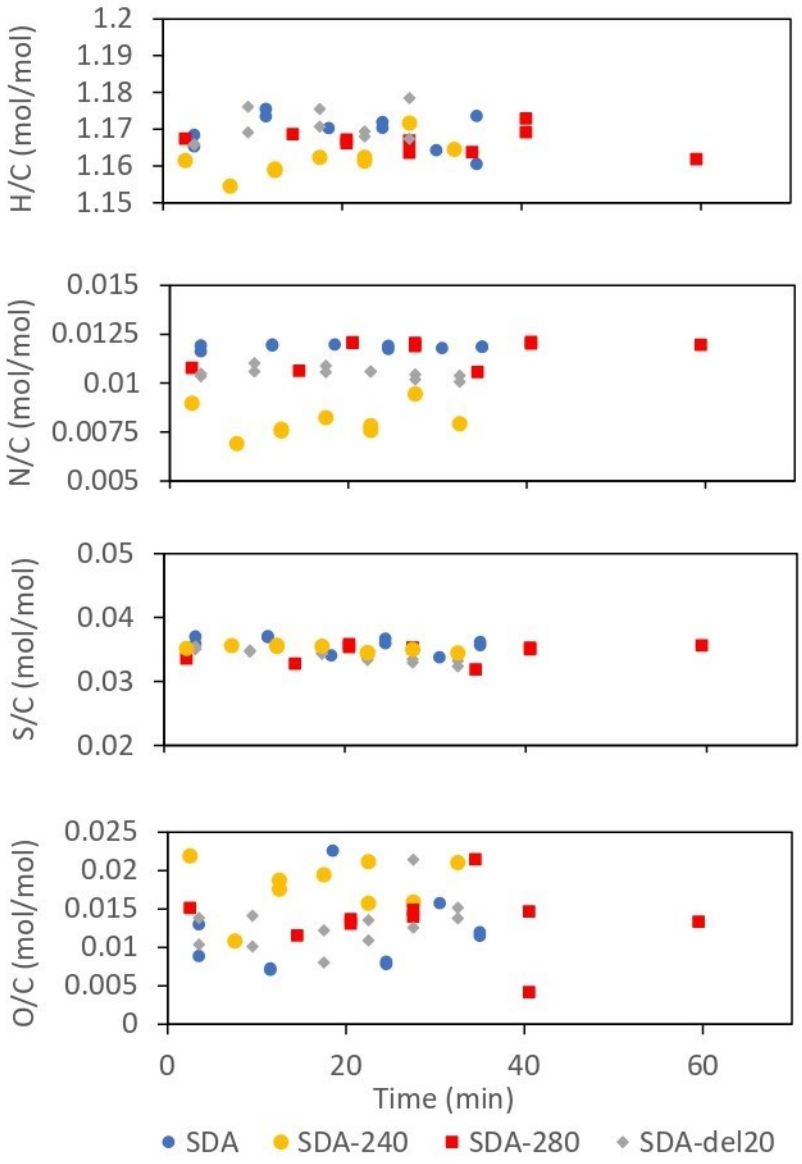

Figure 4.14: CHNS(O) of green fibre fractions of SDA, SDA-240, SDA-280, and SDA-del20

Evidently, there is no significant trend of CHNS-O compositions with time. However, the average compositions of the fractions for each of the spinning variations have differences. These differences were discussed in Section 4.4 where the higher O/C of heat-treated precursors

compared to untreated SDA was attributed to residual oxygen in the heat treatment furnace. The lower N/C of heat-treated precursors compared to untreated SDA was attributed to volatilization of nitrogen functional groups in the asphaltenes. It was suggested but not proven that the residual oxygen reacted with these nitrogen groups leading to its volatilization. The limitation of these arguments is that the average compositions were taken from fractions of green fibres which had undergone the spinning process in addition to heat treatments if applicable. Here, SDA-del20 was not subjected to any heat treatments, yet also exhibits a notably lower average N/C and higher O/C compared to SDA. This is better represented in Figure 4.15, which shows average HNSO/C of SDA-240, SDA-280, and SDA-del20. The vertical error bars denote the 95% confidence interval of the average.

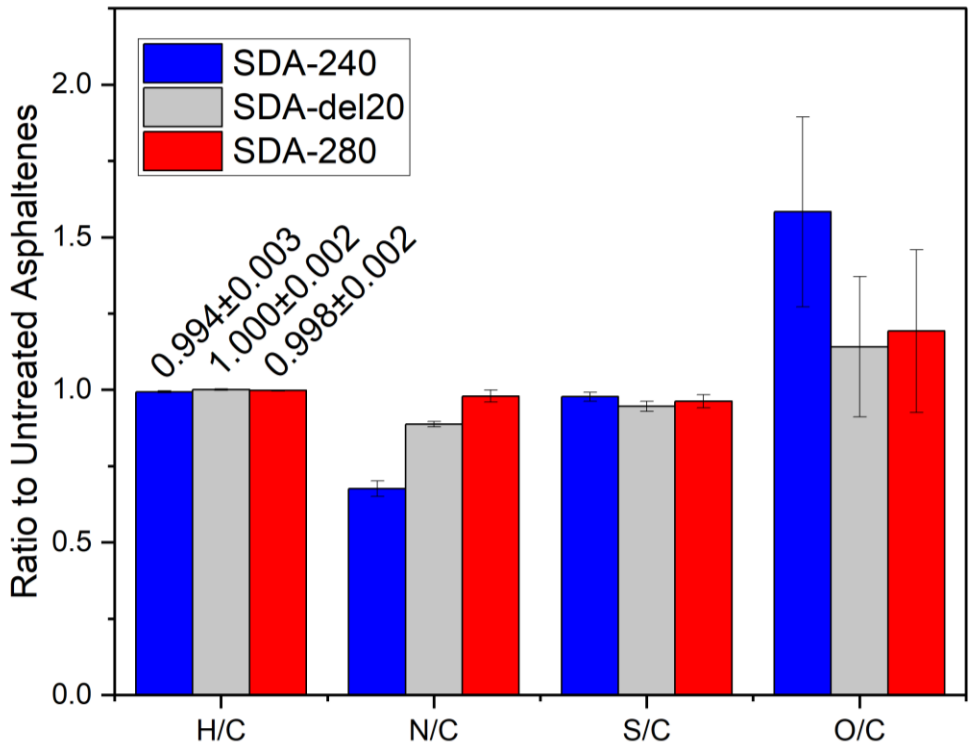

Figure 4.15: Average HNSO/C ratios of SDA-240, SDA-280, and SDA-del20 fractions to untreated SDA fractions with no delayed spinning.

The average HNSO/C suggests that there is no correlation between N/C and O/C ratios. In that case, reaction of residual oxygen with nitrogen functional groups is not a major contributor of N/C reduction. The reduction of N/C also can occur in a nitrogen-only environment, as suggested by the N/C of SDA-del20 which is lower than SDA, and so is not due to the nitrogen-free argon

environment during heat treatment. N/C reduction is therefore attributed to one or more of the following reasons:

- Dissolved nitrogen, possibly from high-pressure and low-temperature processes during solvent de-asphalting, is liberated at spinning conditions.
- Nitrogen incorporated into the molecular structure of the asphaltenes are converted to volatile compounds at spinning temperatures and are liberated irreversibly.

These reasons are not sufficient to explain the trends in N/C reduction. Nitrogen, as a gas, is expected to have a higher solubility in liquids with decreasing temperature or increasing pressure, as it has been shown to be the case for bitumen [39]. It is unlikely that nitrogen would behave differently in asphaltenes. Therefore, the former reason could not alone explain N/C reduction. Meanwhile, the volatilization of nitrogen from the asphaltenes molecular structure would likely be kinetically faster with increasing temperature, but N/C reduction is lower with higher heat treatment temperature. Therefore, the latter reason also cannot explain the trends in N/C reduction.

In addition to the trends in N/C and O/C, there is a positive correlation between O/C and S/C. S/C average ratios of heat-treated or SDA-del20 are slightly lower than that of SDA. Although the differences in H/C are slight, they are statistically significant, and are in negative correlations with O/C and S/C.

4.9 Tetrahydrofuran Treatments

It was thought that if free radical reactions were at least partially responsible for DDE, then a low-temperature chemical treatment aimed at removing free radicals from the precursor could reduce green fibre diameter variation. Indeed, it has been reported that up to 68% of the free radical content could be removed by boiling asphaltenes in tetrahydrofuran (THF) for 24 hours [40]. Here, the asphaltenes were instead boiled for 12 hours. Figure 4.16 shows the FTIR spectra for SDA and THF-treated variants, and the peaks are identified in Table 4.4. A peak between 1650-1800 cm^{-1} and a broad peak between 1000-1300 cm^{-1}, associated with oxidation, were observed in THF-treated asphaltenes (SDA-THF), but upon further heat treatment at 260 °C (SDA-THF-260), the peaks disappeared and there was no significant difference between SDA and SDA-THF-260.

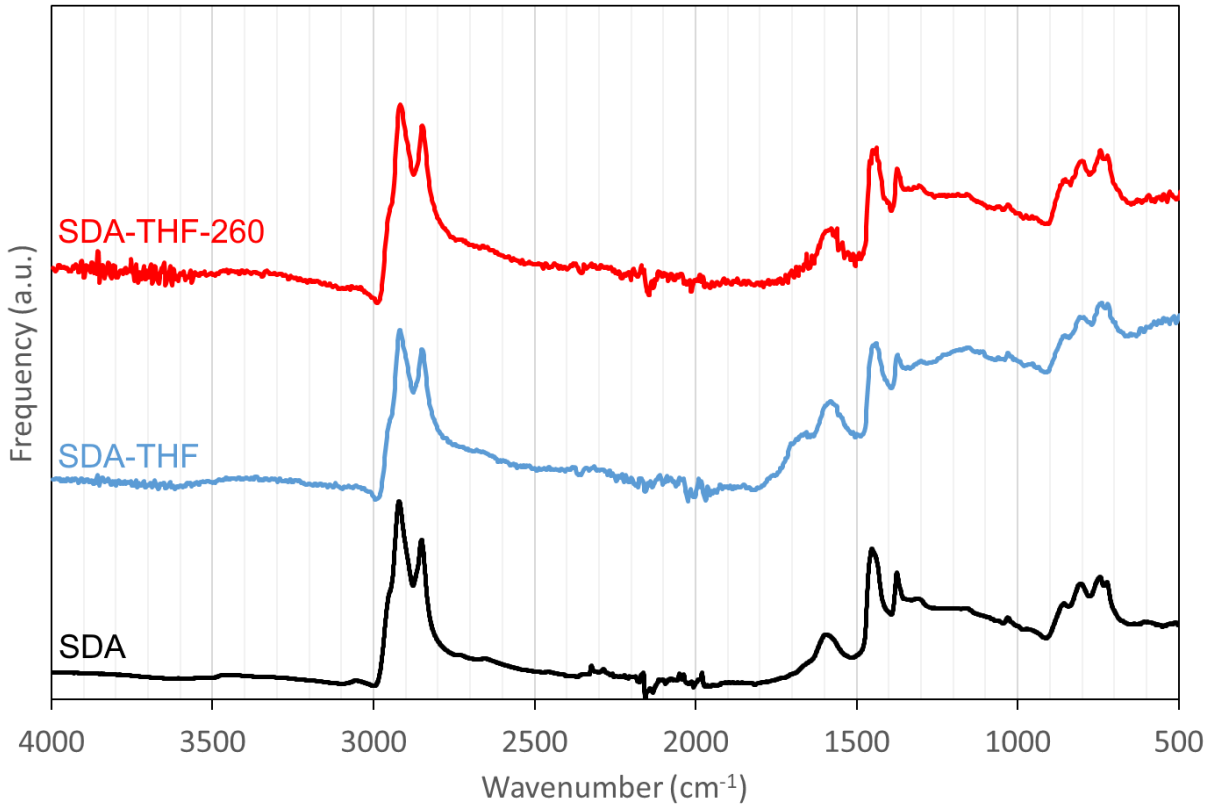

Figure 4.16: FTIR spectra of THF-treated asphaltenes

Table 4.4: Peak Identification for FTIR of SDA and THF-treated variants

Wavenumber (cm^{-1})	Description
2920, 2850	Alkane C-H stretching
1650-1800 (SDA-THF)	Various C=O stretching
1600	Alkene C=C stretching or N-H bending
1450	Alkane C-H bending
1350-1380	Sulfonate and sulfone S=O stretching
1250-1350	Aromatic amine C-N stretching or aromatic ester C-O stretching
1000-1300 (SDA-THF)	Various C-O stretching
1030	Sulfoxide S=O stretching
855, 810, 745, 720	Aromatic C-H bending

The resulting precursor, SDA-THF-260, was not spinnable at all at 260 °C. This could either mean that the softening temperature has significantly changed or that SDA-THF-260 is not spinnable at all. No further investigation on THF treatments on SDA were conducted.

4.10 Spinnability of Heat-Treated Asphaltenes

It was found that while SDA-260 and SDA-280 could be melt-spun unsupervised with occasional thread breakage, successful spinning of SDA-240 was occasional and not replicable. Table 4.5 summarizes the number of successful melt-spinning attempts for each precursor over the course of this work. The precursor SDA-280-24 was produced in a similar treatment procedure to SDA-280, except with a 24-h hold time instead of 2 h. A spinning is declared successful only if green fibres could be collected at the uptake drum without supervision, except upon resuming a pause to extract fibre fractions.

Table 4.5: Record of successful spinning attempts of treated and untreated asphaltenes

Precursor	Treatment Conditions*	No. of Spinning Runs	No. of Successful Spinning Runs
SDA	N/A	4	3
SDA-240	240 °C for 2 h	3	1
SDA-260	260 °C for 2 h	2	2
SDA-280	280 °C for 2 h	3	2
SDA-280-24	280 °C for 24 h	1	0

*Held at these temperatures after a ramp-up of 1.5 ˚C/min

While there are not enough spinning runs to make any statistically significant claims about the spinnability of these precursors, the data presented could serve as a starting point for a larger-scale investigation on spinnability.

4.11 Tensile Strengths of Carbonized Fibre Fractions

The hypothesis central to this work is that diameter variation in the green fibres affects the mechanical performance of the carbonized fibre as the effectiveness of processes after melt spinning, such as oxidative stabilization, theoretically depend on the fibre diameter. To verify this, tensile tests were carried out on carbonized fibres from SDA fractions.

SDA fibre fractions F2 (9-14 min), F3 (16-21 min), F5 (28-33 min), and F6 (33-37 min) were oxidized and carbonized for tensile tests each using the same procedure outlined in Section 3.11. The oxidation and carbonization procedures were adapted from previous literature. The other fractions, F1 (2-5 min) and F4 (22-27 min), did not have sufficient mass to undergo the oxidization and carbonization procedure. F6 was disintegrated upon carbonization and therefore tensile

specimens for F6 could not be prepared. The disintegration of F6 supports the theory discussed in Section 4.1 that some fractions would not be treated properly given the evolution of green fibre diameters with time. In this case, F6 has a lower average diameter than other fractions, so it is likely that F6 disintegrated due to over-oxidation. It is also probable that the oxidation and carbonization procedures were not optimal since the precursor and operating conditions of this study are not identical to that in reference literature. However, to optimize all the oxidation and carbonization variables, i.e. temperature and time of each heating step and acid and ethanol concentrations for oxidation, would be a substantial amount of work that is outside the scope of this study. Optimizing the oxidation and carbonization could significantly improve the tensile properties of the resulting carbon fibres, but even if these processes were not optimized, evidence that some fractions are not properly treated or differences in tensile properties across fractions entail that the oxidation and carbonization processes would not be optimized for every fraction even if they were optimized for the entire spinning batch.

At least 20 specimens were tested for each preparable fraction. The diameters and measured strengths of the single fibres can be found in Appendix D. Average tensile strengths of the tested fractions are plotted with respect to median diameter in Figure 4.17. The vertical error bars denote the 95% confidence interval. The average tensile strengths appear to be lower at higher median diameter, however the sample sizes are still too small to claim so with statistical significance.

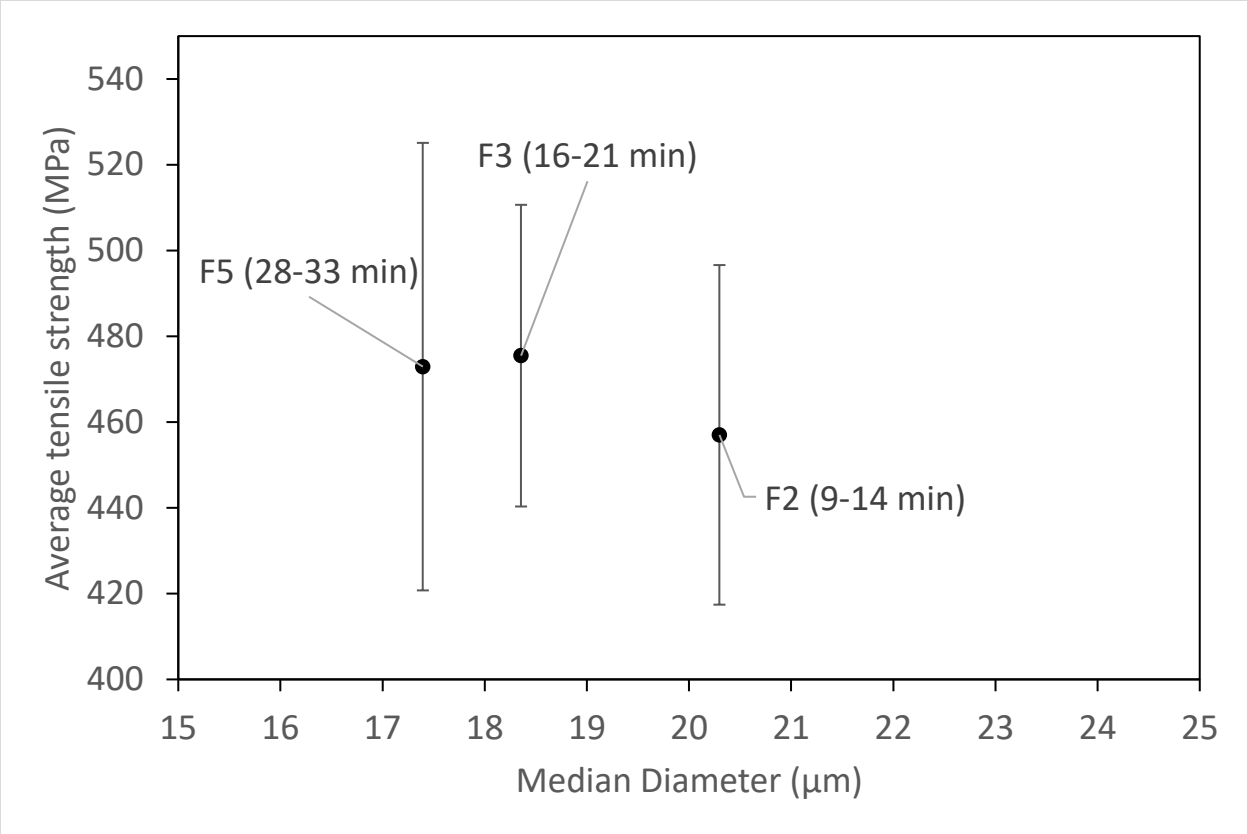

Figure 4.17: Average tensile strength as a function of median diameter of SDA carbonized fibre fractions

Suppose that the average tensile stress indeed does decrease with increasing median diameter. While this phenomenon could be explained by the fact that brittle materials' strengths decrease with increasing volume due to the weakest link theory and Weibull statistics, it does not exclude the contribution of material dependence. I.e., two sample groups with the same median diameters could still have different average tensile strengths. It is therefore necessary to separate the material and volume dependence of tensile strengths. This is done by Weibull analysis, which entails the fitting of Weibull parameters to the tensile strengths and fibre volumes. Refer to Section 2.7 for details on how Weibull analysis was carried out. Figure 4.18 shows Weibull plots for F2, F3, and F5, while Figure 4.19 shows the estimated parameters and their 50% (dashed line) and 95% (solid line) confidence contours. The reference volume used was equivalent to a 5 mm × 20 µm diameter fibre.

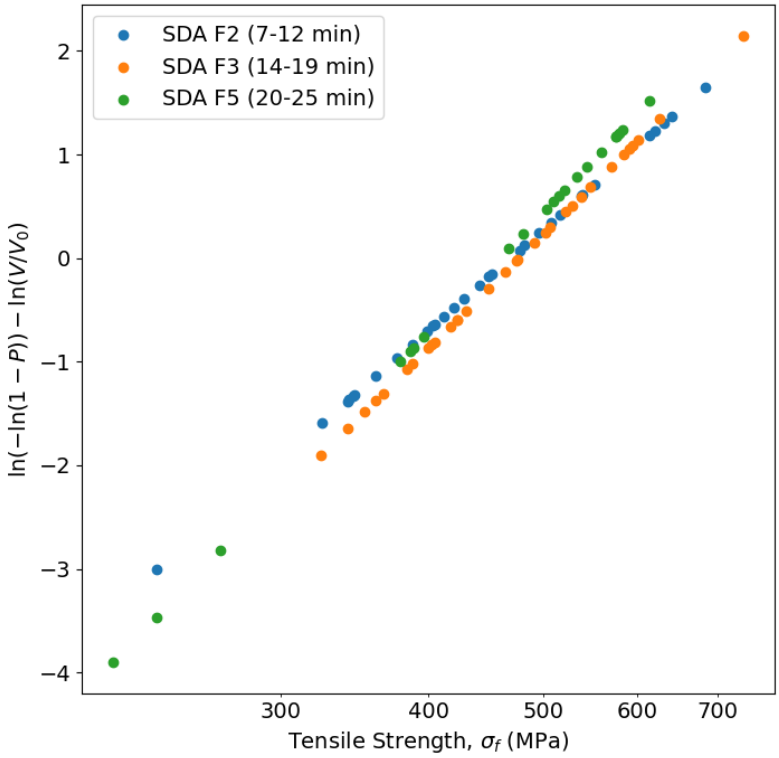

Figure 4.18: Weibull plots for SDA carbonized fibre fractions

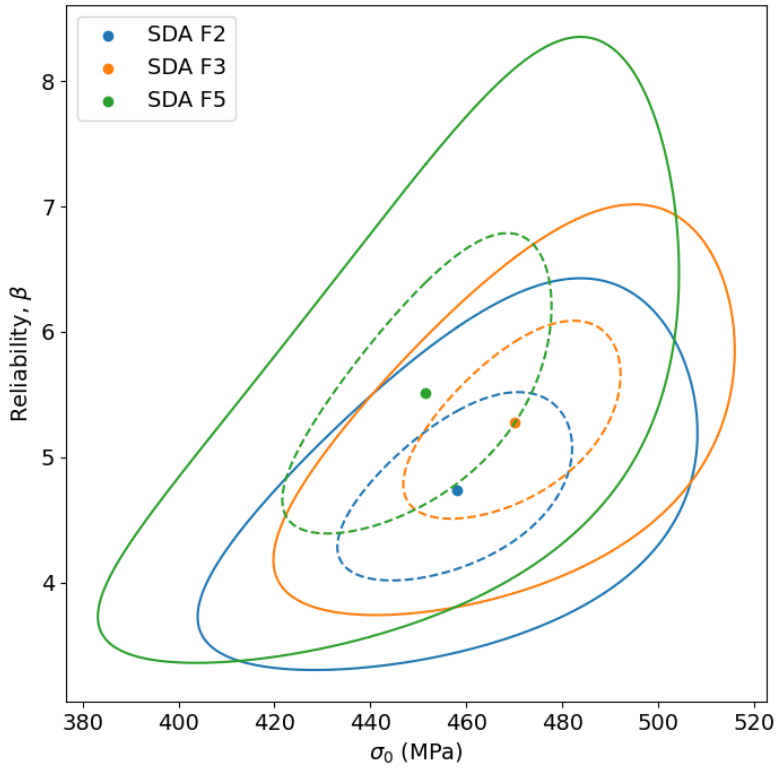

Figure 4.19: Weibull parameter estimates and confidence contours of carbonized fibre fractions

Without rigorous statistical analysis, the severe overlap between the confidence contours shows that no significant trends in β or σ_0 with spinning time can be claimed. This agrees with other literature where a precise estimate of β is claimed to require hundreds of tensile specimens [41]. A Monte Carlo simulation (Figure 4.20) shows the average size of the bounding box dimensions Δ_β (solid) and Δ_{σ_0} (dashed) with sample size over 30 randomly generated datasets.

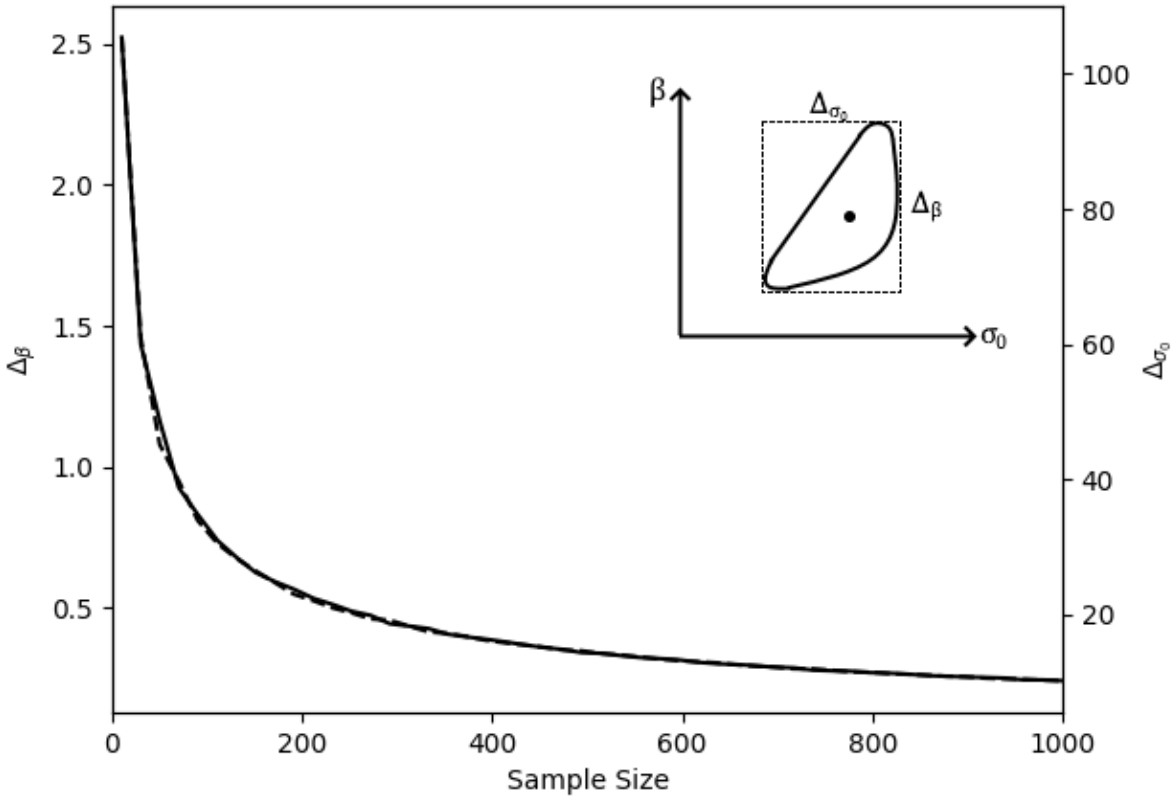

Figure 4.20: Bounding box dimensions of the 95% confidence contour as a function of sample size for β=4 and σ_0=500 MPa, averaged over 30 Monte Carlo simulations

A reasonable goal to achieve is a Δ_β of 0.5, which would require about 200 samples. The corresponding Δ_{σ_0}, about 20 MPa is also reasonable. Creating and testing this sample size, although possible, may not be viable when many groups of tests must be done.

Although the investigation on tensile properties across fractions of untreated SDA carbon fibres remains inconclusive due to low sample size, the question remains whether there would be a

significant effect of treatment or spinning delay on tensile properties. The low sample sizes practically achievable from the tensile testing procedure used in this study would continue to hinder this investigation since the achievable resolution of β and σ_0 are far too low to detect even moderate improvements in tensile properties. Yet, even if the ability to resolve changes in β and σ_0 are improved, it is not clear whether the oxidation and carbonization procedures for fibres derived from different spinning variations or precursors should be controlled and kept the same for each or optimized independently. The latter case would conclude whether one spinning has better optimized tensile properties than another but fails to address whether higher tensile properties are a result of lower diameter variation or a result of an improved precursor. In the former case, even if the average diameter is the same across, say, two different treatments but the diameter variance is different, it is still ambiguous whether an improvement in tensile properties is due to diameter variation or treatment. Variations in the precursor or spinning procedure are necessary to alter diameter variation in green fibres, but it is not possible to optimize tensile properties solely as a function of diameter distribution. Therefore, a method to separate the material and geometrical contributions of the green fibres on the optimal tensile properties of the carbon fibres must be determined.

In this study, it was found that heat treatment influenced the average porosity of green fibres (Section 4.3). Without any mechanism for the porosity to collapse during oxidation and carbonization, it is likely to remain in the final product. With an understanding of the pore structure, it may be possible to exclude the effect of porosity on tensile strength. However, other forms of defects exist. For example, particulates (e.g. coke) finer than the filter mesh (75 µm) would be incorporated in the green fibres (<50 µm diameter) and lead to a negative influence on tensile properties of the final carbon fibres. Even if the particulates were filtered out perfectly, it is still possible for coke to form during oxidation or carbonization. Therefore, a full understanding of the microstructural evolution from green fibre to carbon fibre must be understood in order to reveal the effects of treatment or spinning variation on mechanical properties.

5 CONCLUSIONS

Diameter variation in the melt spinning of Alberta solvent-de-asphalted asphaltenes were found to be partly due to a time-dependent diameter thinning, and partly due to time-independent

fluctuation. Both reversible and irreversible reactions are responsible for diameter thinning. The study considers the three fluid properties central to the physics of melt spinning: density, viscosity, and surface tension. Experimental data concluded that there are no significant changes in density with spinning time and viscosity alone cannot explain the thinning process. By process of elimination, a follow-up investigation of surface tension is critical to understanding how to control diameter non-uniformity.

The following variations to the melt spinning process was investigated in addition to spinning untreated solvent-deasphalting asphaltenes (SDA):

- heat treating the feedstock at around spinning temperatures (240, 260, 280 °C) to allow for irreversible reactions to approach equilibrium,
- delaying the beginning of spinning (10 or 20 minutes) to allow for reversible and irreversible reactions to approach equilibrium, and
- simmering SDA in THF for 12 hours and heat treating at the spinning temperature (260 °C) to chemically reduce free radical content. Heat treatment was necessary to remove oxidized components resulting from the boiling in THF.

The THF-treated SDA could not be spun at the same spinning temperature as untreated SDA (260 °C). This could be due to a significant change in softening temperature or alternatively, THF-treated SDA is not spinnable at all. Heat treating the feedstock for 2 hours at around the spinning temperature did not change the spinning temperature of the precursor and continued to be spinnable at 260 °C. However, melt spinning of SDA heat-treated at 280 °C for 24 h was not successful, suggesting that there is a limit to how long the feedstock should be heat-treated. Delaying the beginning of melt spinning by 10 or 20 minutes also did not change the spinning temperature and the melt spinning process was successful. Delaying the beginning of melt spinning is more effective at reducing fluctuation and thinning rate than heat treatment, but the feedstock can be spun longer with heat treatment. The values for relative thinning rate and fluctuation are determined for some spinnable variations and summarized in Table 5.1.

Table 5.1: Summary of diameter distribution evolution characteristics for the melt spinning of SDA and its variations

Name	Heat treatment	Spinning Delay	Relative Thinning Rate	Fluctuation
SDA	N/A	0 min	38%	24.9%
SDA-260	260 °C for 2 h	0 min	42%/h	22.6%
SDA-280	280 °C for 2 h	0 min	30%/h	24.1%
SDA-del10	N/A	10 min	40%	20.6%
SDA-del20	N/A	20 min	23%	20.9%

No significant trends were found in the H/C, N/C, S/C, and O/C ratios with spinning time. However, when comparing composition ratios between SDA and its variations, S/C and O/C are positively correlated, but they are negatively correlated with H/C. N/C does not correlate with any of the other composition ratios. N/C of the green fibres obtained by variations of SDA melt spinning were found to be lower than that of SDA without treatment or delayed spinning. The reduction of N/C occurred even in a nitrogen environment and is more pronounced with lower heat treatment temperatures.

The combination of TGA-DSC and NMR experiments show that heat treatment at temperatures around the spinning temperature (and by extension the spinning process itself) imply two chemical processes: the generation of volatiles and cross-linking/polymerization reactions. Although cracking is not expected to be significant at spinning temperatures, any minute extent of cracking would lead to more double bonds formed, which could participate in addition reactions. Only a small amount of addition reactions would be required to significantly affect the molecular weight, and therefore viscosity of asphaltenes. Cracking can also explain the trend in volatiles generation which increases with heat treatment temperature.

The effect of diameter non-uniformity of green fibres on the final tensile properties of the carbonized fibre remains inconclusive due to insufficient sample size. Tensile properties are not only a function of diameter distribution but also the molecular structure and microstructure evolution throughout the stabilization and carbonization processes. In addition to achieving

larger sample sizes, a better understanding of these evolutions (e.g. pore structure and particulates) is required in order to separate the material and geometrical effects of the tensile properties of carbon fibres prepared from either different precursors or spinning variations.

6 FUTURE WORK

There are three major improvements that this investigation could use to further advance understanding of diameter variation of asphaltenes melt spinning, the role of diameter variation in the tensile strength of carbon fibres, and any implications on spinnability along the way:

- Determination of surface tension in treated and untreated SDA. This can be experimentally difficult because the experiments must be done in an inert atmosphere to avoid oxidizing the surface of the asphaltenes, and the apparatus must be able to handle high temperatures of hundreds of degrees Celsius.
- More tensile tests must be done to increase sample size sufficiently for statistical significance. Since it is anticipated that hundreds of samples must be done, innovation is needed to optimize every part of the tensile testing process.
- Tensile tests for carbonized fractions produced from other variations of SDA melt spinning, such as using a heat-treated precursor or delaying the beginning of spinning should be carried out. However, first, the oxidation and carbonization procedures must be optimized for each variation.
- A method of separating the material and geometrical (diameter distribution) contributions on tensile properties from carbon fibres prepared from different precursors must be determined in order to assess the influence of diameter distribution on tensile properties.

REFERENCES

[1] W. Chen.Canada Patent WO/2021/072559, 2021.

[2] P. Bhatt and A. Goe, "Carbon Fibres: Production, Properties, and Potential Use," *Mat. Sci. Res. India,* vol. 14, no. 1, 2017.

[3] S. Nunna, P. Blanchard, D. Buckmaster, S. Davis and M. Naebe, "Development of a cost model for the production of carbon fibres," *Heliyon,* vol. 5, no. 10, 2019.

[4] M. Huson, "High-performance pitch-based carbon fibers," in *Structure and Properties of High-Performance Fibers*, Woodhead Publishing, 2017, pp. 31-78.

[5] F. W. Zok, "On weakest link theory and Weibull statistics," *J. Am. Ceram. Soc.,* vol. 100, no. 4, pp. 1265-1268, 2017.

[6] S.-J. Park, Carbon Fibers, Singapore: Springer Nature Singapore Pte Ltd., 2018.

[7] P. Zuo, D. Leistenschneider, Y. Kim, D. G. Ivey and W. Chen, "The effect of thermal pretreatment temperature on the diameters and mechanical properties of asphaltene-derived carbon fibers," *J. Mat. Sci.,* vol. 56, pp. 14964-14977, 2021.

[8] E. A. Morris and M. C. Weisenberger, "Solution Spinning of PAN-Based Polymers for Carbon Fiber Precursors," in *Polymer Precursor-Derived Carbon*, vol. 1173, American Chemical Society, 2014, pp. 189-213.

[9] Y. Qin, "3 - A brief description of textile fibers," *Medical Textile Materials,* pp. 23-42, 2016.

[10] J. B. Donnet, O. P. Bahl, R. C. Bansal and T. K. Wang, "Carbon Fibers," in *Encyclopedia of Physical Science and Technology*, 3 ed., R. A. Meyers, Ed., Academic Press, 2003, pp. 431-455.

[11] M. S. A. Rahaman, A. F. Ismail and A. Mustafa, "A review of heat treatment on polyacrylonitrile fiber," *Polymer Degradation and Stability,* vol. 92, no. 8, pp. 1421-1432, 2007.

[12] B. Saha and G. C. Schatz, "Carbonization in Polyacrylonitrile (PAN) Based Carbon Fibers Studied by ReaxFF Molecular Dynamics Simulations," *J. Phys. Chem. B,* vol. 116, no. 15, pp. 4684-4692, 2012.

[13] P. Chen, J. N. Metz, A. S. Mennito, S. Merchant, S. E. Smith, M. Siskin, S. P. Rucker, D. C. Dankworth, J. D. Kushnerick, N. Yao and Y. Zhang, "Petroleum pitch: Exploring a 50-year structure puzzle with real-space molecular imaging," *Carbon,* vol. 161, pp. 456-465, 2020.

[14] I. Mochida, Y. Korai, C. Ku, F. Watanabe and Y. Sakai, "Chemistry of synthesis, structure, preparation and application of aromatic-derived mesophase pitch," *Carbon,* vol. 38, no. 2, pp. 305-328, 2000.

[15] T. Matsumoto, "Mesophase pitch and its carbon fibers," *J. Pure & Appl. Chem.,* vol. 57, no. 11, pp. 1553-1562, 1985.

[16] C. Daulbayev, B. Kaidar, F. Sultanov, B. Bakbolat, G. Smagulova and Z. Mansurov, "The recent progress in pitch derived carbon fibers applications. A Review," *South African Journal of Chemical Engineering,* vol. 38, pp. 9-20, 2021.

[17] D. D. Dunham and M. G. Edie, "Melt-Spinning Pitch-Based Carbon Fibers," *Carbon,* vol. 27, no. 5, pp. 647-655, 1989.

[18] A. Abdelazim, M. Abu El Ela, A. El-Banbi and H. Sayyouh, "Successful approach to mitigate the asphaltenes precipitation problems in ESP oil wells," *J. Pet. Explor. Prod. Technol.,* vol. 12, pp. 725-741, 2022.

[19] S. Elkahky, C. Lagat, M. Sarmadivaleh and A. Barifcani, "A comparative study of density estimation of asphaltene structures using group contribution methods and molecular dynamics simulations for an Australian oil field," *J. Petrol. Explor. Prod. Technol.,* vol. 9, pp. 2699-2708, 2019.

[20] H. Groenzin and O. C. Mullins, "Molecular Size and Structure of Asphaltenes," *Petroleum Science and Technology,* vol. 19, no. 1-2, pp. 219-230, 2001.

[21] O. C. Mullins, H. Sabbah, J. Eyssautier, A. E. Pomerantz, L. Barré, A. B. Andrews and ..., "Advances in Asphaltene Science and Yen-Mullins Model," *Energy Fuels,* vol. 26, no. 7, pp. 2986-4003, 2012.

[22] S. Saad, A. S. Seraati, S. Roy, M. A. S. R. Saadi, J. R. Radović, A. Rajeev, K. A. Miller, S. Bhattacharyya, S. R. Larter, G. Natale, U. Sundararaj, P. M. Ajayan, M. M. Rahman and M. G. Kibria, "Transformation of petroleum asphaltenes to carbon fibers," *Carbon,* vol. 190, pp. 92-103, 2022.

[23] D. Leistenschneider, P. Zuo, Z. Abedi, D. G. d. K. A. Ivey, X. Zhang and W. Chen, "A mechanism study of acid-assisted oxidative stabilization of asphaltene-derived carbon fibers," *Carbon Trends,* vol. 5, p. 100090, 2021.

[24] P. Zuo, D. Leistenschneider, Y. Kim, Z. Abedi, D. G. Ivey, X. Zhang and W. Chen, "Asphaltene thermal treatment and optimization of oxidation conditions of low-cost asphaltene-derived carbon fibers," *Journal of Industrial and Engineering Chemistry,* vol. 104, pp. 427-436, 2021.

[25] F. N. Cogswell, "Converging flows of polymer melts in extrusion dies," *Polymer Engineering and Science,* vol. 12, no. 1, pp. 64-73, 1972.

[26] T. Kikutani, "Polymer Fiber Processing: Modeling," in *Encyclopedia of Materials: Science and Technology*, 2 ed., 2001, pp. 7280-7283.

[27] Lord Rayleigh Sec. R. S., "XVI. On the instability of a cylinder of viscous liquid under capillary force," *The London Edinburgh, and Dublin Philosophical Magazine and Journal of Science,* vol. 34, no. 207, pp. 145-154, 1892.

[28] D. He, J. J. Wylie, H. Huang and R. M. Miura, "Extension of a viscous thread with temperature-dependent viscosity and surface tension," *Journal of Fluid Mechanics,* vol. 800, no. 10, pp. 720-752, 2016.

[29] J. Bengtsson, K. Jedvert, T. Köhnke and H. Theliander, "The challenge of predicting spinnability: Investigating benefits of adding lignin to cellulose solutions in air-gap spinning," *J. App. Polym. Sci.,* vol. 138, no. 26, p. 50629, 2021.

[30] R. Beyreuther and R. Vogel, "Spinnability of Polymer Melts - a Complex Problem in Basic Research," *International Polymer Processing,* vol. 11, no. 2, 1996.

[31] D. Ram Babu and D. E. Cormack, "Effect of oxidation on the viscosity of athabasca bitumen," *The Canadian Journal of Chemical Engineering,* vol. 62, no. 4, pp. 562-564, 1984.

[32] N. Naghizada, G. H. C. Prado and A. de Klerk, "Uncatalyzed Hydrogen Transfer during 100−250 °C Conversion of Asphaltenes," *Energy Fuels,* vol. 31, no. 7, pp. 6800-6811, 2017.

[33] A. S. Alili, M. N. Siddiquee and A. de Klerk, "Origin of Free Radical Persistence in Asphaltenes: Cage Effect and Steric Protection," *Energy Fuels,* vol. 34, no. 1, pp. 348-359, 2020.

[34] T. Montoya, B. L. Argel, N. N. Nassar, C. A. Franco and F. B. Cortés, "Kinetics and mechanisms of the catalytic thermal cracking of asphaltenes adsorbed on supported nanoparticles," *Pet. Sci.,* vol. 13, pp. 561-571, 2016.

[35] ImageJ, "DiameterJ," [Online]. Available: https://imagej.net/plugins/diameterj#:~:text=DiameterJ%20is%20a%20validated%20nanofiber,a%20histogram%20of%20these%20diameters.. [Accessed 5 August 2022].

[36] OpenCV, "Image Denoising," [Online]. Available: https://docs.opencv.org/3.4/d5/d69/tutorial_py_non_local_means.html. [Accessed 5 August 2022].

[37] S. Reza Bagheri, B. Masik, P. Arboleda, Q. Wen, K. H. Michaelian and J. M. Shaw, "Physical Properties of Liquid Crystals in Athabasca Bitumen Fractions," vol. 26, no. 8, pp. 4978-4987, 2012.

[38] OriginLab Corporation, "16.9 Differentiate," [Online]. Available: https://www.originlab.com/doc/Origin-Help/Math-Differentiate. [Accessed 11 October 2022].

[39] W. Y. Svrcek and A. K. Mehrotra, "Gas Solubility, Viscosity and Density Measurements for Athabasca Bitumen," *J. Can. Pet. Technol.,* vol. 21, no. 4, 1982.

[40] G. E. Socrates Acevedo, M. A. Ranaudo, J. Piñate, A. Amorín, M. Díaz and P. Silva, "Observations about the Structure and Dispersion of Petroleum Asphaltenes Aggregates

Obtained from Dialysis Fractionation and Characterization," *Energy Fuels,* vol. 11, no. 4, pp. 774-778, 1997.

[41] S. Nohut, "Influence of Sample Size on Strength Distribution of Advanced Ceramics," *Ceramics International,* vol. 40, no. 3, pp. 4285-4295, 2014.

[42] D. Karonis, E. Lois, S. Stournas and F. Zannikos, "Correlations of Exhaust Emissions from a Diesel Engine with Diesel Fuel Properties," *Energy Fuels,* vol. 12, no. 2, pp. 230-238, 1998.

APPENDICES

Appendix A. DiameterJ Histogram Data for Green Fibre Fraction Diameters

A.1. HISTOGRAM DATA FOR SDA GREEN FIBRE DIAMETERS

Radius (× 0.676 µm)	Counts					
	F1 2-5 min	F2 9-14 min	F3 16-21 min	F4 22-27 min	F5 28-33 min	F6 33-37 min
1	280	413	520	533	791	404
2	338	500	564	628	862	471
3	416	574	712	778	1036	536
4	605	901	1062	1114	1618	865
5	450	652	817	869	1209	669
6	576	784	893	904	1307	766
7	768	694	757	738	914	606
8	553	548	446	511	686	556
9	425	294	290	308	643	405
10	186	147	169	244	490	268
11	170	151	238	478	1664	437
12	158	130	421	1102	7593	1535
13	421	367	3132	6836	19345	3148
14	805	943	7914	11677	8271	6356
15	2206	4218	6304	6893	3732	9283
16	7014	6743	2402	3169	1170	7850
17	5048	2778	479	601	419	2585
18	3543	468	94	55	44	109
19	1554	79	141	11	26	15
20	332	28	95	8	15	11
21	108	7	19	13	6	4
22	60	0	9	5	4	2
23	149	0	0	1	0	0
24	39	0	0	0	0	0
25	39	0	0	0	0	0
26	17	0	0	0	0	0
27	20	0	0	0	0	0
28	22	0	0	0	0	0
29	15	0	0	0	0	0
30	158	0	0	0	0	0
31	29	0	0	0	0	0
32	0	0	0	0	0	0

A.2. HISTOGRAM DATA FOR SDA-260 GREEN FIBRE DIAMETERS

Nomenclature: t = time; r = fibre radius, 1 px = 0.741 µm

Fraction	F1	F2	F3	F4	F5	F6	F7	F8	F9	F10
t (min)	0-5	5-10	11-16	16-21	21-26	26-31	31-36	36-41	41-46	46-51
r (px)	Counts									
1	11	3	13	0	0	0	2	2	1	18
2	53	24	13	5	26	6	2	4	23	21
3	141	52	34	5	27	10	3	8	67	24
4	436	149	91	14	54	18	6	19	264	71
5	471	183	111	48	162	79	14	28	685	85
6	2019	205	149	52	185	77	37	229	1507	248
7	6034	173	113	79	284	99	110	1130	3086	715
8	11790	200	130	129	315	88	330	4644	8331	1919
9	11306	1119	87	253	453	140	3558	14479	16866	5184
10	12162	3068	276	44	500	2580	5970	9114	11544	7793
11	9295	4788	1701	61	2479	5698	7291	8108	5731	6035
12	5226	7098	5812	1461	5975	9490	2724	6200	2485	3105
13	3446	7162	7619	4144	7344	5305	2645	2214	1689	890
14	2133	4831	3327	2938	7286	4538	1166	620	764	426
15	1015	1890	474	1349	6446	1345	456	711	422	34
16	374	940	286	1179	3069	596	262	529	225	3
17	245	228	1674	183	1390	281	2	3	102	13
18	259	119	243	1048	282	511	0	4	37	534
19	86	84	23	1767	48	69	0	12	105	30
20	130	44	527	57	9	0	0	0	72	0
21	303	21	693	44	47	0	0	0	62	0
22	262	8	1	0	86	0	0	0	12	0
23	114	196	0	0	50	0	0	0	16	0
24	33	1158	0	0	15	0	0	0	11	0
25	25	452	0	0	13	0	0	0	0	0
26	10	0	0	0	27	0	0	0	0	0
27	29	0	0	0	9	0	0	0	0	0
28	82	0	0	0	3	0	0	0	0	0
29	54	0	0	0	13	0	0	0	0	0
30	37	0	0	0	38	0	0	0	0	0
31	13	0	0	0	7	0	0	0	0	0
32	160	0	0	0	0	0	0	0	0	0
33	251	0	0	0	0	0	0	0	0	0
34	408	0	0	0	0	0	0	0	0	0
35	1301	0	0	0	0	0	0	0	0	0
36	234	0	0	0	0	0	0	0	0	0
37	97	0	0	0	0	0	0	0	0	0

Fraction	F1	F2	F3	F4	F5	F6	F7	F8	F9	F10
t (min)	0-5	5-10	11-16	16-21	21-26	26-31	31-36	36-41	41-46	46-51
r (μm)	Counts									
38	164	0	0	0	0	0	0	0	0	0
39	191	0	0	0	0	0	0	0	0	0
40	1504	0	0	0	0	0	0	0	0	0
41	945	0	0	0	0	0	0	0	0	0
42	238	0	0	0	0	0	0	0	0	0
43	56	0	0	0	0	0	0	0	0	0
44	40	0	0	0	0	0	0	0	0	0
45	12	0	0	0	0	0	0	0	0	0
46	0	0	0	0	0	0	0	0	0	0
Fraction	F11	F12	F13	F14	F15					
t (min)	51-56	56-61	61-66	66-71	71-76					
r (μm)	Counts									
1	27	29	8	10	78					
2	74	80	55	121	249					
3	217	295	154	492	676					
4	665	1039	1301	2709	3628					
5	690	1170	2178	4286	9156					
6	2400	3729	4568	8506	23234					
7	5858	8871	8837	7944	30604					
8	13506	11760	14468	6024	39736					
9	19551	13178	6746	5723	27857					
10	8212	4276	3812	2354	8543					
11	3689	1995	1155	1175	3098					
12	899	652	384	503	1056					
13	492	110	27	852	671					
14	148	5	14	291	767					
15	24	0	1	24	869					
16	28	0	0	8	217					
17	29	1	0	0	21					
18	6	1	0	0	0					
19	6	1	0	0	0					
20	5	45	0	0	0					
21	31	83	0	0	0					
22	138	0	0	0	0					
23	279	0	0	0	0					
24	11	0	0	0	0					
25	0	0	0	0	0					

A.3. HISTOGRAM DATA FOR SDA-280 GREEN FIBRE DIAMETERS

Nomenclature: t = time; s = scaling; r = fibre radius.

Fraction	F1	F2	F3	F4	F5	F6	F7	F8	F9	F10	F11
t (min)	0-5	6-11	12-17	18-23	25-30	32-37	38-43	44-49	50-55	57-62	64-69
s (µm/100 px)	300	494	444	440	405	405	440	440	440	440	580
r (px)	Counts										
1	10	33	154	152	14	140	84	144	201	204	0
2	11	60	168	167	43	160	109	150	229	218	0
3	29	117	193	217	95	214	140	200	251	271	0
4	54	199	305	340	190	355	180	274	417	421	0
5	70	191	266	296	187	256	177	225	304	317	0
6	139	232	315	392	244	324	222	216	317	351	0
7	155	208	309	417	268	286	188	157	235	244	0
8	248	245	339	519	285	299	156	107	170	177	0
9	330	718	319	540	287	272	128	75	158	193	0
10	333	697	176	278	157	163	829	56	588	228	207
11	426	573	264	546	205	201	947	711	1309	879	95
12	384	1643	845	910	591	425	690	1246	3008	1022	1120
13	478	3633	1349	1115	690	1900	3256	2829	3131	2577	1389
14	364	3389	1353	2104	1663	1486	3503	1591	2931	1796	1991
15	285	5307	2465	4213	1421	3282	2507	769	1714	1156	3593
16	397	3163	2987	7626	3574	4805	1736	552	1054	1533	4340
17	366	3050	2150	6307	4458	1792	1022	221	197	601	4547
18	489	3463	1736	3052	4832	2191	322	50	82	227	4336
19	712	2955	2699	2873	4817	1198	238	143	94	53	3564
20	1053	1015	1093	1650	2712	1845	251	52	5	70	3100
21	1750	1268	339	785	2911	891	89	91	0	14	2386
22	2517	606	197	410	559	127	31	2	0	15	2418
23	4170	244	115	471	510	493	3	1	0	16	1389
24	7765	271	20	42	330	157	6	1	0	9	2057
25	8405	565	38	35	134	127	5	2	0	19	1890
26	6630	110	95	0	230	14	0	1	0	13	1054
27	9829	137	96	3	23	44	0	1	0	8	1036
28	6022	181	76	0	0	81	0	2	0	12	761
29	2743	69	8	0	0	68	0	1	0	0	265
30	2172	47	0	0	0	2	0	10	0	0	65
31	1471	53	0	0	0	18	0	176	0	0	57
32	1015	50	0	0	0	31	0	97	0	0	535
33	895	145	0	0	0	1	0	0	0	0	56
34	865	12	0	0	0	2	0	0	0	0	64
35	1274	5	0	0	0	1	0	0	0	0	0
36	738	8	0	0	0	1	0	0	0	0	62

Fraction	F1	F2	F3	F4	F5	F6	F7	F8	F9	F10	F11*
t (min)	0-5	6-11	12-17	18-23	25-30	32-37	38-43	44-49	50-55	57-62	64-69
s (µm/100 px)	300	494	444	440	405	405	440	440	440	440	580
r (px)	Counts										
37	290	11	0	0	0	1	0	0	0	0	198
38	72	27	0	0	0	0	0	0	0	0	0
39	78	3	0	0	0	0	0	0	0	0	94
40	95	174	0	0	0	0	0	0	0	0	0
41	481	191	0	0	0	0	0	0	0	0	126
42	670	2	0	0	0	0	0	0	0	0	0
43	254	0	0	0	0	0	0	0	0	0	0
44	129	0	0	0	0	0	0	0	0	0	107
45	67	0	0	0	0	0	0	0	0	0	0
46	26	0	0	0	0	0	0	0	0	0	0
47	9	0	0	0	0	0	0	0	0	0	0
48	0	0	0	0	0	0	0	0	0	0	107
>48	226	0	0	0	0	0	0	0	0	0	0

Notes:

- The magnification of images within this dataset are not identical.
- F11 was measured manually by overlaying the SEM image with lines in GIMP and varying the brush width. The fibre radius is then half the brush width. Counts are taken as line lengths in pixels, rounded to the nearest integer.

A.4. HISTOGRAM DATA FOR SDA-DEL10 GREEN FIBRE DIAMETERS

Nomenclature: t = time; r = fibre radius, 1 px = 0.741 µm

Fraction	F1	F2	F3	F4	F5	F6	F7	F8
t (min)	1-6	6-11	11-16	16-21	21-26	26-31	31-36	36-41
r (µm)	Counts							
1	0	3	13	5	26	6	2	2
2	4	24	13	5	27	10	2	4
3	14	52	34	14	54	18	3	8
4	57	149	91	48	162	79	6	19
5	69	183	111	52	185	77	14	28
6	120	205	149	79	284	99	37	229
7	101	173	113	129	315	88	110	1130
8	195	200	130	253	453	140	330	4644
9	687	1119	87	44	500	2580	3558	14479
10	31	3068	276	61	2479	5698	5970	9114
11	439	4788	1701	1461	5975	9490	7291	8108
12	4273	7098	5812	4144	7344	5305	2724	6200
13	10348	7162	7619	2938	7286	4538	2645	2214
14	5865	4831	3327	1349	6446	1345	1166	620
15	1749	1890	474	1179	3069	596	456	711
16	1662	940	286	183	1390	281	262	529
17	644	228	1674	1048	282	511	2	3
18	205	119	243	1767	48	69	0	4
19	272	84	23	57	9	0	0	12
20	134	44	527	44	47	0	0	0
21	150	21	693	0	86	0	0	0
22	48	8	1	0	50	0	0	0
23	49	196	0	0	15	0	0	0
24	26	1158	0	0	13	0	0	0
25	0	452	0	0	27	0	0	0
26	0	0	0	0	9	0	0	0
>= 27	0	0	0	0	58	0	0	0

A.5. HISTOGRAM DATA FOR SDA-DEL20 GREEN FIBRE DIAMETERS

Nomenclature: t = time; s = scaling; r = fibre radius

Fraction	F1	F2	F3	F4	F5	F6
t (min)	1-6	7-12	15-20	20-25	25-30	30-35
s (µm/100 px)	556	444	562	444	444	444
r (px)	Counts					
1	191	125	345	131	194	146
2	216	151	199	77	203	153
3	228	160	231	103	256	189
4	363	268	344	161	351	326
5	260	181	267	111	272	246
6	259	212	284	155	285	264
7	164	171	524	129	230	191
8	111	139	329	134	183	155
9	111	135	183	83	419	217
10	902	95	175	46	597	1170
11	608	94	1085	42	349	1155
12	1555	394	2162	35	567	2203
13	3221	1328	8563	93	1116	2427
14	1048	1270	5103	1391	596	2887
15	441	1131	2041	2229	1232	630
16	263	1247	1022	3603	2029	1326
17	155	1739	308	1513	1027	1598
18	63	696	91	1083	517	358
19	28	569	9	980	531	144
20	0	61	0	247	100	0
21	0	208	0	82	21	0
22	0	150	0	20	0	0
23	0	35	0	11	0	0
24	0	24	0	7	0	0
25	0	43	0	12	0	0
26	0	14	0	6	0	0
27	0	23	0	4	0	0
28	0	10	0	3	0	0
29	0	7	0	5	0	0
30	0	12	0	5	0	0
31	0	11	0	4	0	0
32	0	20	0	0	0	0
33	0	0	0	0	0	0

Note: the scaling s is given since the magnification of images within this dataset are not identical.

Appendix B. Tensile Specimen Preparation and Testing Details

B.1. GENERAL CONSIDERATIONS

The tensile testing procedure of single fibres must be designed to limit bias. Consider three categories of biases:

1. Stress bias: e.g., low-strength fibre fragments cannot be sampled since they tend to break during handling.
2. Force bias: e.g., it may not be possible to resolve low forces from noise in a tensiometer
3. Diameter bias: e.g., the human selection of single fibres may be biased toward larger, more visible diameters.

These biases would lead to a stress-diameter domain where tensile data is less likely to be sampled than true unbiased data. A diameter bias is acceptable as there are other methods to determine the diameter distribution of the fibres. A force bias due to instrument limitations could be considered a systematic error that is constant between groups of samples which would not invalidate any qualitative or semi-quantitative comparisons. However, the stress bias is a direct consequence of specimen preparation and handling. The dependence on the human factor calls for the minimization of stress bias, and therefore, a proper specimen preparation and handling procedure.

B.2. SPECIMEN PREPARATION AND HANDLING

Single fibres were isolated from a bundle of carbonized fibres by separating them lengthwise. Due to static, single fibres are dispersed onto white copy paper which could be picked out with the assistance of a magnifier and placed onto a cardstock cut-out. These papers were cut using the Cricut Explore Air 2, which allowed for precise cutting of complex geometry from an uploaded image. The choice of gauge length was chosen with consideration to two factors:

- Long intact fibres were rare. Tearing of the bundle preferred to disperse shorter fibres. Also, long fibres were more likely to break when moving and adjusting the fibre on the specimen paper due to the inherent volume effect of brittle materials.
- Fibres adhered to specimen paper with a short gauge length were also prone to breaking before a tensile test could be completed. There is less fibre length to damp vibrations between the grips, especially when mounting the specimen papers onto the tensiometer's clamps. Short gauge lengths could also break during curing or setting of the glue utilized due to the glue's shrinkage imparting a tensile strain on the fibre.

While 5 mm and 10 mm gauge lengths are both viable options, preparation of sufficient specimens that successfully complete the tensile tests outside of that range proved to be too time-consuming for its worth. Furthermore, a higher failure rate was a sign of higher human bias, which was undesirable for the quality of the data.

B.3. DIAMETER MEASUREMENT WITH LASER DIFFRACTOMETRY

For stress calculations, the diameter of each single fibre must be known, ideally at the location where the fibre breaks. For the size of the fibres tested (~5-20 µm) they are typically determined using SEM. However, it is virtually impossible to capture every fibre this way: the energy released at breaking is enough to scatter the fiber. As a result, not only is a significant amount of tensile data unusable, but stronger fibres release more energy upon breaking and so are more likely to scatter and less likely to provide data, which would lead to a bias against higher strength values. Although applying vacuum grease is claimed to dampen the vibrations enough so that the broken fibre remains on the specimen paper, SEM for many samples is costly and time-consuming. Laser diffractometry is a contactless alternative for determining diameters of single fibres and has already been applied in professional instruments[5].

In laser diffractometry, a straight beam of a known wavelength (515 or 532 nm) of light[6] is directed perpendicular to the fibre's length. The beam is scattered and projected onto a screen. A schematic of the apparatus is shown in Figure B. 1. The width of the intensity pattern relates to the diameter of the fibre. The simplest model is the Fraunhofer approximation which is a solution identical to a single-slit experiment. The Fraunhofer diameter D_{Fraun} is given by

$$D_{\mathrm{Fraun}} = \frac{m\lambda}{\sin\theta_m} \approx \frac{m\lambda L}{x_m},$$

where λ is the wavelength, θ_m is the scattering angle of the mth minimum, L is the distance from the fibre to the screen, and x_m is the distance from the centre of the diffraction pattern to the mth minimum. Note that the approximation $\sin\theta_m \approx \frac{x_m}{L}$ only works for small values of x_m, such as $m = 1$. The inaccuracy of the Fraunhofer approximation grows with decreasing fibre diameter. For fibres less than 50 µm in diameter, Mie scattering must be used. In this work, `miepython`, which is written for spherical applications, was modified to incorporate functions for cylindrical geometries. The modified version can be found on Github[7]. Mie scattering algorithms also require

[5] Dia-stron (2019). *Technical Fibre Testing Instrumentation* [Brochure].
[6] The laser had to be replaced a few times over the course of this work. They were all green wavelengths (~515-532 nm) but each change was re-calibrated with SEM diameter correlation.
[7] https://github.com/GhostOrder/Fibre-Tester-Scripts

knowledge of the complex refractive index of the fibre, which is taken to be 2.27-0.64i, corresponding to that of amorphous carbon in a green wavelength[8].

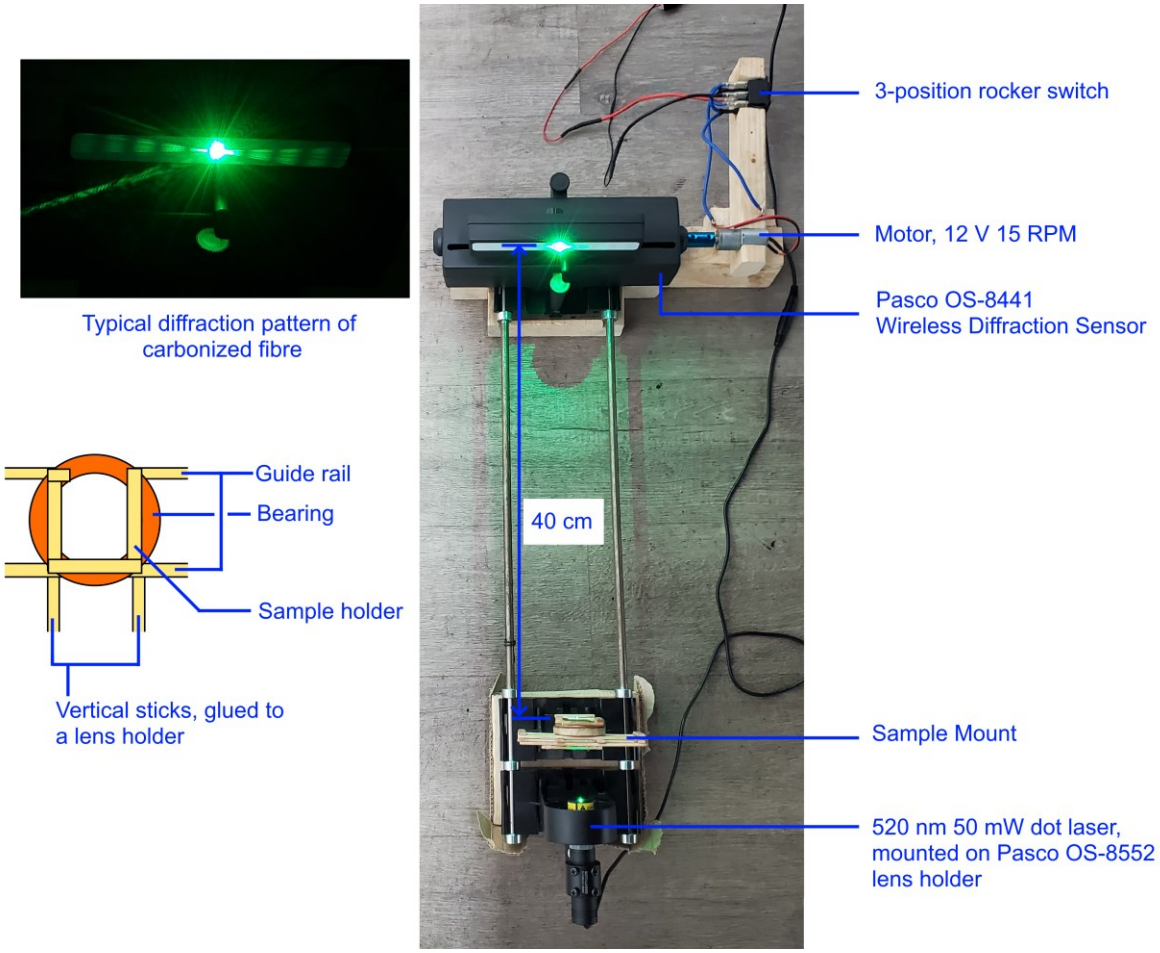

Figure B. 1: Schematic of laser diffractometer

Error in the assumptions of refractive index and wavelength, as well as measured distance between the fibre and the screen, all contribute to a deviation between diameters measured by laser and by SEM. To correct for this, the fibre fragments that remained on the specimen paper after tensile testing were measured in SEM. A linear correlation is established between laser and SEM diameters which is used to apply a "calibration correction." An example of this process is shown Figure B. 2.

[8] W. W. Duley. "Refractive Indices for Amorphous Carbon," *The Astrophysical Journal*, vol. 287, pp. 694-696, 1984.

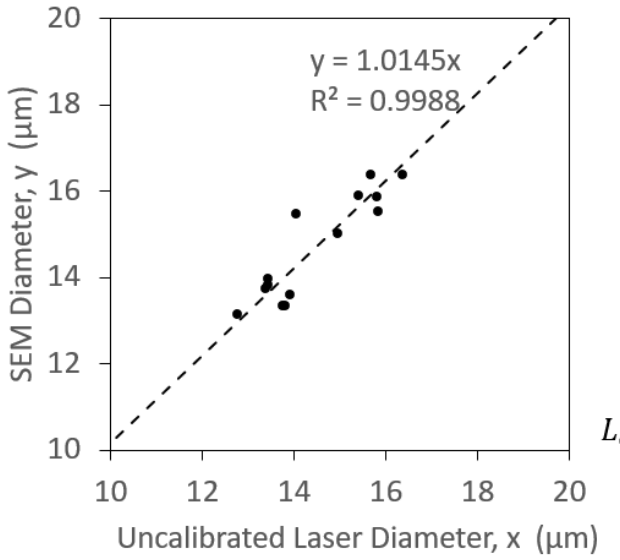

$$m\lambda \approx \frac{Dx_m}{L}$$

$$\frac{D_{\text{uncalibrated}}}{L_{\text{uncalibrated}}} = \frac{D_{\text{calibrated}}}{L_{\text{calibrated}}}$$

$$\text{slope} = \frac{D_{\text{calibrated}}}{D_{\text{uncalibrated}}} = \frac{L_{\text{calibrated}}}{L_{\text{uncalibrated}}}$$

$$L_{\text{uncalibrated}} = 40 \text{ cm}$$

$$L_{\text{calibrated}} = (40 \text{ cm})(1.0145) = 40.58 \text{ cm}$$

Figure B. 2: correlation and calibration of laser diameter to SEM diameter.

B.4. TENSIOMETRY AND WEIBULL ANALYSIS

Breaking force of a single fibre is determined using the tensiometer, Newton 100 series from TestResources, with a 1000 lbf actuator (DG1000) and a SMT-2.2-294 force transducer. The load accuracy is 11 N. Care must be taken when securing the specimens in the grips, since vibrations can prematurely break the fibre, especially for smaller gauge lengths. Once secured, the ligaments are cut with manicure scissors which produce less vibration when cutting. Thread snips and kitchen scissors cause too much vibration and break the fibre before the tensile test is initiated. Tensile tests were run in displacement control at a strain rate of 0.05 min^{-1}.

Tensile strength was determined from stress-strain diagrams in accordance with ASTM C1557-20. An example is shown below. The baseline stress was not necessarily zero due to taring errors or pre-loading in the fibre prior to beginning the tensile test. From the diagram, two parameters are manually specified:

1) The range in strain (uncorrected) corresponding to the baseline (taken after tensile failure)
2) The range in strain (uncorrected) corresponding to the linear increase in stress with strain, where there was no load slack (typically right before tensile failure).

By generalized least-squares regression, a piecewise-linear function denoted by the dashed blue line was fitted, from which the maximum stress, offset, and uncorrected elongation were obtained, as shown in Figure B. 3.

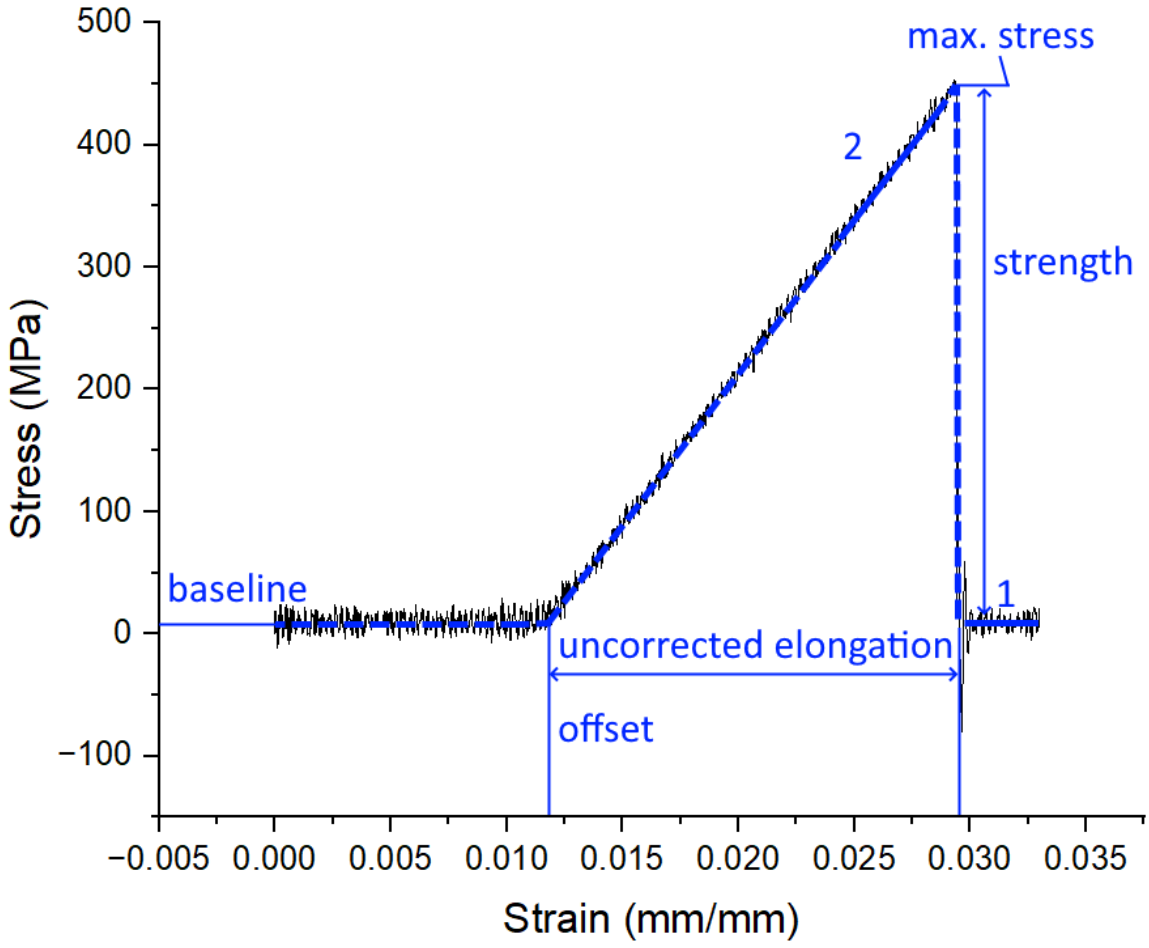

Figure B. 3: Characterization of experimental stress-strain plots

Tensile strength can be determined by subtraction of the baseline from the maximum stress. While elongation and elastic modulus were not used in discussion in this work, they could also be calculated by

$$\text{Elongation} = \frac{\text{Uncorrected Elongation}}{1 + \text{Offset}},$$

$$\text{Elastic Modulus} = \text{Slope} \times (1 + \text{Offset}).$$

The corrected gauge length which accounts for load slack or pre-loading is given by

$$\text{Corrected Gauge Length} = \text{Uncorrected Gauge Length} \times (1 + \text{Offset}).$$

Weibull parameter estimation was carried out using maximum likelihood estimation. This method is numerical and entails the minimization of the log-likelihood $\log L$ with respect to the Weibull parameters β and σ_0,

$$\log L = \sum_i \left(\log \frac{\beta}{\sigma_0} \frac{V_i}{V_0} + (\beta - 1) \log \frac{\sigma_{fi}}{\sigma_0} - \frac{V_i}{V_0} \left(\frac{\sigma_{fi}}{\sigma_0} \right)^{\beta} \right)$$

where V_i and σ_{fi} are the volume and tensile strengths of the ith single fibre. The estimated parameters are then used to calculate P for each sample to create Weibull plots. As the initial guess, Bernard's approximation is used to calculate P of each point without knowledge of the parameters, which is

$$P \equiv 1 - \exp\left(-\frac{V}{V_0} \left(\frac{\sigma_f}{\sigma_0} \right)^{\beta} \right) \approx \frac{i + 0.3}{N + 0.4},$$

where i is the index of sample sorted from lowest to highest tensile strength, and N is the total number of samples in the group.

Appendix C. Aliphatic to Aromatic Ratios from NMR Spectra

NMR spectra of asphaltenes can typically be separated into two peaks. For ^{1}H NMR, the peak at lower chemical shifts (<5 ppm) correspond to the protons bound to aliphatic carbon, while the peak at higher chemical shifts (>5 ppm) correspond to hydrogen bonded to aromatic carbons. There is a singlet peak at around 7.26 ppm in ^{1}H NMR which corresponds to the $CDCl_3$ solvent. This contribution of this peak is better discounted from the analysis of aromatic content. Meanwhile, for ^{13}C NMR, the lower chemical shift around 30 ppm corresponds to aliphatic carbons and the peak at higher chemical shifts around 130 ppm corresponds to aromatic carbons. There is an additional triplet peak in ^{13}C NMR spectra just under 80 ppm associated with the solvent. The interpretation of NMR spectra as explained here is better exemplified in the figures below, which are spectra for untreated SDA. To obtain aromatic and aliphatic content, the integral of the corresponding peak is taken.

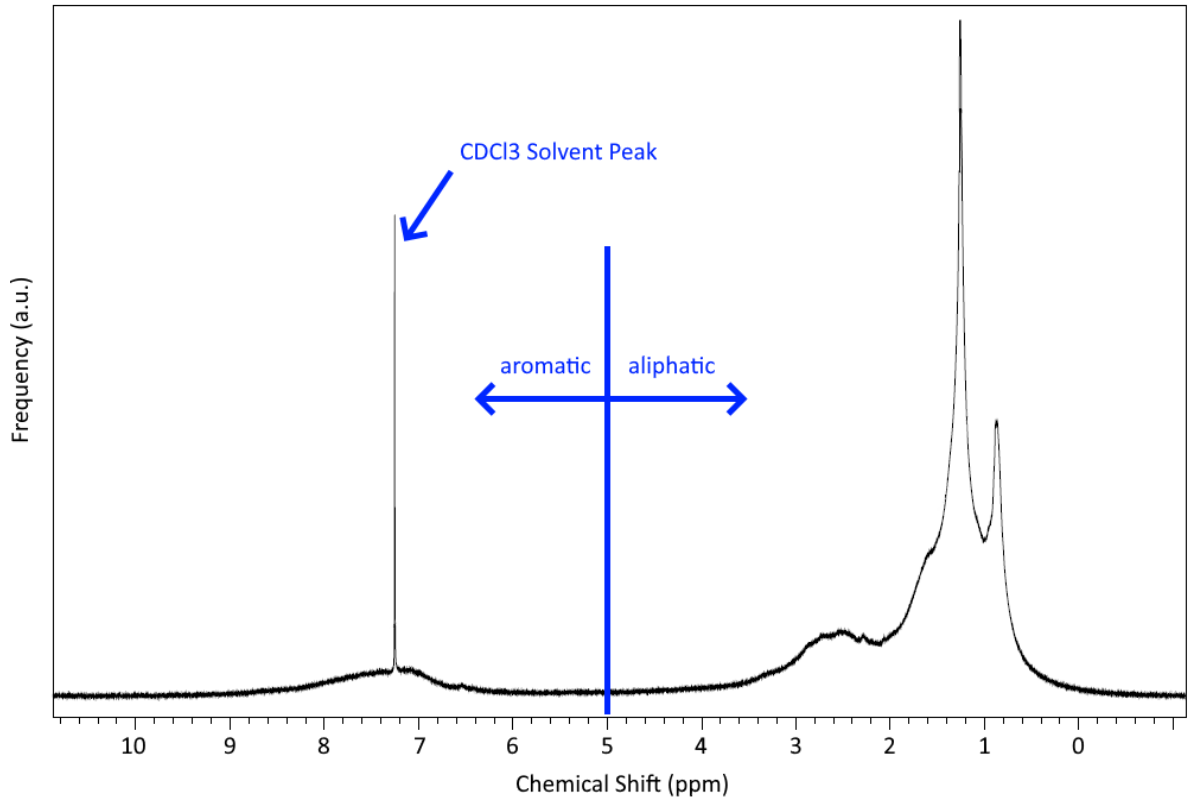
CDCl3 Solvent Peak
aromatic
aliphatic
Frequency (a.u.)
10
9
8
7
6
5
4
3
2
1
0
Chemical Shift (ppm)

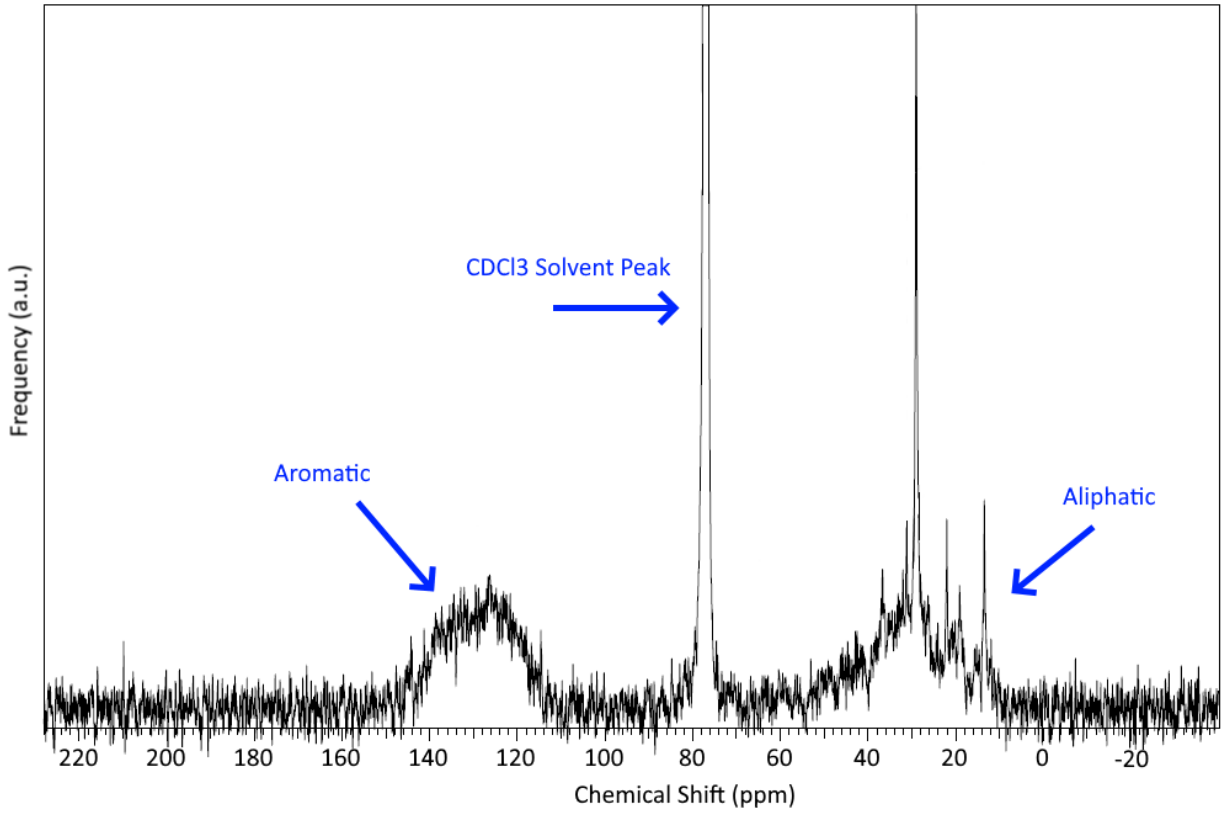
CDCl3 Solvent Peak
Aromatic
Aliphatic
Frequency (a.u.)
220
200
180
160
140
120
100
80
60
40
20
0
-20
Chemical Shift (ppm)

Appendix D. Tensile Data for Carbonized Fibre Fractions of Untreated SDA

D.1. TENSILE DATA FOR SDA F2 CARBONIZED FIBRES

Parameter	Value
Fraction Time	9-14 min
Number of Samples	31
Average strength	457 MPa
Average diameter	15.51 µm
Weibull modulus, β	4.74
Characteristic strength, σ_0	458 MPa
Reference Volume, V_0	0.00157 mm^3
Maximum Log-Likelihood	-187.9906

No.	D (µm)	L (mm)	σ_f (MPa)	P
1	16.63	5.06	631.35	0.9592
2	15.12	5.00	341.63	0.1327
3	19.58	5.00	235.77	0.0403
4	15.76	5.02	551.54	0.7774
5	15.14	5.15	451.89	0.4249
6	15.05	4.98	621.16	0.9081
7	14.95	5.05	614.44	0.8966
8	17.23	4.99	346.10	0.1781
9	16.13	5.03	345.62	0.1582
10	18.05	4.94	481.83	0.6402
11	15.98	5.08	476.87	0.5437
12	17.10	5.05	537.58	0.7932
13	15.23	5.07	403.25	0.2748
14	18.78	4.94	412.21	0.4104
15	14.90	5.03	683.77	0.9759
16	16.59	5.03	495.17	0.6324
17	16.07	5.02	427.93	0.3746
18	17.66	5.06	375.82	0.2656
19	16.26	5.01	361.08	0.1930
20	15.89	4.99	342.56	0.1469
21	16.53	4.99	507.00	0.6679
22	16.70	4.99	387.47	0.2700
23	16.04	5.04	538.93	0.7535
24	16.25	5.02	449.47	0.4543
25	15.89	5.07	441.10	0.4143
26	18.01	4.94	398.61	0.3393
27	17.17	4.98	405.08	0.3362
28	17.73	4.95	640.87	0.9781
29	17.61	4.93	420.33	0.3986
30	16.39	5.00	325.29	0.1242
31	16.49	4.95	516.05	0.6938

D.2. TENSILE DATA FOR SDA F3 CARBONIZED FIBRES

Parameter	Value
Fraction Time	16-21 min
Number of Samples	32
Average strength	475 MPa
Average diameter	16.22 µm
Weibull modulus, β	5.27
Characteristic strength, σ_0	470 MPa
Reference Volume, V_0	0.00157 mm^3
Maximum Log-Likelihood	-191.260

No.	D (µm)	L (mm)	σ_f (MPa)	P
1	16.69	4.98	353.06	0.1421
2	16.16	4.92	430.26	0.3315
3	13.68	5.02	584.17	0.7721
4	15.19	4.93	736.14	0.9977
5	15.98	4.95	383.67	0.1947
6	15.56	4.98	528.22	0.6725
7	15.69	4.95	594.43	0.8779
8	13.91	4.99	625.84	0.8875
9	15.39	4.98	521.90	0.6408
10	16.11	4.98	360.73	0.1478
11	16.14	4.95	569.60	0.8306
12	16.58	4.93	601.25	0.9165
13	15.72	4.95	547.55	0.7455
14	15.85	5.09	387.87	0.2071
15	15.95	5.01	474.27	0.4874
16	16.58	4.99	448.85	0.4160
17	16.34	5.08	341.65	0.1184
18	16.24	5.05	402.31	0.2540
19	17.16	4.98	404.89	0.2838
20	16.39	5.10	422.99	0.3248
21	16.71	5.05	366.11	0.1720
22	16.21	4.96	589.73	0.8843
23	16.67	5.08	491.17	0.5894
24	15.59	4.98	464.14	0.4323
25	15.89	5.00	324.26	0.0852
26	15.42	4.99	501.48	0.5661
27	17.06	4.95	475.23	0.5339
28	16.11	4.98	537.69	0.7312
29	15.79	5.10	399.87	0.2374
30	15.85	5.04	417.13	0.2862
31	17.59	4.98	506.52	0.6811
32	15.25	5.01	422.7	0.2831

D.3. TENSILE DATA FOR SDA F5 CARBONIZED FIBRES

Parameter	Value
Fraction Time	28-33 min
Number of Samples	22
Average strength	473 MPa
Average diameter	13.99 µm
Weibull modulus, β	5.51
Characteristic strength, σ_0	452 MPa
Reference Volume, V_0	0.00157 mm^3
Maximum Log-Likelihood	-133.540

No.	D (µm)	L (mm)	σ_f (MPa)	P
1	13.01	5.12	520.48	0.6123
2	12.44	5.12	467.60	0.3812
3	16.36	5.02	235.91	0.0186
4	13.98	4.99	575.14	0.8425
5	14.11	5.02	216.93	0.0088
6	14.26	5.07	502.88	0.6066
7	12.75	5.14	576.36	0.7987
8	12.29	5.15	515.40	0.5533
9	14.46	5.10	266.81	0.0290
10	15.69	5.12	509.45	0.7062
11	14.08	5.20	396.54	0.2226
12	14.11	5.10	385.90	0.1925
13	14.01	5.13	388.76	0.1979
14	13.01	5.11	558.82	0.7531
15	14.32	5.11	533.60	0.7313
16	15.60	5.12	480.63	0.5847
17	13.82	5.08	544.19	0.7422
18	12.03	5.12	614.20	0.8667
19	14.53	5.07	582.23	0.8858
20	13.81	5.05	574.79	0.8378
21	15.02	5.11	579.16	0.8967
22	14.18	5.08	378.76	0.1763